Universiteit Leiden
The Netherlands

Exploring strange new worlds with high-dispersion spectroscopy

Serindag, D.B.

Citation

Serindag, D. B. (2022, October 6). *Exploring strange new worlds with high-dispersion spectroscopy*. Retrieved from https://hdl.handle.net/1887/3466049

Version:	Publisher's Version
License:	Licence agreement concerning inclusion of doctoral thesis in the Institutional Repository of the University of Leiden
Downloaded from:	https://hdl.handle.net/1887/3466049

Note: To cite this publication please use the final published version (if applicable).

EXPLORING STRANGE NEW WORLDS

WITH

HIGH-DISPERSION SPECTROSCOPY

DILOVAN BANKS SERINDAG

Exploring Strange New Worlds
with High-Dispersion Spectroscopy

Proefschrift

ter verkrijging van
de graad van doctor aan de Universiteit Leiden,
op gezag van rector magnificus prof.dr.ir. H. Bijl,
volgens besluit van het college voor promoties
te verdedigen op donderdag 6 oktober 2022
klokke 15:00 uur

door

Dilovan Banks Serindag
geboren te Alexandria, Virginia, United States of America
in 1993

Promotor:
Prof.dr. I.A.G. Snellen

Co-promotor:
Dr. M.A. Kenworthy

Promotiecommissie:
Prof.dr. H.J.A. Röttgering
Prof.dr. E.F. van Dishoeck
Prof.dr. C.U. Keller
Dr. L. Kaltenegger (Cornell University)
Dr. H.J. Hoeijmakers (Lund University)

ISBN 978-94-6423-974-4

Cover designed by Maria Cristina Fortuna and Dilovan Banks Serindag,
and illustrated by Maria Cristina Fortuna

Printed by ProefschriftMaken (www.proefschriftmaken.nl)

To my grandfather, David G. Banks,
who instilled in me the importance and power
of education and learning

Contents

1 Introduction **1**
1.1 Methods for probing exoplanet atmospheres 4
1.1.1 Transit spectroscopy 4
1.1.2 Emission spectroscopy 6
1.1.3 Imaging spectroscopy 6
1.1.4 Spectral resolution 7
1.2 Studies of exoplanet atmospheres 8
1.2.1 Chemical composition 8
1.2.2 Structure and dynamics 10
1.2.3 Young planets 12
1.2.4 Habitability and extraterrestrial life 13
1.3 This dissertation 15

2 Is TiO emission present in the ultra-hot Jupiter WASP-33b? A reassessment using the improved ExoMol TOTO line list **17**
2.1 Introduction 19
2.2 Subaru data of WASP-33 20
2.3 Search for TiO emission 21
2.3.1 ExoMol TOTO opacities for TiO 21
2.3.2 *petitRADTRANS* TiO emission models 22
2.3.3 Cross-correlation search for TiO emission 24
2.4 Results 24
2.4.1 Welch's t-test 30
2.4.2 Injection–recovery test 30
2.5 Discussion and conclusions 33
2.5.1 Scenario I: Only our detection with ExoMol TOTO is valid 33

2.5.2 Scenario II: Only the Nugroho et al. (2017) detection with Plez98 is valid . . . 36
2.5.3 Scenario III: Both detections are valid . . . 37
2.5.4 Scenario IV: Both detections are false positives . . . 38
2.A K_p–v_{sys} matrices . . . 39

3 Measuring titanium isotope ratios in exoplanet atmospheres 47
3.1 Introduction . . . 49
3.2 High-resolution TiO spectral data . . . 51
3.2.1 CARMENES spectrum of GJ 1002 . . . 51
3.2.2 Choice of wavelength range for TiO fitting . . . 52
3.3 High-resolution TiO spectral models . . . 53
3.4 Fitting TiO isotopologue abundances . . . 55
3.5 Results . . . 56
3.5.1 Ti isotope ratios for the M-dwarf GJ 1002 . . . 56
3.5.2 Ti isotope ratios from noise-degraded spectra . . . 56
3.6 Discussion . . . 59
3.6.1 Effects of wavelength range and broadband filtering . . . 59
3.6.2 GJ 1002 Ti isotope ratios in context . . . 62
3.6.3 Determining Ti isotope ratios for gas-giant exoplanets . . . 62
3.7 Conclusions . . . 64
3.A Supplementary materials . . . 66

4 A search for protoplanets around the young star HD 169142 using molecule mapping 71
4.1 Introduction . . . 73
4.2 Integral field spectroscopic data of HD 169142 . . . 75
4.2.1 Data acquisition and characteristics . . . 75
4.2.2 Data reduction . . . 76
4.2.3 Removal of stellar and telluric contamination . . . 78
4.2.4 Combining observations . . . 78
4.3 Search for planet signals . . . 79
4.4 Injection–recovery tests of synthetic planet signals . . . 80
4.5 Results . . . 81
4.5.1 Non-detection of planet signal . . . 81
4.5.2 Injection–recovery tests . . . 81
4.6 Discussion and conclusions . . . 83

5 Testing the detectability of extraterrestrial O_2 with the extremely large telescopes using real data with real noise 85
5.1 Introduction 87
5.2 Archival data of Proxima Centauri 89
5.2.1 Initial data reduction 89
5.2.2 Assessment of data quality 90
5.3 Synthetic oxygen transmission spectra 92
5.3.1 Transmission model calculation and injection 92
5.3.2 Signal recovery 94
5.3.3 Perfect Gaussian-noise comparisons 94
5.4 Results 95
5.4.1 Transits at constant v_{offset} 95
5.4.2 Combining transits at multiple v_{offset} 96
5.5 Discussion and conclusions 98

Bibliography 100

Summary 111

Samenvatting 115

List of publications 119

Curriculum vitae 121

Acknowledgments 123

Chapter 1

Introduction

The contemplation of planets beyond Earth and the Solar System is recorded to stretch back millennia, though perhaps not always phrased in such precise terms. For instance, the Greek philosopher Epicurus (c. 341–271 BCE) mused that there exist "an infinite number of worlds, some like this world, others unlike it" (Laertius & Hicks 2015). Such openness to worlds unlike our own is rather prescient, and foreshadows the themes of investigating unfamiliar, often extreme, objects and pushing observational and theoretical capabilities that are recurrent in the more recent scientific study of exoplanets — those worlds beyond our Solar System. Over the past three decades, many such unfamiliar worlds have been discovered and explored in the pursuit of answers to the key questions of exoplanetary science, such as *What kinds of planets exist beyond the Solar System? Of what are these planets made? How did they form?* and *Is there life beyond Earth?*

Indeed, the first exoplanet discovered orbiting a main-sequence star proved to be one of these extreme objects. By measuring periodic Doppler shifts in the radial velocity of the solar-type star 51 Pegasi, Mayor & Queloz (1995) inferred the presence of the orbiting planet 51 Peg b (see Figure 1.1). This radial velocity method of exoplanet detection provides both the minimum mass of the perturbing planet and the orbital period. While the derived mass of about half that of Jupiter for 51 Peg b was not surprising, the same could not be said of the roughly four-day orbital period. For comparison, the closest orbit in the Solar System — the only other main-sequence planetary system known at the time — is that of Mercury lasting 88 days.

This extreme discovery, with no analogue in our own planetary system, immediately challenged and subsequently advanced the contemporaneous understanding of planet formation. Astonishment is readily evident in the discovery paper, in which Mayor & Queloz (1995) tried to reconcile the rather hot 0.05-AU orbit of 51 Peg b with the expectation that gas giant planets form in icy regions of protoplanetary disks, beyond several AU. Confronted with this new class of so-called hot Jupiters, planet formation theory developed further, and it is now accepted that planet migration is capable of decaying a gaseous planet's orbit from several AU to a few hundredths of an AU (e.g., Lin et al. 1996; Armitage et al. 2002). The extreme radiation environment of such planets also spurred studies into the nature of their atmospheres. Particular interest has been paid to how strong stellar irradiation impacts the chemistry, structure, and dynamics of hot Jupiters (e.g., Showman & Guillot 2002; Fortney et al. 2008; Showman et al. 2009, 2013) — a topic that will recur frequently throughout this dissertation.

Observationally, the discovery of 51 Peg b and similar hot Jupiters gave way to a series of survey programs to discover more exoplanets. The afore-

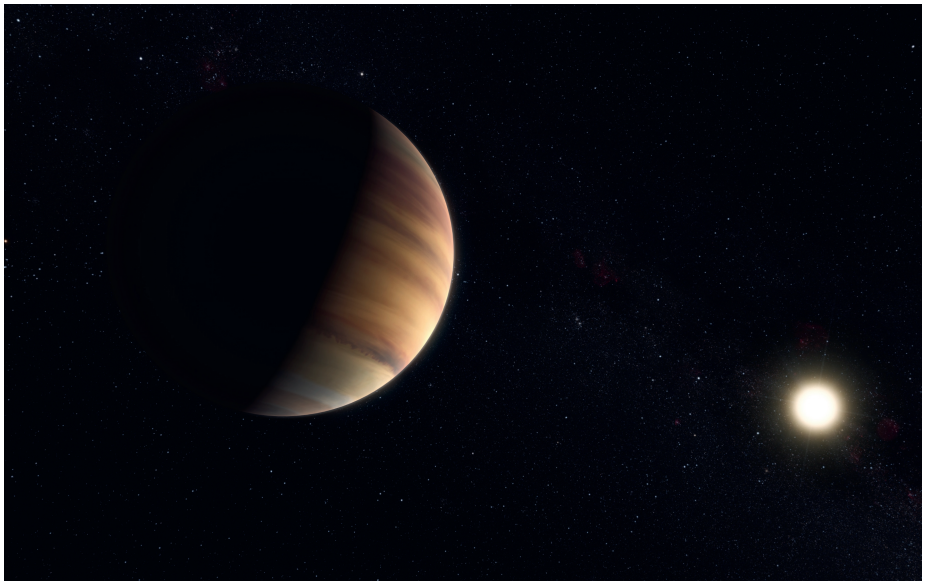

Figure 1.1. Artist's depiction of the archetypal hot Jupiter 51 Peg b. In addition to being the first exoplanet discovered orbiting a main-sequence star, 51 Peg b represents an extreme class of planet with no analogue in the Solar System. Image credit: ESO/M. Kornmesser/Nick Risinger (skysurvey.org).

mentioned radial velocity method, in which an orbiting planet is inferred by its gravitational perturbations of the host star's radial velocity, has been successfully employed using several ground-based spectrographs (e.g., HARPS/La Silla, HIRES/Keck), leading to the discovery of more than 900 planets. The success of this technique was later surpassed by transit surveys, in which fortuitously-aligned planets are detected from periodic decreases in stellar light as they orbit in front of their host stars. Following the successful application of this technique by Charbonneau et al. (2000) to the known hot Jupiter HD 209458 b, various ground-based (e.g., TrES, HATNet, WASP) and space-based (e.g., CoRoT, Kepler, TESS) surveys set out to detect planets from their transits. To date, in excess of 4900 planets have confirmed detections[1], with over 75% discovered using the transit method. In combination, the radial velocity and transit methods have provided 95% of all exoplanet discoveries.

[1]NASA Exoplanet Archive (https://exoplanetarchive.ipac.caltech.edu)

In addition to detecting exoplanets, radial velocity and broadband transit studies allow basic analysis of planetary bulk properties. Being a gravitational effect, radial velocity analyses provide a lower limit on the planet mass $M_{\rm p} \sin i$, dependent on the inclination angle i between the orbital plane and the sky plane. On the other hand, the transit technique constrains the radius ratio of the planet and star $R_{\rm p}/R_\star$ and the inclination. In those cases where both radial velocity and transit observations are performed, and the stellar properties (e.g., stellar radius) are well known, the average planetary density may be derived. This can provide a basic characterization of the planet, for instance, as a gaseous or rocky body. Such basic information is valuable for understanding the diversity of planet types. However, to more fully understand the characteristics of exoplanets, spectroscopic studies specifically probing their atmospheres are required.

1.1 Methods for probing exoplanet atmospheres

Studies to detect and characterize the atmospheres of exoplanets developed nearly contemporaneously with the first discoveries of these objects. Soon after the first broadband transit detection, Charbonneau et al. (2002) used a similar method to detect the first exoplanet atmosphere. By comparing the amount of light blocked by the hot Jupiter HD 209458 b during transit in different visible wavelength bands, they found excess absorption by the planet in the wavelength range containing the sodium D-lines at 5893 Å. Charbonneau et al. (2002) were thus able to infer the presence of sodium in the atmosphere of HD 209458 b.

Since then, the spectroscopic study of exoplanet atmospheres has advanced and expanded to observations across various wavelength ranges, spectral resolutions, and orbital phases, as well as planets spatially resolved from their host star. These various methods contribute complementary information about planets and their atmospheres.

1.1.1 Transit spectroscopy

Transit spectroscopy involves observing a planet at different wavelengths as it passes in front of its host star and attenuates a fraction of the stellar light. In addition to the broadband attenuation due to, for instance, the rocky core of a terrestrial planet or optically-thick atmospheric layers of gaseous planets, the optically-thin limb of the planetary atmosphere imprints a wavelength-dependent extinction due to its constituent spectroscopically-active species. As

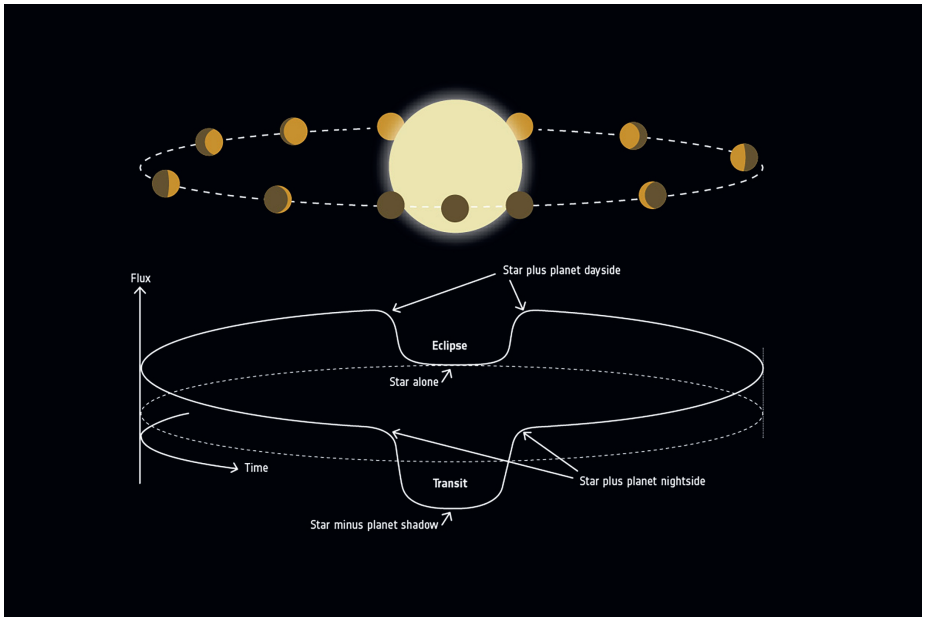

Figure 1.2. Flux variations in a transiting planetary system over the course of an orbit. The upper diagram shows how a greater fraction of the hotter planetary dayside is visible at orbital phases adjacent to secondary eclipse. The lower diagram plots the corresponding flux modulations. Image credit: ESA.

a result, the amount of light blocked — and thus the effective radius of a planet — will exceed the broadband radius for wavelengths corresponding to spectroscopic transitions. It is therefore possible to infer the presence of specific chemical species based on a transit spectrum.

Since transit spectroscopy probes the extinction of stellar light, rather than the emergent spectrum of the exoplanet, such observations are less sensitive to the vertical thermal structure of the planetary atmosphere than emission spectroscopy (see Section 1.1.2). Instead, by virtue of the observation geometry, transit spectra are most useful for probing the composition of the limb regions between the day- and nightside of the planet, as well as the atmospheric dynamics at these regions.

1.1.2 Emission spectroscopy

In contrast, emission spectroscopy measures the emergent flux of exoplanetary atmospheres. For hot Jupiters, such measurements probe the dayside atmosphere since these planets are expected to be in synchronous rotation and, as a result, the same side of the planet continuously faces the host star. This sets up a relatively strong temperature contrast between the dayside and nightside. As shown in Figure 1.2, as the planet orbits, various fractions of the hotter, brighter planet dayside are visible from Earth. Taking spectroscopic observations during the out-of-transit phases of the orbit allows the dayside planetary emission spectrum to be derived.

Since emission spectroscopy measures the flux from the planetary atmosphere itself, in addition to revealing the atmospheric composition, it provides constraints on the vertical temperature structure. Depending on the opacity, the spectrum will probe a different atmospheric layer at each wavelength, and thus a different point in the atmospheric temperature–pressure (T–P) profile. Fitting observed emission spectra with models that link T–P profiles to emergent spectra enable a characterization of the vertical temperature structure (e.g., Stevenson et al. 2014).

1.1.3 Imaging spectroscopy

Emergent spectra can also be measured for planets that are spatially resolved from their host stars. These directly-imaged planets are usually first detected with photometric and low-dispersion spectral observations in the near-infrared using some combination of physical obstruction (e.g., coronagraphs) and processing procedures to suppress the stellar flux (e.g., Marois et al. 2008; Lagrange et al. 2010; Chauvin et al. 2017). Planets manifest as temporally-persistent flux sources. Follow-up observations conducted over wider spectral ranges and at higher spectral resolutions enable more detailed analyses of planetary spectra (e.g., Konopacky et al. 2013; Barman et al. 2015; Petit dit de la Roche et al. 2018; Hoeijmakers et al. 2018b; Petrus et al. 2021).

Due to current observational limitations, this technique is most sensitive to widely orbiting ($\gtrsim$10 AU) planets, and in particular, young or still-forming planets. This is because planets are expected to cool on timescales of billions of years after their formation (e.g., Phillips et al. 2020), leading to a higher planet-to-star flux contrast for younger objects. For directly-imaged planets, it is not practical to derive mass and radius information from transit or radial velocity studies due to their relatively long orbital periods of tens of years. Therefore,

bulk properties such as mass, radius, and temperature must be derived using other techniques, for instance, analysis of the planet's luminosity and spectral energy distribution (e.g., Marois et al. 2008), or astrometric analysis of planet-induced perturbations of the proper motion of the host star (e.g., Snellen & Brown 2018).

1.1.4 Spectral resolution

The spectroscopic methods of observing exoplanet atmospheres presented and discussed in the preceding sections can be conducted at various dispersions. This is often quantified by the resolving power $\mathcal{R} = \lambda/\Delta\lambda$, where λ is the wavelength of observation and $\Delta\lambda$ is the spectral resolution. Higher values of $\mathcal{R}$ indicate a finer resolvability along the spectral axis, allowing greater differentiation of spectral features and velocity shifts. Spectra are generally referred to as low resolution for $\mathcal{R} < 10^3$, medium resolution for $\mathcal{R} \sim 10^3$, and high resolution for $\mathcal{R} \gtrsim 10^4$.

The main motivation for using medium- and high-resolution spectroscopy is the ability to resolve individual spectral lines, for instance, in molecular bands. Using model-matching techniques such as cross-correlation (e.g., Snellen et al. 2010) and atmospheric retrievals (e.g., Brogi & Line 2019), the signals of the unique set of individual lines of a chemical species, or blend of species, in high-dispersion data can be combined. For this reason, chemical detections based on high-resolution spectroscopic analysis are often considered more unambiguous than those using low-resolution spectroscopy, though quantifying the robustness of high-dispersion detections is still a matter of discussion (Cabot et al. 2019).

A corresponding critical advantage of high-dispersion spectroscopy is the increase in velocity resolution. Current high-resolution spectrographs typically have $\mathcal{R} \sim 10^5$, corresponding to velocity resolutions of $\sim$1 km s^{-1}. This allows the changing radial velocity of the exoplanet to be resolved as it orbits, which assists in differentiating the planetary atmospheric signal from that of the host star and Earth's atmosphere. This contributes to the greater unambiguity of high-resolution detections. As will be discussed in subsequent sections, this more precise velocity resolution enables the study of dynamics within planet atmospheres.

1.2 Studies of exoplanet atmospheres

Over the past several decades, studies of exoplanet atmospheres have consistently pushed observational and theoretical capabilities in an effort to better understand various aspects of these objects, including chemical makeup, structure and dynamics, young and forming planets, and habitability and the search for extraterrestrial life. Thoroughly investigating each of these avenues, often for extreme cases, has promoted a better understanding of the nature of planets and their atmospheres in the round. The following sections highlight some of the significant advances in the field of exoplanet atmospheres, with a focus on results from high-dispersion studies and topics that have particular relevance to subsequent chapters.

1.2.1 Chemical composition

One of the earliest characteristics to be probed in the study of exoplanet atmospheres was chemical composition. As previously mentioned, the first detection of a planetary atmosphere outside the Solar System was conducted by finding sodium absorption in the transmission spectrum of a hot Jupiter (Charbonneau et al. 2002). This discovery was but the first in a continuing effort to tally the inventory of chemical species present in exoplanets. Due to current sensitivity limitations, this inventorying has rather exclusively been done for gas giant exoplanets, and in particular, hot Jupiters and young super Jupiters.

Through a combination of high- and low-dispersion transit, emission, and imaging spectroscopy from ground- and space-based observatories, dozens of different chemicals have been detected in the atmospheres of exoplanets. These include neutral atoms and ions across several grouping in the periodic table, including alkali metals (e.g., Li I, Na I, K I), alkaline Earth metals (e.g., Mg I, Ca I, Ca II, Sr II), transition metals (e.g., Sc II, Ti I, Ti II, V I, Cr I, Cr II, Mn I, Fe I, Fe II, Ni I, Y II), and nonmetals and metalloids (e.g., H I, He I, Si I). Additionally, various molecules have been detected, including CO, H_2O, CH_4, and HCN. High-dispersion studies have been particularly useful in detecting the presence of molecules (e.g., Snellen et al. 2010; Birkby et al. 2013) and transition metals (e.g., Hoeijmakers et al. 2018a, 2019), given the relatively high number of narrow, resolved spectral lines for these species that may be co-added.

Expanding this inventory to more chemical species across a wide range of exoplanets is important to understanding the various processes at work in exoplanet atmospheres. For instance, comparing observed chemical inventories to expectations from atmospheric chemical models enables the validation and refinement

of these models. Consider the case of the transition-metal molecule titanium (mon)oxide (TiO), which has strong visible-wavelength opacities and is prominent in the spectra of cool stars and hot brown dwarfs, in which gaseous TiO is expected to be most abundant for atmospheric temperatures ∼2000–3000 K (Lodders 2002). The dayside temperatures of ultra-hot Jupiters ($T_{\rm day} \gtrsim 2200$ K; Parmentier et al. 2018) have similar values. Despite predictions of the presence of gaseous TiO in these hottest of exoplanets (Hubeny et al. 2003; Fortney et al. 2008), unambiguous detections have proven scarce. Various effects have been invoked to explain this discrepancy between observation and theory, such as gravitational settling of TiO and its condensates to lower, less-observationally-accessible altitudes (Spiegel et al. 2009), transport of TiO to the planet's nightside by winds and subsequent condensation (Parmentier et al. 2013), and thermal dissociation in the cases of highest stellar irradiation (Lothringer et al. 2018). Pushing atmospheric models to extreme cases and attempting to validate them using observed chemical inventories has thus enabled advances in our understanding of potential non-equilibrium processes in exoplanet atmospheres.

Assembling complete chemical inventories of exoplanet atmospheres also enables a better understanding of how planets and their atmospheres form and evolve. The protoplanetary disks in which planets form are complex, with physical and chemical properties that vary with time (Eistrup et al. 2018). In general, though, it is expected that bulk chemical properties like elemental abundance ratios vary with temperature, and thus radial distance, from the host star. As a result, different planet formation models predict different trends of bulk chemical properties for exoplanet atmospheres depending on the orbital distance of formation, relative importance of gas and solid accretion to the atmospheric envelop, and accretion during any orbital migration (Madhusudhan 2019, and the references therein). Determining the abundances of these inventoried species by modeling and fitting exoplanet spectra can enable the empirical determination of elemental abundances and metallicity. Comparison with the associated trends predicted by planet formation scenarios can constrain the formation process for individual objects. For instance, Line et al. (2021) recently performed the first robust determination of the C/O value and metallicity of a hot-Jupiter atmosphere using high-dispersion dayside emission spectroscopy. The solar C/O value and subsolar metallicity they found in the hot Jupiter WASP-77Ab is inconsistent with general predictions made by various planet formation models, leading Line et al. (2021) to propose constraints on, for instance, the orbital distance at which atmospheric accretion occurred and the degree of planetesimal bombardment.

Another recent development that is pushing the boundaries of current chem-

ical inventorying capabilities is the differentiation and analysis of isotopes in exoplanet atmospheres. Isotopes, and their molecular counterparts isotopologues, of a given species behave slightly differently in radiative, chemical, nuclear, and dynamical processes. As a result, variations in relative isotope abundances trace these processes, and in a complementary fashion to elemental abundance ratios and metallicities, can constrain the formation and evolution of exoplanets. Recently, an isotopologue abundance ratio was robustly measured for the first time in a young, widely-orbiting super Jupiter. Zhang et al. (2021a) concluded that the enhanced ^{13}CO/^{12}CO value relative to that of the interstellar medium that they measured in the planet TYC 8998-760-1 b may indicate accretion of ices enriched in ^{13}CO during its formation. After performing a similar measurement for a brown dwarf and finding a ^{13}CO/^{12}CO value consistent with that of the interstellar medium, Zhang et al. (2021b) suggested that the difference in isotopologue abundance ratio could be indicative of different formation mechanisms for these two objects. As a result, isotope and isotopologue studies have begun to serve as a complementary tool to trace planet formation through chemical inventorying.

1.2.2 Structure and dynamics

In addition to itemizing the chemical inventories of exoplanet atmospheres, efforts have been made to characterize and understand exoplanets as three-dimensional objects. As alluded to in the discussion of TiO in the previous section, atmospheric analyses are pushing beyond simply determining whether chemical species are present in planet atmospheres, to trying to understand how these species are distributed and the associated impact on atmospheric structure. In turn, these studies drive a better general understanding of the structure and dynamics in exoplanet atmospheres.

Determining T–P profiles for exoplanets probes the vertical structure of their atmospheres and has been a major contribution of emission spectroscopy at both low and high spectral resolution. The variation of temperature with altitude is heavily influenced by the strength of the incident stellar radiation, as well as the chemistry of the atmosphere, which determines the opacities available for heating and cooling at each pressure layer. Unlike cooler hot Jupiters ($T \lesssim 2000$ K), most extremely-irradiated ultra-hot Jupiters exhibit T–P profiles that are isothermal or inverted, in which case the temperature increases with altitude over a certain range of pressures (Madhusudhan 2019; Baxter et al. 2020). Understanding the mechanisms that produce these inversions is of particular interest, as it involves the interplay between stellar irradiation, at-

mospheric chemistry, and atmospheric opacities in these extreme objects. Originally, it was proposed that inversions are driven by strong optical absorption of stellar radiation by gaseous TiO and/or VO (Hubeny et al. 2003; Fortney et al. 2008). However, given the scarcity of unambiguous detections of either molecule in exoplanets known to have inverted T–P profiles, further theoretical developments have suggested that various atoms (e.g., Fe I, alkali metals), ions (e.g., H^-, Fe II), and molecules (e.g., metal oxides, metal hydrides) besides TiO and VO have sufficiently strong optical opacities to drive temperature inversions (Mollière et al. 2015; Parmentier et al. 2018; Lothringer et al. 2018; Lothringer & Barman 2019; Gandhi & Madhusudhan 2019). Indeed, recent high-dispersion studies have found clear evidence for Fe I emission lines in several ultra-hot Jupiters (e.g., Pino et al. 2020; Yan et al. 2020; Nugroho et al. 2020a). Analysis of these extreme objects has thereby advanced the understanding of the impact of stellar radiation fields and atmospheric chemistry on the vertical structure of exoplanet atmospheres.

Observations have also started to reveal the structure and dynamics at work across the surfaces of hot Jupiters, often confirming the predictions of three-dimensional global circulation models of these tidally-locked planets (e.g., Showman et al. 2009, 2013). For instance, high-resolution transit spectroscopy has revealed net velocity offsets between atmospheric species and the orbital rest frames of exoplanets (e.g., Snellen et al. 2010; Brogi et al. 2016, 2018; Alonso-Floriano et al. 2019; Casasayas-Barris et al. 2019; Nugroho et al. 2020b), as well as asymmetries in these offsets when determined separately for the start and end of transit (e.g., Louden & Wheatley 2015; Ehrenreich et al. 2020). These findings reflect the impact of various dynamical factors, such as day-to-nightside winds, zonal jets, and planetary rotation. Additionally, these velocity asymmetries between the leading and trailing limbs have been shown to vary for different species in the ultra-hot Jupiter WASP-76b, which may trace different wind patterns at different altitudes in this planet (Kesseli et al. 2021).

Chemical gradients have also recently been inferred based on signal strength asymmetries in high-dispersion transit spectra. For instance, in the same study analyzing transit velocity asymmetries in the ultra-hot Jupiter WASP-76b, Ehrenreich et al. (2020) also found stronger Fe I absorption at the end of transit, when only the trailing (evening) limb was probed. This was interpreted as evidence for the condensation of Fe I on the night side and morning limb. These regions are expected to be cooler than the dayside and the evening limb due to the day-to-nightside temperature contrast of synchronously-rotating hot Jupiters and the shift in the dayside hot spot from the substellar point towards the evening limb due to zonal jets. Asymmetries in transit signal strength have

also been found in other chemical species, with transition metal atoms similarly presenting stronger signals in the hotter, inflated evening limb of WASP-76b, while more readily-ionized alkali atoms produce stronger signals at the cooler morning limb of this hot Jupiter (Kesseli et al. 2021). Such advances in understanding the dynamics and structure of exoplanets have thereby enabled the probing of their weather patterns.

1.2.3 Young planets

Characterizing planets at various ages allows for the study of their atmospheres at different stages of evolution and, for the youngest planets and protoplanets, during formation. Such observations uniquely complement studies that infer constraints on planetary histories based on current atmospheric properties such as elemental abundance ratios, metallicities, and isotope and isotopologue abundance ratios (see Section 1.2.1). Finding and characterizing planets early in their development also facilitates a better understanding of their impact on their formation environment. Rings, gaps, and spiral arm patterns have been observed in various disks around young stars, and it is expected that young planets may drive these substructures (ALMA Partnership et al. 2015; Andrews et al. 2016; Andrews 2020). Studying still-forming exoplanets, like those in the PDS 70 system (see Figure 1.3), allows these objects to be directly linked to observed disk structures (Bae et al. 2019; Toci et al. 2020), which may in turn influence the formation and evolution of their atmospheres.

As mentioned in Section 1.1.3, studies of young planets and their atmospheres are largely the province of direct imaging studies, which probe the emergent spectrum of these objects. Like high-dispersion transmission and spatially-unresolved emission spectroscopy, medium-resolution imaging spectroscopy has allowed unambiguous molecular detections. In particular, the molecule mapping technique developed by Hoeijmakers et al. (2018b), in which the spectra of the spatial pixels containing planet signal are probed for chemical signatures using cross-correlation with model atmosphere templates, has revealed the presence of CO and H_2O in several young planets (Hoeijmakers et al. 2018b; Petit dit de la Roche et al. 2018; Petrus et al. 2021), as well as provided constraints on planet parameters such as temperature and surface gravity. This method has also been applied to data of embedded, accreting protoplanets (Cugno et al. 2021) and protoplanet candidates (see Chapter 4), but produced ambiguous results.

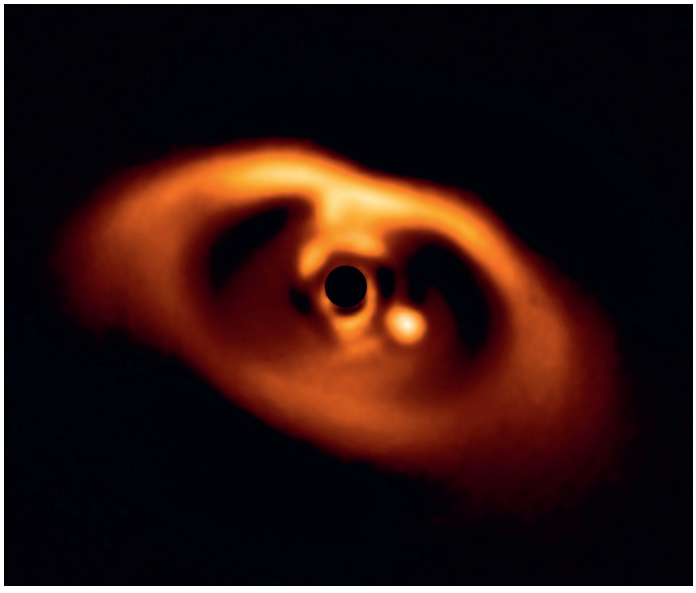

Figure 1.3. VLT/SPHERE near-infrared image of the young PDS 70 system. To the right of the central mask, the accreting protoplanet PDS 70 b is readily visible as an isolated emission source. Image credit: ESO/A. Müller et al.

1.2.4 Habitability and extraterrestrial life

The previous sections on the characterization of exoplanet atmospheres have exclusively focused on gas-giant planets, with a particular emphasis on hot Jupiters. Despite the significant advances made in understanding planetary atmospheres through studies of these extreme objects, hot Jupiters are relatively rare compared to terrestrial planets (Fressin et al. 2013). With the recent launch and deployment of the James Webb Space Telescope, upcoming ground-based extremely large telescopes (ELT, TMT, GMT), and planned future space-based observatories such as LUVOIR and HabEx, observational capabilities will improve and enable routine and robust measurements of atmospheres for progressively smaller, and eventually terrestrial, exoplanets. Studying terrestrial planet atmospheres is not only important for understanding planetary characteristics across various classes of planets, but also offers the opportunity to search for extraterrestrial life.

Many factors impact whether a terrestrial planet is capable of sustaining life as we know it (Kaltenegger 2017). Perhaps one of the most relevant from a planet detection standpoint is whether a given planet orbits within the habitable zone — the range of orbital distances where the equilibrium temperature of the planet can sustain liquid water. Several dozen such planets has been discovered,[2] but due to current observational constraints, have largely been out of reach of robust atmospheric analysis. Such analysis will be critical to determining whether life is indeed present on planets we believe to be habitable.

In particular, searching for atmospheric biosignatures — chemical species we associate with life on Earth — is seen as the most promising method for probing life on exoplanets. It has long been advocated that detecting multiple biosignatures in thermodynamic disequilibrium will be necessary to serve as robust evidence of extraterrestrial life (Lovelock 1965). Canonically, the specific combination of molecular oxygen and methane in the atmosphere of terrestrial planets has been proposed, since these two molecules should react rapidly and would therefore require substantial and ongoing replenishment to maintain their individual abundances (Lovelock 1975; Lippincott et al. 1967; Sagan et al. 1993). On the present-day Earth there are no such processes known to produce appreciable quantities of O_2, absent life (Meadows et al. 2018, and the references therein). However, for other planets the situation may not be as straightforward. For instance, it has been theorized that the vaporization and subsequent photodissociation of large bodies of water could be a substantial abiotic source of molecular oxygen in terrestrial planets (Luger & Barnes 2015). Recent studies have therefore advocated a more holistic approach to determining whether life is present, involving as complete a characterization of a planet and its atmosphere as possible to investigate the possibilities for such false positive scenarios (Meadows 2017; Meadows et al. 2018). In such an endeavor, the insights gained by studying the atmospheres of various classes of planet, including the most extreme hot Jupiters, will be invaluable.

[2]Habitable Exoplanets Catalog, The Planetary Habitability Laboratory, UPR Arecibo

1.3 This dissertation

The subsequent chapters in this dissertation present several works studying exoplanet atmospheres at medium- and high-spectral resolution, spanning a diverse set of topics in the field. In Chapter 2, the atmosphere of one of the hottest ultra-hot Jupiters WASP-33b is probed, in an attempt to verify a previous high-dispersion detection of gaseous TiO in its dayside emission spectrum. Despite expecting to retrieve a stronger signal using an improved spectral template for TiO, the signal detected in this reanalysis was weaker and found at inconsistent orbital velocities. An analysis of these results is presented and discussed in the context of the fidelity of high-resolution spectral observations.

For exoplanets in which TiO is unambiguously detected, Chapter 3 demonstrates how high-resolution emergent spectra can be used to determine the absolute and relative abundances of the isotopologues of TiO, and by extension, the relative abundances of Ti isotopes. As previously discussed, such isotope ratios can constrain processes at work during the formation and evolution of planet atmospheres. In this study, the impact of commonly-used high-dispersion processing techniques on measured abundances and abundance ratios is shown to be minimal, and the observing time required to perform such Ti isotope measurements is determined for upcoming observational facilities.

Chapter 4 investigates candidate protoplanets in a young protoplanetary disk system. A search for planetary atmospheric signatures in medium-resolution integral field spectroscopic data is conducted using molecule mapping, but does not reveal any compelling signals at the locations of the candidates. A sensitivity analysis indicates that the data is too noisy to probe the most promising candidate. Detectability requirements for upcoming, improved integral field spectrographs are estimated, and the impact of possible obscuring disk material is discussed.

This dissertation concludes in Chapter 5 with a forward-looking investigation into the feasibility of using the next generation of large ground-based telescopes to detect O_2 in the atmospheres of habitable-zone terrestrial planets. Previous studies have focused on determining the observing time necessary to detect this biosignature in high-resolution transmission spectra of temperate planets orbiting M-dwarf stars — a favorable planetary system set-up for such an endeavor due to the comparatively high planet-to-star flux contrast and relatively frequent transit occurrence. Chapter 5 improves upon previous works by incorporating real data with similar uncorrelated and correlated noise levels expected for future observations targeting O_2 in such terrestrial planets using the upcoming 39-meter Extremely Large Telescope.

Chapter 2

Is TiO emission present in the ultra-hot Jupiter WASP-33b? A reassessment using the improved ExoMol TOTO line list

Dilovan B. Serindag, Stevanus K. Nugroho, Paul Mollière, Ernst J. W. de Mooij, Neale P. Gibson, and Ignas A. G. Snellen
Published in Astronomy & Astrophysics, 645, A90 (2021)

Abstract

Context. Efficient absorption of stellar ultraviolet and visible radiation by TiO and VO is predicted to drive temperature inversions in the upper atmospheres of hot Jupiters. However, very few inversions or detections of TiO or VO have been reported, and results are often contradictory.

Aims. Using the improved ExoMol TOTO line list, we searched for TiO emission in the dayside spectrum of WASP-33b using the same data in which the molecule was previously detected with an older line list at 4.8σ. We intended to confirm the molecular detection and quantify the signal improvement offered by the ExoMol TOTO line list.

Methods. Data from the High Dispersion Spectrograph on the Subaru Telescope was extracted and reduced in an identical manner to the previous study. Stellar and telluric contamination were then removed. High-resolution TiO emission models of WASP-33b were created that spanned a range of molecular abundances using the radiative transfer code *petitRADTRANS*, and were subsequently cross-correlated with the data.

Results. We measure a 4.3σ TiO emission signature using the ExoMol TOTO models, corresponding to a WASP-33b orbital velocity semi-amplitude of $K_{\rm p} = 252.9^{+5.0}_{-5.3}$ km s^{-1} and a system velocity of $v_{\rm sys} = -23.0^{+4.7}_{-4.6}$ km s^{-1}. Injection–recovery tests using models based on the new and earlier line lists indicate that if the new models provide a perfect match to the planet spectrum, the significance of the TiO detection should have increased by a factor of $\sim$2.

Conclusions. Although the TiO signal we find is statistically significant, comparison with previous works makes our result too ambiguous to claim a clear-cut detection. Unexpectedly, the new ExoMol TOTO models provide a weaker signal than that found previously, which is offset in $K_{\rm p}$–$v_{\rm sys}$ space. This sheds some doubt on both detections, especially in light of a recently published TiO non-detection using a different data set.

2.1 Introduction

The first exoplanet discovered orbiting a main-sequence star was not only significant as a milestone in the search for such objects. As a gas-giant planet with a mass comparable to that of Jupiter but an orbital period of less than ten days, 51 Peg b represented a new class of planet with no analog in the Solar System (Mayor & Queloz 1995). The discovery of hundreds of these so-called hot Jupiters with such small orbital separations has naturally raised questions about the effects of intense stellar radiation on planetary atmospheres (Hubeny et al. 2003; Fortney et al. 2008). It is predicted that for sufficiently high levels of stellar irradiation, gaseous TiO and VO can persist in the upper atmospheres of hot Jupiters. Efficient absorption of ultraviolet and visible radiation by these molecules would lead to an inversion in the temperature–pressure profile — that is, an increase in temperature with decreasing pressure. The extent and prevalence of such inversions are important to understanding the various radiative, chemical, and dynamical processes at work in the atmospheres of hot Jupiters.

Evidence for thermal inversions and spectral signatures from TiO and VO are scarce in the literature, and results are often ambiguous and sometimes even contradictory. In particular, the relation between thermal inversions and the presence of TiO and VO is not evident. WASP-121b is an illustrative example. Evans et al. (2017) resolve near-infrared H_2O emission in secondary eclipse spectra, resulting in an unambiguous detection of a thermal inversion. While the inversion in WASP-121b is supported by TESS phase curve and eclipse photometry (Daylan et al. 2019; Bourrier et al. 2020), no spectroscopic evidence for TiO has been found (Evans et al. 2018; Merritt et al. 2020). Evidence for VO is present in both eclipse (Evans et al. 2017; Mikal-Evans et al. 2019) and transit (Evans et al. 2018) spectra at low resolution, but not in high-resolution transmission spectra (Merritt et al. 2020). Gibson et al. (2020) detect Fe I in high-resolution transmission spectra and suggest the inversion in WASP-121b may instead be driven by neutral iron.

Similarly, CO emission in low-resolution eclipse observations of WASP-18b indicates the presence of an inversion layer, but no evidence for TiO or VO has been found (Sheppard et al. 2017). Arcangeli et al. (2018) confirm the inversion and suggest that H^- opacity may play an important role in driving the inversion, instead of TiO or VO. Conversely, WASP-19b has a possible TiO detection but no evidence for a temperature inversion. Sedaghati et al. (2017) report a strong TiO signal in transmission at low resolution, while Espinoza et al. (2019) do not.

Currently, WASP-33b is the only exoplanet with a reported temperature

inversion and TiO emission detection based on high-dispersion spectral observations. Orbiting its A5 host star in a 1.2-day period, the ultra-hot Jupiter WASP-33b ($T_{\rm eq} \sim 2700$ K) is one of the hottest known exoplanets. Haynes et al. (2015) find a temperature inversion necessary to interpret near-infrared Hubble Space Telescope eclipse spectra, attributing excess flux at shorter wavelengths to TiO emission. Using cross-correlation techniques on high-resolution optical spectra taken of the planet's dayside with the Subaru Telescope, Nugroho et al. (2017) detect TiO in emission at the 4.8σ level, assuming the inverted temperature–pressure profile from Haynes et al. (2015). This is both the first high-resolution TiO or VO detection and the first high-resolution detection of a thermal inversion. However, Herman et al. (2020) analyzed similar quality high-resolution optical transmission and dayside spectra of WASP-33b taken with the Canada–France–Hawaii Telescope (CFHT) and do not detect a TiO signal. More recently, Nugroho et al. (2020a) have detected Fe I emission from WASP-33b in the same Subaru data and suggest neutral iron may also contribute to driving the inversion.

In this chapter, we used the new and more accurate ExoMol TOTO line list for TiO from McKemmish et al. (2019) to reanalyze the data of WASP-33b from the High Dispersion Spectrograph on Subaru, used by Nugroho et al. (2017) to find TiO emission in its dayside spectrum. We anticipated this improved line list would enable a significantly stronger TiO detection. In Section 2.2 we present this data of WASP-33b and discuss our methodology for detecting TiO in Section 2.3. We present and discuss our tentative detection in Sections 2.4 and 2.5.

2.2 Subaru data of WASP-33

For our analysis, we used archival spectra[1] of WASP-33 taken on 26 October 2015 using the High Dispersion Spectrograph (HDS) on the Subaru Telescope, first presented in Nugroho et al. (2017). A slit width of 0.″2 provided a resolving power $\mathcal{R} = \lambda/\Delta\lambda = 165,000$ ($\Delta v = 1.8$ km s^{-1}), with a pixel sampling of 0.9 km s^{-1}. Fifty-two observations with integration time 600 s were taken using both the blue and red HDS CCDs covering 6164–7396 Å and 7685–8810 Å, respectively. The observation midpoints span orbital phases $\phi = 0.207$–0.539, with the final 15 exposures taken with the planet in occultation.

The extraction of the one-dimensional HDS spectra is identical to that described in Sections 2.3 and 2.4 of Nugroho et al. (2017). Bias correction, bad-

[1]Proposal ID: S15B-090; PI: H. Kawahara

pixel masking, non-linearity correction, background subtraction, and flat fielding were performed on the blue and red CCD frames using IRAF. Subsequently, 18 blue and 12 red orders were extracted and continuum normalized, and a wavelength solution was determined by comparison with Th–Ar frames. A ∼0.1-pixel drift in the wavelength solution was identified by comparing the positions of strong telluric lines over the observing night, and corrected by spline interpolation. A 5σ outlier clipping was then applied to each wavelength bin. A full description of these preliminary reduction steps is given in Nugroho et al. (2017).

While these previous steps are identical to those in the original analysis, Nugroho et al. (2017) performed all further analysis for each order separately. Instead, we combined all blue and red orders into a single spectrum and entirely removed the overlapping wavelength regions, which show poor agreement. These regions amount to 7.5% of the wavelength bins. Although this removes some flexibility in treating particular orders differently, it also simplifies the analysis. In addition to flagging the telluric O_2 *A* and *B* bands at 7600 Å and 6900 Å, respectively, we flagged all wavelength bins with a telluric transmission value $\leq$0.98. These two steps result in a further flagging of 7.9% and 4.0% of the wavelength bins, respectively. After dividing each wavelength bin by its median value over all observations, we performed an additional 5σ clipping on each and set all outliers to the bin's median value.

To further identify and remove tellurics and systematic noise, we performed singular value decomposition (SVD) to deconstruct our data matrix into its constituent components as described in de Kok et al. (2013). We created ten new data matrices in addition to the original, each with a successively weaker SVD component removed. After interpolating each matrix onto a wavelength grid with pixels of width 0.5 km s^{-1}, we performed a single high-pass filter with full width 20.5 km s^{-1} (41 pixels) on each observation. We then divided each wavelength bin by its standard deviation over all observations. These last two steps were performed separately on the matrices of each SVD "iteration".

2.3 Search for TiO emission

2.3.1 ExoMol Toto opacities for TiO

Recently, McKemmish et al. (2019) published a new line list for TiO as part of the ExoMol project, which aims to calculate complete, accurate line lists for molecular species of interest to exoplanet spectroscopy (Tennyson & Yurchenko

2012). This ExoMol TOTO line list includes data for all the main TiO isotopologues[2], computed using more accurate experimental energy levels. McKemmish et al. (2019) demonstrate the superior quality of their ExoMol TOTO line list for the primary isotopologue ^{48}Ti^{16}O compared to the Plez (2012) line list (hereafter, Plez12), itself an improvement on the Plez (1998) line list (hereafter, Plez98) used by Nugroho et al. (2017) in their study of WASP-33b. Specifically, they note the improved completeness of the ExoMol TOTO line list, as well as improved positions and strengths of lines when compared to M-dwarf spectra. Pavlenko et al. (2020) show that the ExoMol TOTO line lists for the secondary isotopologues also provide an improvement over the Plez12 line list. We calculated TiO opacities using the ExoMol TOTO line list for each main isotopologue on a high-resolution grid ($\lambda/d\lambda = 10^6$) using the method presented in Appendix A of Mollière et al. (2015), which improves efficiency by computing the contributions of line cores and wing continua on a high- and low-resolution grid, respectively.

2.3.2 *petitRADTRANS* TiO emission models

The radiative transfer code *petitRADTRANS*[3] (Mollière et al. 2019) was used to model the TiO emission spectrum of WASP-33b. As input for *petitRADTRANS*, we adopted the Haynes et al. (2015) temperature–pressure profile with inversion also used by Nugroho et al. (2017), and calculated a corresponding one-dimensional mean molecular weight profile for 46 atmospheric layers from 10^2 to 10^{-5} bar using the equilibrium chemistry code described in Appendix A2 of Mollière et al. (2017) assuming a solar metallicity. Both profiles are plotted in the left panel of Figure 2.1. We included opacity contributions from all five main TiO isotopologues assuming solar abundances. We created a grid of such models, varying the total TiO volume mixing ratio $\log_{10}(\mathrm{VMR_{TiO}})$ from -7.0 to -10.0 in steps of 0.2. The $\log_{10}(\mathrm{VMR_{TiO}}) = -9.0$ emission model, scaled by the stellar continuum, is shown as an example in the right panel of Figure 2.1. To maximize any retrieved signal, we broadened these models to the HDS resolving power and performed a high-pass filter to mimic our treatment of the HDS data.

[2] ^{46}Ti^{16}O, ^{47}Ti^{16}O, ^{48}Ti^{16}O, ^{49}Ti^{16}O, ^{50}Ti^{16}O

[3] https://petitradtrans.readthedocs.io

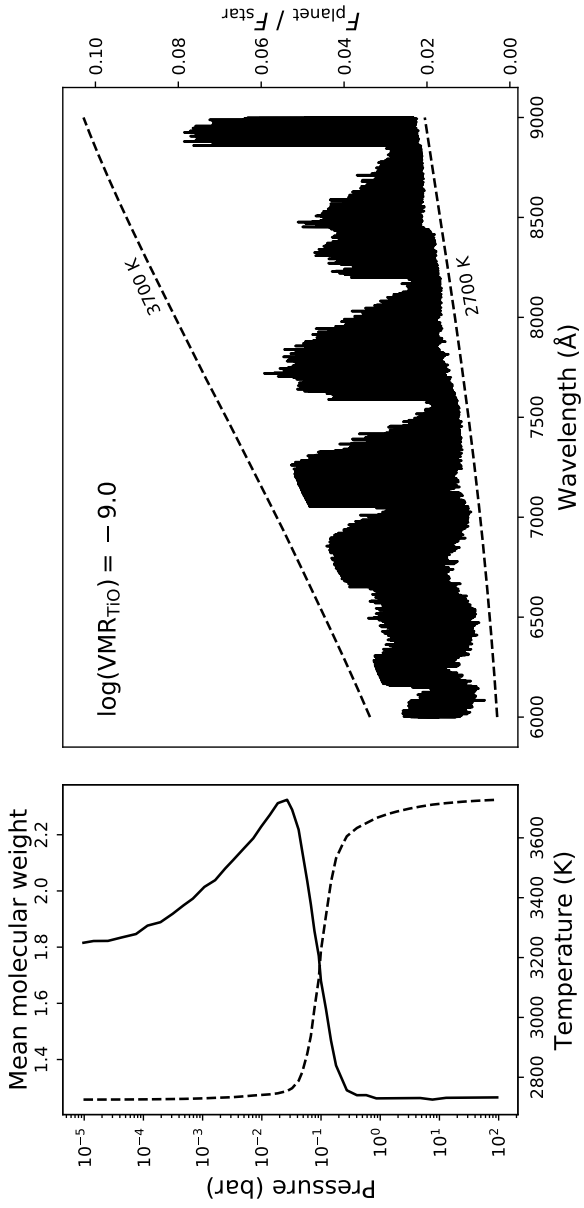

Figure 2.1. *Left panel*: Haynes et al. (2015) temperature–pressure profile with inversion (solid line) and calculated mean molecular weight profile (dashed line) used to model the TiO emission spectrum of WASP-33b. *Right panel*: example TiO emission spectrum for WASP-33b assuming a constant $\log_{10}(\mathrm{VMR}_{\mathrm{TiO}}) = -9.0$. The planet-to-stellar-continuum flux ratio is plotted (solid line). The dashed lines show the blackbody-to-stellar-continuum flux ratio for the minimum (2700 K) and maximum (3700 K) temperatures of the Haynes et al. (2015) temperature–pressure profile.

2.3.3 Cross-correlation search for TiO emission

To search for TiO emission in WASP-33b, we cross-correlated each model with the noise residuals of each observation over velocities ± 600 km s^{-1} in steps of 0.5 km s^{-1} relative to the observatory rest frame. The cross-correlation function (CCF) of each observation was normalized such that values of 0 and 1 correspond to no and full match, respectively, and then median subtracted. This process was performed on the data matrix of each SVD iteration separately, resulting in 11 two-dimensional CCF matrices for each model.

To combine any TiO emission signal over time, we shifted the CCF for each observation to the rest frame of the exoplanet, summed the CCFs for each out-of-occultation observation, and performed another median subtraction. This resulted in a one-dimensional CCF for the entire night of observations. The exoplanet velocity relative to the observatory rest frame at orbital phase ϕ is given by $v_{\rm p}(\phi) = v_{\rm bary}(\phi) + v_{\rm sys} + K_{\rm p} \sin(2\pi\phi)$, where $v_{\rm bary}$ is the velocity of the observatory relative to the Solar System barycenter, $v_{\rm sys}$ is the velocity of the WASP-33 barycenter relative to that of the Solar System, and $K_{\rm p}$ is the orbital velocity semi-amplitude of WASP-33b. While $v_{\rm bary}$ and the orbital phase for each observation are known, we varied $K_{\rm p}$ and $v_{\rm sys}$ to allow for deviations from those values reported by Nugroho et al. (2017) and to assess the noise properties of the CCF data. We stacked these one-dimensional CCFs into a $K_{\rm p}$–$v_{\rm sys}$ matrix, where each row is the aligned and summed CCF for a given $K_{\rm p}$ and each column corresponds to a different $v_{\rm sys}$. We converted the CCF values of each matrix to S/N values by dividing each row (constant $K_{\rm p}$) by its standard deviation. With 11 data matrices (one for each SVD iteration) and 16 model templates, we constructed 176 $K_{\rm p}$–$v_{\rm sys}$ matrices.

2.4 Results

We identified prospective TiO emission by searching for peaks in the $K_{\rm p}$–$v_{\rm sys}$ matrices that (1) have velocity values within a 3σ box of the $(K_{\rm p},\ v_{\rm sys}) = \left(237.5^{+13.0}_{-5.0},\ -1.5^{+4.0}_{-10.5}\right)$ km s^{-1} result from Nugroho et al. (2017), (2) have S/N $\geq 4\sigma$, and (3) are the strongest peak on the entire matrix. In the 176 $K_{\rm p}$–$v_{\rm sys}$ matrices, we found four peaks that satisfy these criteria, all with $(K_{\rm p},\ v_{\rm sys}) \approx (253,\ -23)$ km s^{-1}: peaks with S/N values of 4.05σ and 4.02σ for the SVD6 and SVD8 data matrices and $\log_{10}(\mathrm{VMR_{TiO}}) = -8.8$ model, and peaks with S/N values of 4.08σ and 4.03σ for the SVD6 and SVD8 data matrices and $\log_{10}(\mathrm{VMR_{TiO}}) = -9.0$ model.

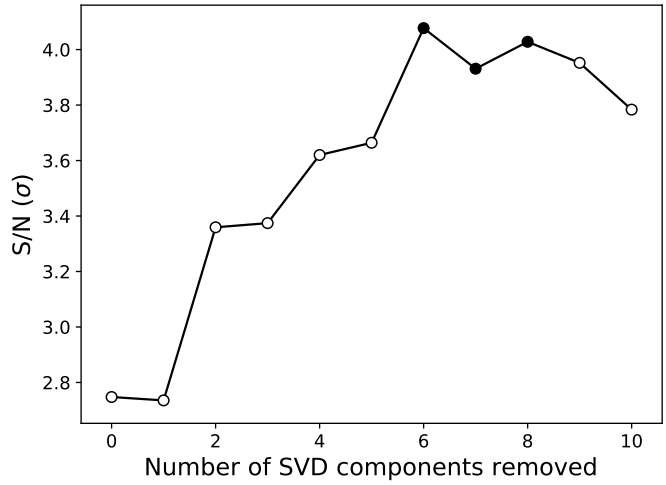

Figure 2.2. S/N of the emission peak around $(K_\mathrm{p},\ v_\mathrm{sys}) \approx (253,\ -23)$ km s^{-1} in the K_p–v_sys matrices for the $\log_{10}(\mathrm{VMR_{TiO}}) = -9.0$ model and data matrices with various numbers of SVD components removed. The filled circles indicate SVD iterations for which this emission peak is the strongest on the full K_p–v_sys matrix. Since the S/N value exceeds 4σ for SVD iterations 6 and 8, the peak was flagged by our analysis for these iterations.

Although we could not constrain the TiO volume mixing ratio, based on the slightly stronger S/N values, we adopted the $\log_{10}(\mathrm{VMR_{TiO}}) = -9.0$ template as our fiducial model and examined how varying the number of removed SVD components affects these prospective emission peaks. Figures 2.8 and 2.9 show the full K_p–v_sys matrices for the fiducial model and the data matrix after each successive SVD iteration. The dashed cyan box in each panel denotes the aforementioned 3σ region within which we searched for potential TiO emission, based on the velocities reported by Nugroho et al. (2017). The S/N and location of the strongest peak on each matrix is noted at the top of each panel and marked by a cyan ring on the matrix. Figures 2.10 and 2.11 show the same, but with the v_sys axis restricted to ± 100 km s^{-1} for clarity. For SVD iterations 6–8 the strongest peak of each matrix falls within the 3σ box around velocities $(K_\mathrm{p},\ v_\mathrm{sys}) \approx (253,\ -23)$ km s^{-1}. This same emission signal appears present in the K_p–v_sys matrices for all SVD iterations and becomes relatively prominent

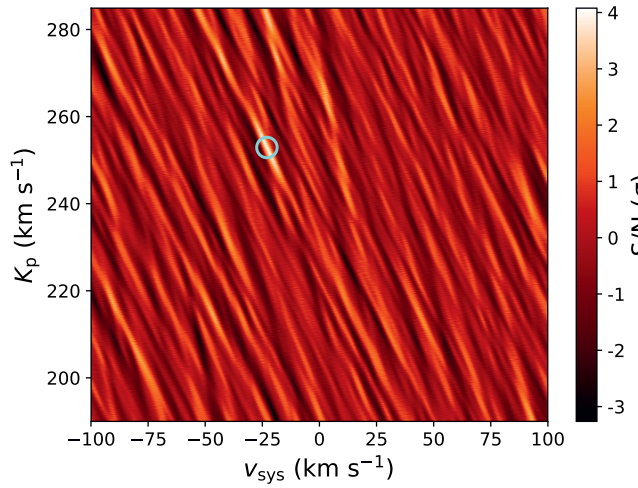

Figure 2.3. K_p–v_{sys} matrix of S/N values for the SVD6 data matrix and the $\log_{10}(\mathrm{VMR_{TiO}}) = -9.0$ model. For clarity, the v_{sys}-axis is restricted to ± 100 km s^{-1}. The matrix is plotted on the full v_{sys} range in Figure 2.9. The cyan ring indicates the location of the highest S/N value.

after two iterations of SVD.

To better quantify this, we plotted the S/N of this emission peak as a function of SVD iteration in Figure 2.2. After two SVD iterations the peak exceeds 3σ, which explains its relative prominence in the K_p–v_{sys} matrices for subsequent iterations. The solid markers for SVD iterations 6–8 indicate the peak has the highest S/N on the K_p–v_{sys} matrix for those iterations. That the strength of the peak falls below 4σ for the SVD7 case explains why it was not initially flagged in our search of all 176 K_p–v_{sys} matrices.

The strongest S/N value consistent with our search criteria is that at $(K_p,\ v_{sys}) = \left(252.9^{+5.0}_{-5.3},\ -23.0^{+4.7}_{-4.6}\right)$ km s^{-1} for the SVD6 data matrix and the $\log_{10}(\mathrm{VMR_{TiO}}) = -9.0$ model. The corresponding K_p–v_{sys} matrix, zoomed to a narrow v_{sys} range for clarity, is shown in Figure 2.3. The one-dimensional CCF for $K_p = 252.9$ km s^{-1} is shown in the top panel of Figure 2.4, recomputed over velocities ± 2775 km s^{-1} from the planet rest frame. We recalculated the noise as the standard deviation of the CCF across this wider velocity range while excluding the central ± 25 km s^{-1} to derive a more robust S/N $= 4.3\sigma$ for

the peak. The prominence of the central peak is clear over this extensive range of offset velocities.

In the bottom panel of Figure 2.4, we sequentially summed the CCFs of all observations in bins, performed a median subtraction, and normalized to S/N values using the standard deviation outside ± 25 km s^{-1}. The first three curves (solid blue, orange, and green) each consist of ten out-of-occultation observations and have peaks with S/N $\sim$ 2–3σ within 1.0 km s^{-1} (two pixels) of zero offset velocity. The fourth curve (solid red), consisting of seven out-of-occultation observations, has a S/N $\sim 3\sigma$ peak within 1.0 km s^{-1} of zero offset velocity. The final curve (dashed black) contains only ingress and fully occulted observations, and lacks a similarly distinct, coherent peak close to zero offset velocity. Thus, the presence or absence of the TiO signal seems consistent with the start of occultation.

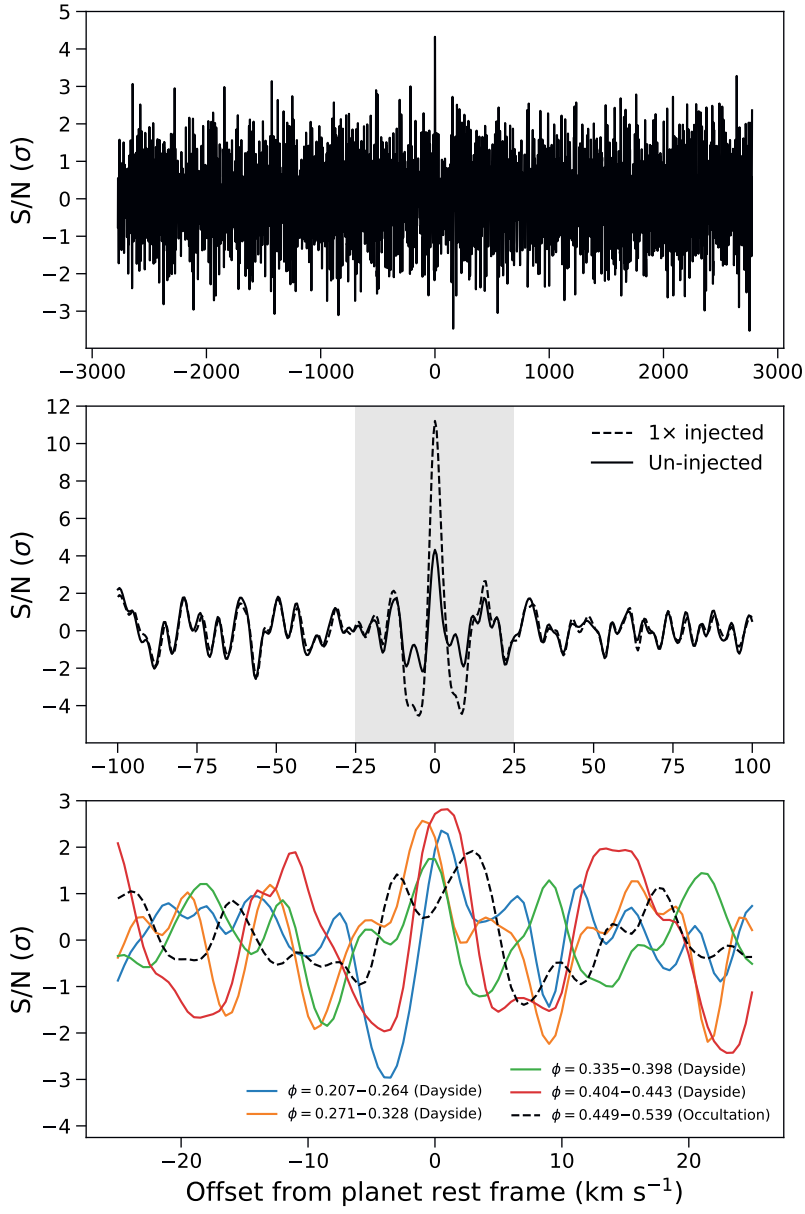
S/N (σ)
1× injected
Un-injected
ϕ = 0.207−0.264 (Dayside)
ϕ = 0.271−0.328 (Dayside)
ϕ = 0.335−0.398 (Dayside)
ϕ = 0.404−0.443 (Dayside)
ϕ = 0.449−0.539 (Occultation)
Offset from planet rest frame (km s^{-1})

Figure 2.4. *Top panel*: one-dimensional out-of-occultation CCF for the $\log_{10}(\mathrm{VMR_{TiO}}) = -9.0$ model and the SVD6 data matrix aligned to $(K_\mathrm{p},\ v_\mathrm{sys}) = (252.9,\ -23.0)$ km s^{-1}. The CCF values were converted to S/N values by dividing by the standard deviation outside ± 25 km s^{-1}. *Middle panel*: same, but on a narrower offset velocity range. The solid line plots the un-injected curve shown in the top panel, while the dashed line denotes the result of the $1\times$ injection case aligned to $(K_\mathrm{p},\ v_\mathrm{sys}) = (253.9,\ -24.0)$ km s^{-1}. The shaded region denotes the ± 25 km s^{-1} range that was excluded from the noise calculation. The peak S/N of the injected case is $2.6\times$ that of the un-injected case. *Bottom panel*: same as top panel, but instead of combining the out-of-occultation CCFs into a single one-dimensional CCF, we sequentially summed the individual CCFs for various portions of the observing night. Observations 1–37 are completely out of occultation. The CCFs of observations 1–30 are summed in sets of ten and denoted by the solid blue, orange, and green lines. The solid red line shows the combined CCF of observations 31–37. Observations 38–52 contain ingress and full occultation, and the combined CCF for these 15 observations is shown in the dashed black line.

2.4.1 Welch's t-test

To further investigate the significance of this emission signal, we performed a two-sided Welch's t-test to compare the in- and out-of-trail values of the two-dimensional out-of-occultation CCF matrix for $K_\mathrm{p} = 252.9$ km s^{-1} (Figure 2.5, top panel). Cabot et al. (2019) note that the significance given by the Welch's t-test is susceptible to overestimation from pixel oversampling. Therefore, we binned the two-dimensional CCF matrix along the velocity axis. Since the resolution element of the HDS data is 1.8 km s^{-1} and the pixel width is 0.5 km s^{-1}, we averaged the CCF values in three-pixel-wide bins. We adopted in-trail bounds $|v| \leq 1.5$ km s^{-1} and out-of-trail bounds 1.5 km s^{-1} $< |v| \leq$ 2775 km s^{-1}.

First, we verified that the out-of-trail values are Gaussian using the probability plot shown in the top panel of Figure 2.6. Within $\pm 4\sigma$, the out-of-trail CCF values are tightly correlated to a Gaussian normal distribution sampling. The Welch's t-test gives a two-sided p-value of 1.5×10^{-5}, which corresponds to a 4.3σ rejection of the null hypothesis that the in- and out-of-trail CCF values are drawn from the same distribution. This matches the peak S/N of the one-dimensional CCF reported in Section 2.4.

The bottom panel of Figure 2.6 separately plots the in- and out-of-trail CCF values, clearly showing an overall positive shift of the in-trail values relative to the out-of-trail values. We emphasize that the result of the Welch's t-test strongly depends on the adopted width of the in-trail region. Our treatment of the data matrices lowers the CCF values immediately surrounding the signal around $\pm$2–10 km s^{-1} (Figure 2.4, middle panel), lowering the Welch's t-test significance as more of this region is included.

2.4.2 Injection–recovery test

We also performed an injection–recovery test to check if we could successfully recover the planet signal. Using the emission peak velocities $(K_\mathrm{p},\ v_\mathrm{sys}) = (252.9,\ -23.0)$ km s^{-1} determined above, we calculated the relative velocity of WASP-33b at the midpoint of each observation and Doppler shifted the $\log_{10}(\mathrm{VMR}_\mathrm{TiO}) = -9.0$ model accordingly. We scaled each model emission spectrum to match our data's normalization, accounting for the planet-to-star full-disk ratio and the mid-observation visible illumination fraction of the planet, which we modeled as a Lambertian sphere. After broadening each model planet spectrum to the resolving power of the data and performing an additional boxcar smoothing to simulate the relatively long 600-s integration time, we added our

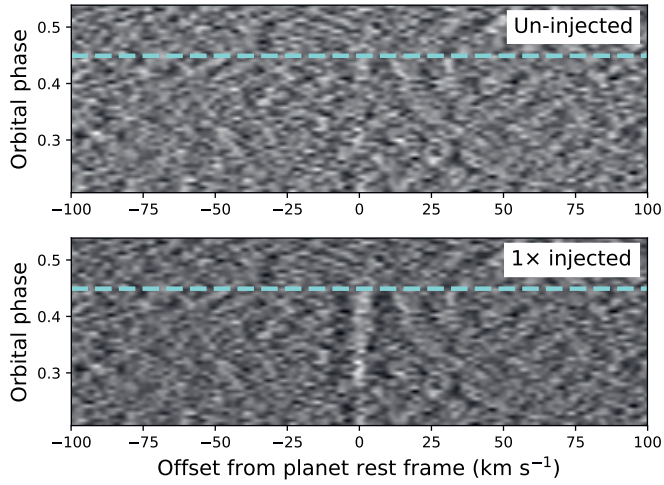

Figure 2.5. *Top panel*: two-dimensional CCF matrix for the $\log_{10}(\mathrm{VMR_{TiO}}) = -9.0$ model and SVD6 data matrix aligned to the exoplanet rest frame for $(K_\mathrm{p},\ v_\mathrm{sys}) = (252.9,\ -23.0)$ km s^{-1}. Each row is the one-dimensional CCF for a given observation. The first observation in occultation is denoted by the dashed cyan line. Orbital phase values 0 and 0.5 correspond to the center of transit and occultation, respectively. *Bottom panel*: same for the injection test discussed in Section 2.4.2. In this case, the velocities $(K_\mathrm{p},\ v_\mathrm{sys}) = (253.9,\ -24.0)$ km s^{-1} were used to shift to the exoplanet rest frame.

artificial signal to the pre-flagged HDS data. We thereby injected a TiO emission signal at 1× the expected level for WASP-33b. We subsequently performed the same procedure to reduce stellar, telluric, and systematic noise outlined in Section 2.2, removing six SVD components to mimic the treatment that gave our strongest signal. Using the $\log_{10}(\mathrm{VMR_{TiO}}) = -9.0$ template, broadened and filtered as described in Section 2.3.2, we calculated a K_p–v_sys matrix as discussed in Section 2.3.3.

The location of the strongest peak on this matrix is $(K_\mathrm{p},\ v_\mathrm{sys}) = (253.9,\ -24.0)$ km s^{-1}, matching very closely the injected values. The correspondingly aligned two-dimensional CCF matrix is shown in the bottom panel of Figure 2.5, demonstrating how the injected planet signal increases toward occultation as a larger fraction of the dayside becomes visible

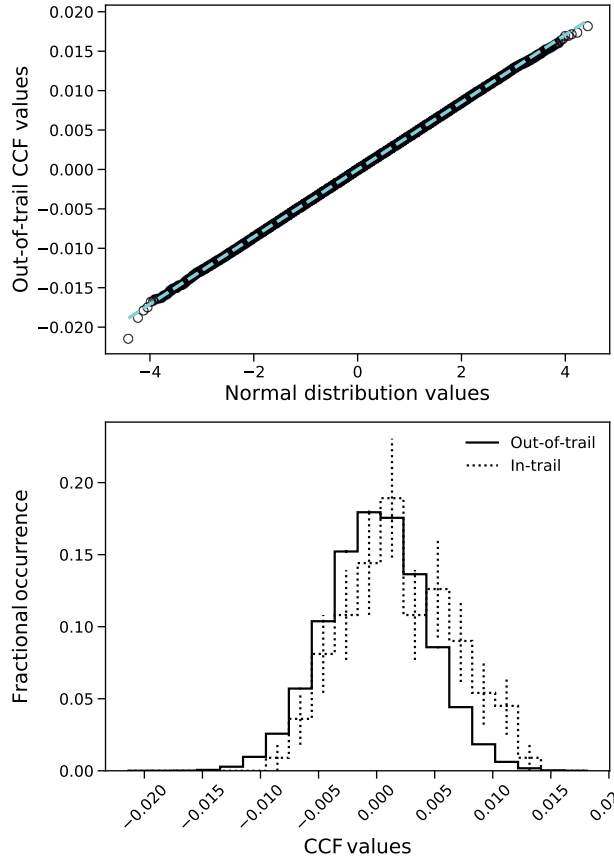

Figure 2.6. *Top panel*: probability plot comparing the binned out-of-trail CCF values to a sampling of the normal distribution (black rings). The dashed cyan line is the calculated linear regression. That the correlation so closely follows a linear trend indicates the out-of-trail values are well described by a Gaussian out to $\pm 4\sigma$. *Bottom panel*: histogram of the binned in- (dotted line) and out-of-trail (solid line) CCF values. Error bars were calculated as the square root of the individual bin count, normalized by the sample size. A two-sided Welch's t-test gives a 4.3σ rejection of the null hypothesis that both populations are draw from the same distribution.

along our line of sight. The middle panel of Figure 2.4 plots the summed one-dimensional CCF on a restricted range for the injected and un-injected cases, which show minimal difference for velocity offsets outside ± 25 km s^{-1}. Within ± 25 km s^{-1}, the shape of the central peak and aliasing of the CCF of the injected case matches very closely that of the un-injected case.

As for the un-injected case, we adopted as noise the standard deviation of the one-dimensional CCF over velocities ± 2775 km s^{-1}, excluding the central ± 25 km s^{-1}. We then recover the $1\times$-injected TiO emission at the 11.2σ level, which is $2.6\times$ as strong as the un-injected case (4.3σ). Assuming our injected model perfectly represents WASP-33b, we would expect a $1\times$ injection at the same location as our tentative detection to result in a doubling of the retrieved S/N. As our model is not perfect, however, an increase in S/N of over 100% from a $1\times$ injection–recovery test is to be expected.

2.5 Discussion and conclusions

Our detection of a tentative TiO signal in the dayside of WASP-33b is intriguing when compared to similar previous studies. Using the new and more accurate ExoMol Toto line list for TiO, we find a potential signal at the 4.3σ level in the HDS spectra. Nugroho et al. (2017) used the older Plez98 TiO line list to recover a stronger 4.8σ TiO signal from the same data. Meanwhile, Herman et al. (2020) analyzed CFHT transit and dayside spectra using the Plez12 line list, but do not detect TiO. There are four possible scenarios: (1) only our TiO detection with the ExoMol Toto template is valid, (2) only the TiO detection by Nugroho et al. (2017) using the Plez98 line list is valid, (3) both detections are valid, and (4) both detections are false positives. We discuss each below.

2.5.1 Scenario I: Only our detection with ExoMol Toto is valid

Taken in isolation, there are several aspects of our analysis that make our 4.3σ TiO signal compelling. In addition to the statistical significance of the one-dimensional CCF peak (Figure 2.4, top panel), the Welch's t-test presented in Section 2.4.1 rejects the hypothesis that the in- and out-of-trail CCF samples are drawn from the same distribution. Furthermore, the injection–recovery test discussed in Section 2.4.2 and shown in the middle panel of Figure 2.4 lends confidence to our result, in that the shape of the one-dimensional CCF around the signal peak for the $1\times$-injected case seems to be a scaled version of that for

the un-injected case. Additionally, when the aligned two-dimensional CCF is summed in bins (Figure 2.4, bottom panel), the presence or absence of the TiO signal seems consistent with the start of occultation.

Nonetheless, we anticipated our analysis of the same HDS data of WASP-33b using the improved ExoMol Toto line list would yield a stronger TiO detection than the 4.8σ result from Nugroho et al. (2017) using the older Plez98 line list. We initially suspected our weaker detection with a better line list may be partly due to our treatment of the spectral orders. Whereas Nugroho et al. (2017) separately reduced each order and subsequently optimized the number of SysRem iterations performed on an order-by-order basis using injection–recovery tests, we combined all orders into a single spectrum prior to our comparable step of SVD. As a result, our approach has fewer parameters to optimize and may be inherently unable to maximize the S/N to a similar degree.

To test whether combining all orders into a single spectrum leads to an inherent decrease in recoverable S/N, we performed a data reduction similar to that of Nugroho et al. (2017) that treats each spectral order separately. After the extraction, wavelength drift correction, and initial 5σ clipping steps described in Section 2.2, we performed the SysRem detrending algorithm (Tamuz et al. 2005) independently on each spectral order. After cross-correlation, the CCFs for each order were added with a uniform SysRem iteration. We chose not to optimize the SysRem iteration for each order based on injection–recovery tests so as to prevent biasing the signal recovery. However, running SysRem on each spectral order separately should, in principle, still facilitate a better reduction, assuming the noise varies for different orders. Similarly, the fact that the SysRem algorithm allows for weighting of individual pixels by their uncertainty during detrending should also enable a more optimized signal recovery. While we readily recover the Nugroho et al. (2017) signal with this methodology when the cross-correlation is performed with their Plez98 models, the results from cross-correlation with the $\log_{10}(\mathrm{VMR}_{\mathrm{TiO}}) = -9.0$ ExoMol Toto model are ambiguous and we cannot claim a detection — much less an improvement in signal — using this better-optimized methodology.

Additionally, the K_{p} and v_{sys} values of our TiO signal are offset compared to previous studies. In Figure 2.7, we plot our reported velocity values (circular marker), as well as those from Nugroho et al. (2017) (cross marker), Nugroho et al. (2020a) (star marker), and other studies of WASP-33b. In addition to a higher value for K_{p}, the value our TiO analysis derives for v_{sys} is blue-shifted compared to values presented in previous works. Particularly intriguing is that the error contours indicate a velocity discrepancy between the TiO results of this work and Nugroho et al. (2017), but may indicate agreement between our

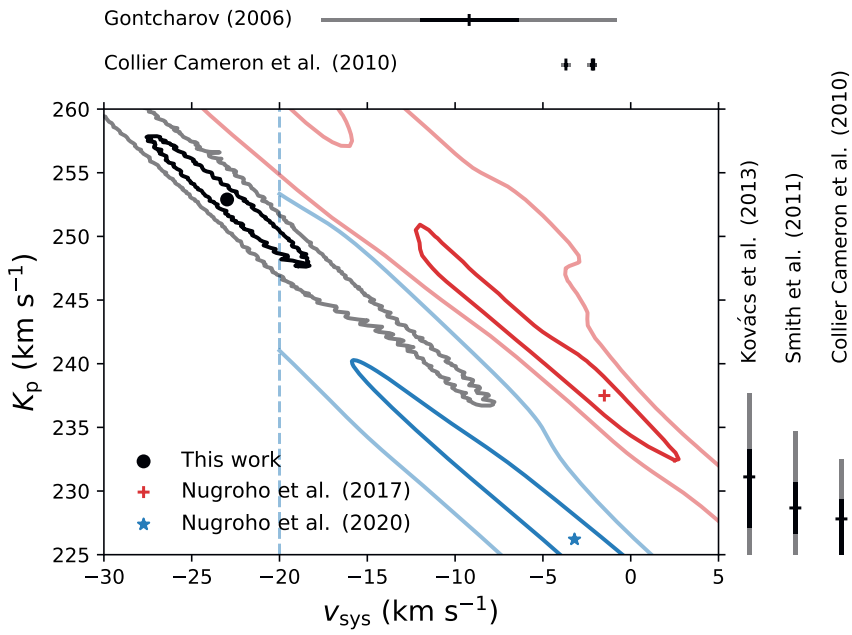

Figure 2.7. Comparison of various reported values of K_p and v_{sys} for the WASP-33 system. Our result is indicated by the circular marker, along with 1σ and 3σ contours in black and gray, respectively. The corresponding results from Figure 14 in Nugroho et al. (2017) for TiO are also plotted, with the location of their S/N peak denoted by the cross marker and the 1σ and 3σ contours shown in dark and light red. The S/N peak from the recent Nugroho et al. (2020a) Fe I detection is indicated by the star marker, with the 1σ and 3σ contours from the S/N matrix shown as solid dark blue and solid light blue lines. The $v_{sys} = -20$ km s^{-1} lower limit in their analysis caused by stellar pulsations is denoted by the dashed blue line. Previously reported values for v_{sys} (Gontcharov 2006; Collier Cameron et al. 2010) and K_p (Kovács et al. 2013; Smith et al. 2011; Collier Cameron et al. 2010) are shown above and to the right of the plot, with the strokes indicating the reported values, and the extended black and gray bars denoting the 1σ and 3σ errors, respectively. The negative errors for the K_p values are clipped for clarity.

TiO result and the Fe I detection of Nugroho et al. (2020a). We emphasize that all three analyses used the same HDS data of WASP-33b. Also puzzling is the fact that we derive a $v_{\rm sys} \sim -3$ to -5 km s^{-1} based solely on cross-correlating a rotationally broadened stellar model and the HDS data, which is comparable to previous studies.

2.5.2 Scenario II: Only the Nugroho et al. (2017) detection with Plez98 is valid

In light of these issues, another possible scenario is that the Nugroho et al. (2017) result is valid. While the corresponding values of $K_{\rm p}$ and $v_{\rm sys}$ that Nugroho et al. (2017) report are indeed in better agreement with previous works (Figure 2.7), we were unable to reproduce the same unambiguous detection of TiO emission in WASP-33b using our data treatment with their Plez98 model templates. For reference, we include the corresponding $K_{\rm p}$–$v_{\rm sys}$ matrices in Figures 2.12–2.13 and Figures 2.14–2.15 for the $\log_{10}(\mathrm{VMR_{TiO}}) = -9.0,\ -8.0$ cases, which are the fiducial volume mixing ratios from this work and Nugroho et al. (2017), respectively.

To estimate the recoverability of the TiO signal in WASP-33b with our methodology and the Nugroho et al. (2017) models based on the Plez98 line list, we performed the same ExoMol Toto injection described in Section 2.4.2 except we cross-correlated with a Plez98 TiO emission template from Nugroho et al. (2017). This way, we could compare the signal lost due to differences in the models. For the recovery, we used the $\log_{10}(\mathrm{VMR_{TiO}}) = -9.0$ contrast model presented in Nugroho et al. (2017), broadened and filtered in the same manner as our ExoMol Toto models to match our treatment of the data set.

The resulting global peak on the SVD6 $K_{\rm p}$–$v_{\rm sys}$ matrix for this Plez98 recovery of injected ExoMol Toto signal is $(K_{\rm p},\ v_{\rm sys}) = (255.4,\ -24.0)$ km s^{-1}, which is very close to the injected values. This demonstrates that the aforementioned $v_{\rm sys}$ discrepancy between this work and Nugroho et al. (2017) is not caused by differences in the model templates. Indeed, cross-correlating these $\log_{10}(\mathrm{VMR_{TiO}}) = -9.0$ models reveals a relative velocity offset of only 2.0 km s^{-1}, while cross-correlating the $\log_{10}(\mathrm{VMR_{TiO}}) = -9.0$ ExoMol Toto and $\log_{10}(\mathrm{VMR_{TiO}}) = -8.0$ Plez98 models indicates a relative velocity offset of just 1.5 km s^{-1}. As before, we calculated the noise on the correspondingly aligned one-dimensional CCF between ± 2775 km s^{-1}, excluding the inner ± 25 km s^{-1}, to get a 5.1σ detection with the Plez98 model from Nugroho et al. (2017). This represents a 54% loss compared to the 11.2σ signal recovered with our ExoMol Toto model. Scaling our 4.3σ detection using the ExoMol Toto

models and un-injected data, we estimate the TiO emission present in WASP-33b to be recoverable only at the $\lesssim 2\sigma$ level using the Plez98 spectral models from Nugroho et al. (2017) with our methodology.

2.5.3 Scenario III: Both detections are valid

A third possible, but unlikely, scenario is that our TiO emission signal found with the ExoMol TOTO spectral templates and the signature reported by Nugroho et al. (2017) using Plez98 models are both valid. In principle, the comparative completeness of the line lists may influence the retrieved signal. An increased quantity of weak TiO lines in our ExoMol TOTO model template may decrease the effective contrast of the TiO emission, thereby degrading the S/N. Our fixation of the temperature–pressure profile may also be a contributing factor. Differences in line strengths, line positions, and overall completeness between the ExoMol TOTO and Plez98 line lists may lead to substantially different line profiles even for similar atmospheric models (temperature–pressure profile, mean molecular weight profile, TiO volume mixing ratio, etc.), potentially leading to a weaker detection with the ExoMol TOTO models. Indeed, the normalized cross-correlation of the filtered $\log_{10}(\mathrm{VMR_{TiO}}) = -9.0$ Plez98 and ExoMol TOTO models peaks at a value of only 0.28, indicating substantial differences in the spectral models. Similar points are raised by Gandhi et al. (2020) when interpreting a discrepancy in detecting methane using two different line lists.

We attempted to recover our ExoMol TOTO TiO signal using models based on different temperature–pressure profiles to determine whether the signal strength substantially changes for different atmospheric structures. As limiting cases, we adopted fully inverted and non-inverted temperature–pressure profiles that span the same pressure (10^2–10^{-5} bar) and temperature (2700–3700 K) ranges as the Haynes et al. (2015) profile, but vary monotonically with a constant lapse rate. These are the same fully inverted and non-inverted profiles used by Nugroho et al. (2017). We followed the same procedure presented in Section 2.3 to create model spectra with *petitRADTRANS* for the two alternate atmospheric profiles, and subsequently cross-correlated these models with the processed data. In both the fully inverted and non-inverted cases, varying the total TiO abundance does not lead to significant differences in the final filtered models compared to that for the fiducial abundance of $\log_{10}(\mathrm{VMR_{TiO}}) = -9.0$, so we investigated only with the latter abundance. The fully inverted and non-inverted models recover very similar TiO emission signals, with the former giving a 4.3σ correlation and the latter giving a -4.4σ anti-correlation at K_p and v_sys values consistent with the 4.3σ peak recovered using the Haynes et al. (2015)

model. A more exhaustive investigation might determine an optimal inverted temperature–pressure profile that enables the recovery of a stronger TiO emission signal for models based on the ExoMol Toto line list, but such a study is beyond the scope of this work.

Nonetheless, the various points previously raised in this section pose serious challenges to this interpretation that both detections are valid. A degradation in contrast by additional weak lines and our fixation of the temperature–pressure profile would not explain our inability to recover the Nugroho et al. (2017) detection using their Plez98 models. Furthermore, we were unable to find an explanation for the offset in reported $v_{\rm sys}$.

2.5.4 Scenario IV: Both detections are false positives

The fourth possible scenario is that both TiO emission signals are in fact false positives. Herman et al. (2020) do not find evidence for TiO in either dayside or transmission spectra of WASP-33b. This interpretation has the advantage of explaining the noted discrepancies between this work and Nugroho et al. (2017). Such a scenario would raise questions regarding the current statistical techniques used to evaluate detection significance in high-resolution spectroscopy, as well as highlight the importance of reanalyzing detections using a diverse set of reduction methodologies and spectral models. In the end, further high-resolution spectra may be required to resolve the ambiguity surrounding the presence of TiO in WASP-33b.

Acknowledgments

D.B.S., P.M., and I.A.G.S. acknowledge support from the European Research Council under the European Union's Horizon 2020 research and innovation program under grant agreement No. 694513. S.K.N. would like to acknowledge support from UK Science Technology and Facility Council grant ST/P000312/1. P.M. acknowledges support from the European Research Council under the European Union's Horizon 2020 research and innovation program under grant agreement No. 832428. N.P.G. gratefully acknowledges support from Science Foundation Ireland and the Royal Society in the form of a University Research Fellowship.

2.A K_p–v_{sys} matrices

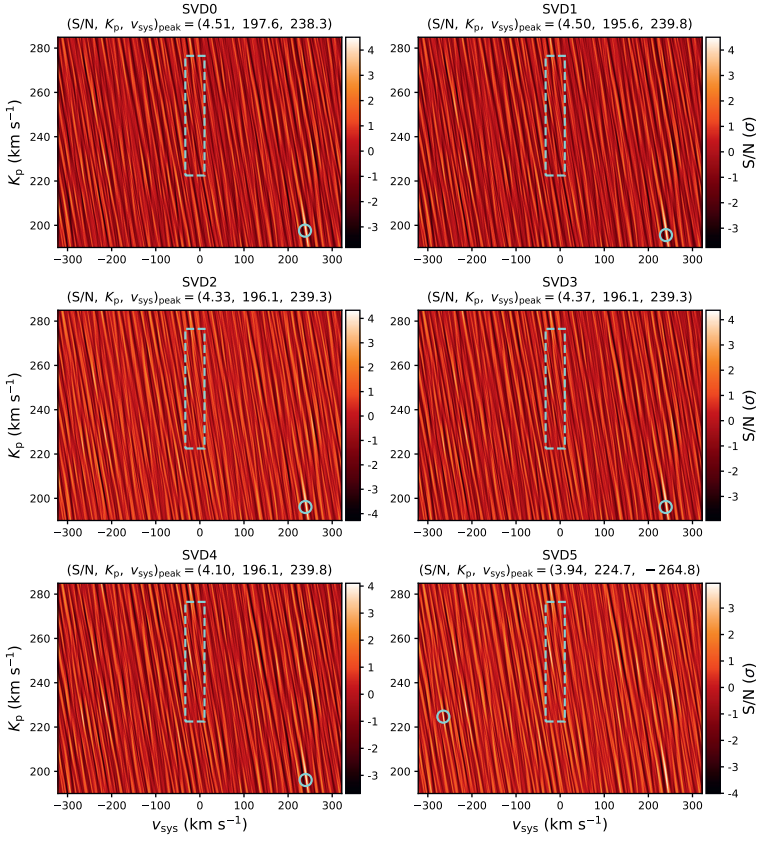

Figure 2.8. K_p–v_{sys} matrices of S/N values for the $\log_{10}(\mathrm{VMR_{TiO}}) = -9.0$ ExoMol TOTO model, as described in Section 2.3.3. Each panel corresponds to the matrix for a different SVD iteration (0–5), indicated above each panel. The strongest peak is marked on each matrix with a cyan ring and noted above each panel with the corresponding values of K_p and v_{sys}. The dashed cyan box indicates the region where peaks must be found to be considered "significant", as described in Section 2.4.

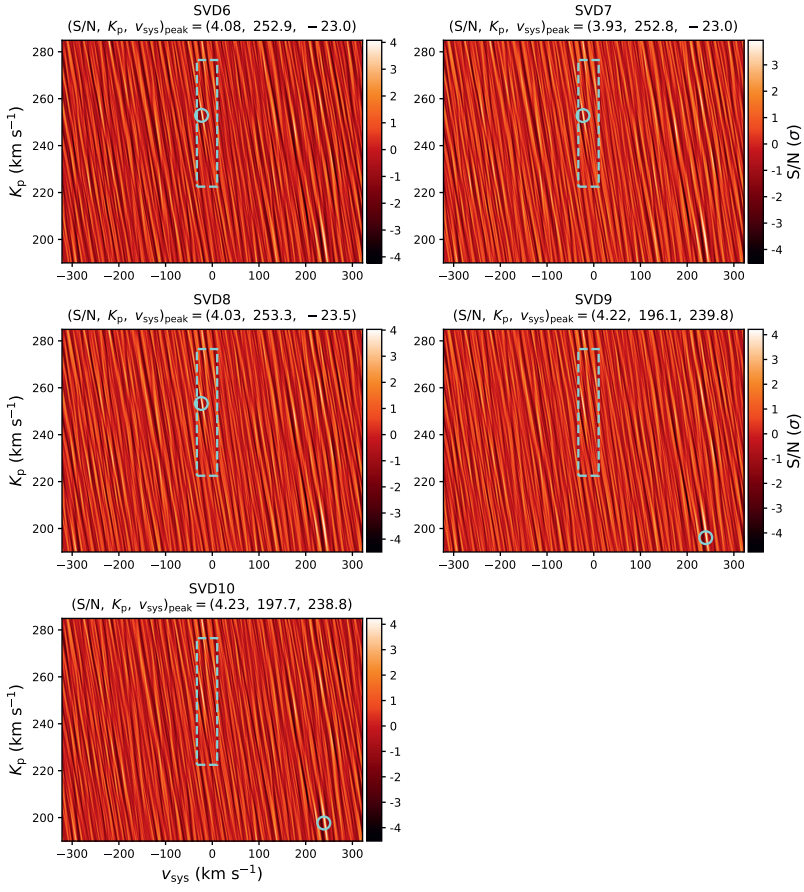

Figure 2.9. Same as Figure 2.8, but for SVD iterations 6–10.

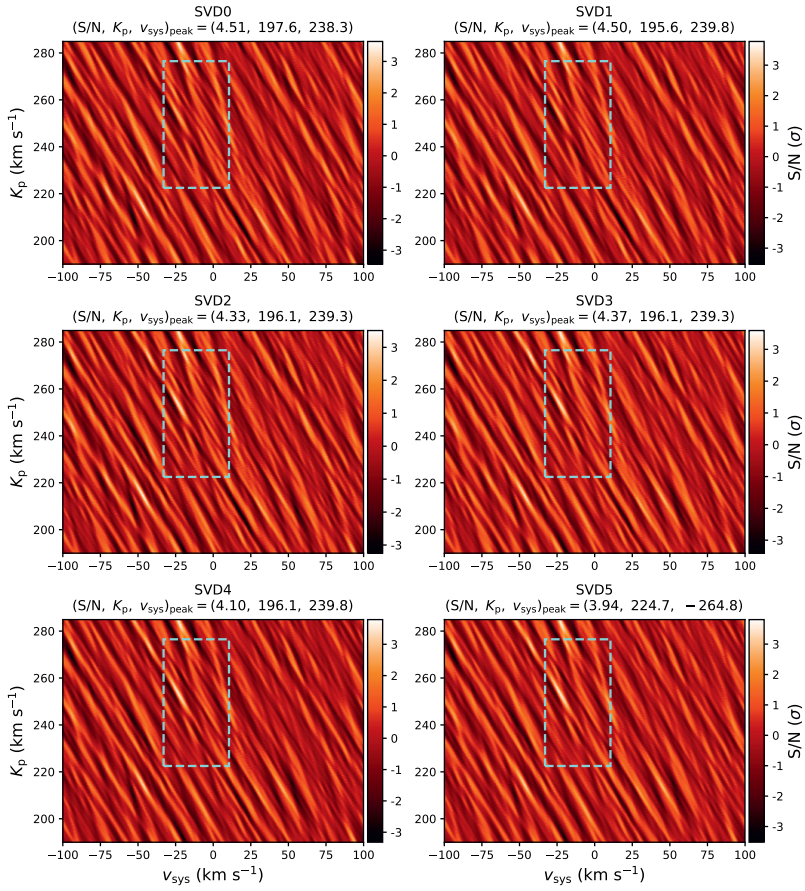

Figure 2.10. Same as Figure 2.8, but with the $v_{\rm sys}$-axis restricted to values within ± 100 km s^{-1} for clarity. While the S/N peak printed above each panel refers to that for the full $v_{\rm sys}$ range, the colorbar scaling is based on the S/N values on this restricted $v_{\rm sys}$ range.

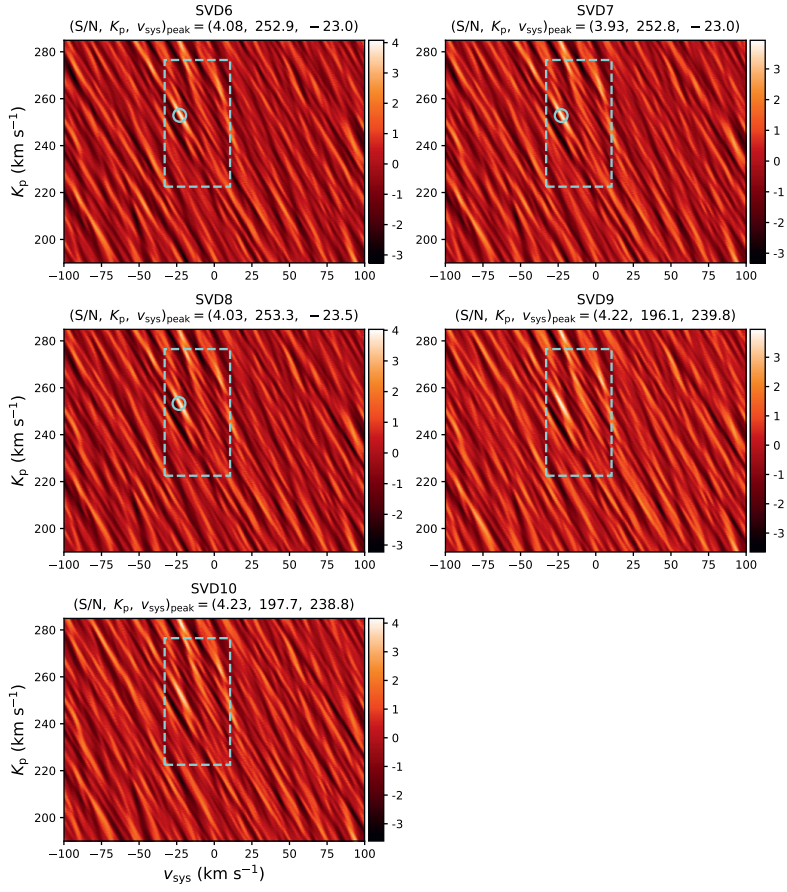

Figure 2.11. Same as Figure 2.10, but for SVD iterations 6–10.

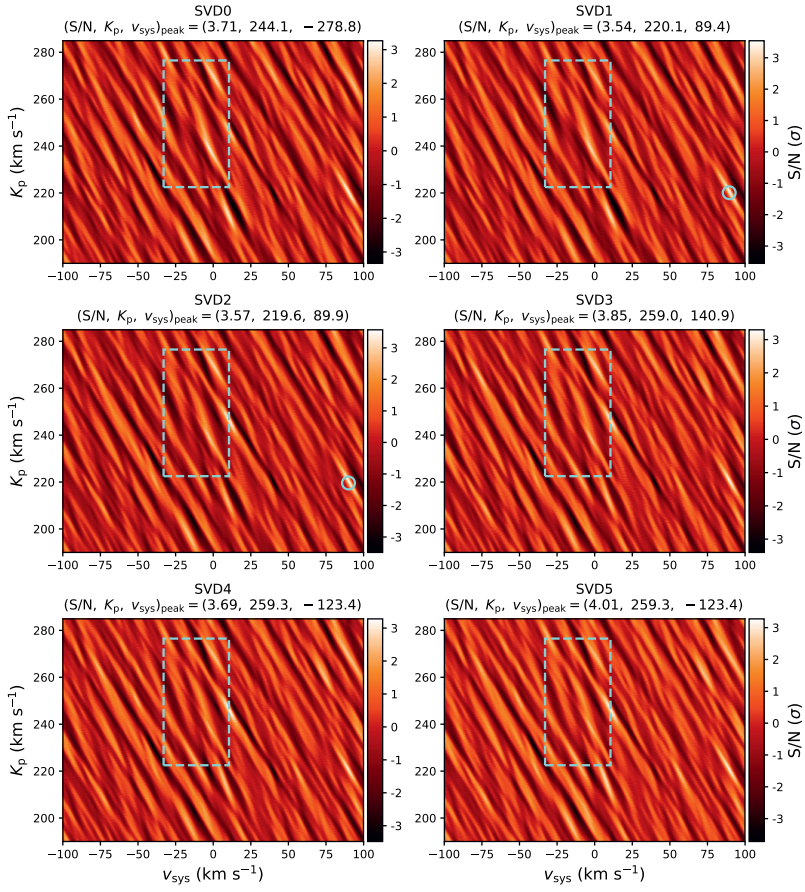

Figure 2.12. K_p–v_{sys} matrices of S/N values for the $\log_{10}(\mathrm{VMR_{TiO}}) = -9.0$ Plez98 model from Nugroho et al. (2017), with the v_{sys}-axis restricted to values within ± 100 km s^{-1} for clarity. Each panel corresponds to the matrix for a different SVD iteration (0–5), indicated above each panel. The strongest peak on the full v_{sys} range is noted above each panel with the corresponding values of K_p and v_{sys}. Where applicable, this peak is also marked on each matrix with a cyan ring. The dashed cyan box indicates the region where peaks must be found to be considered significant, as described in Section 2.4. The colorbar binning is based on the local S/N minimum and maximum on this restricted v_{sys} range.

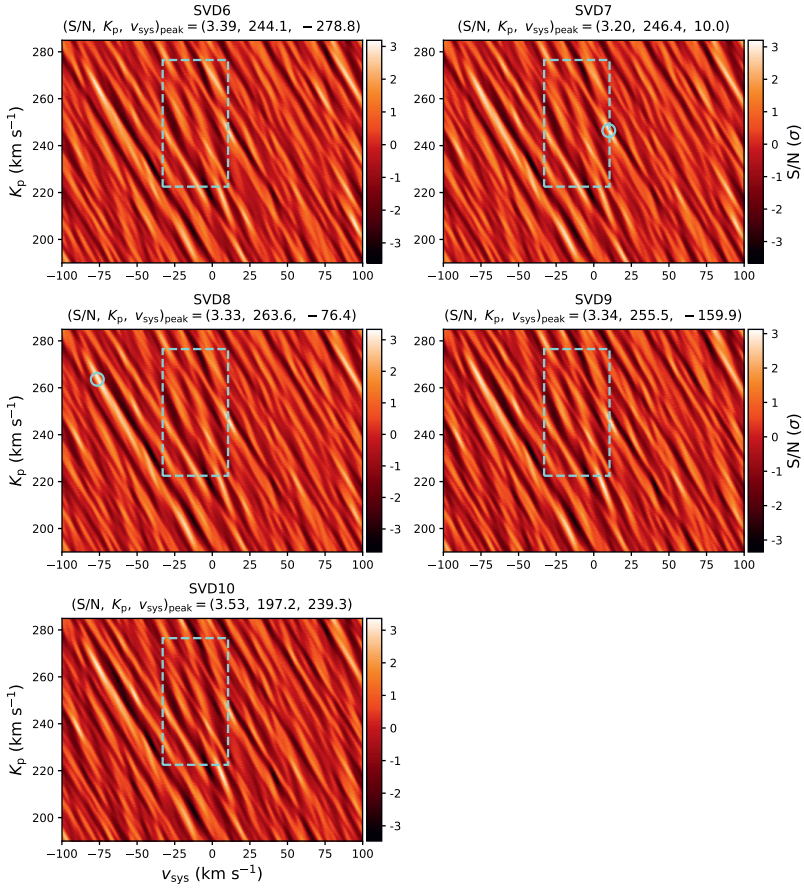

Figure 2.13. Same as Figure 2.12, but for SVD iterations 6–10.

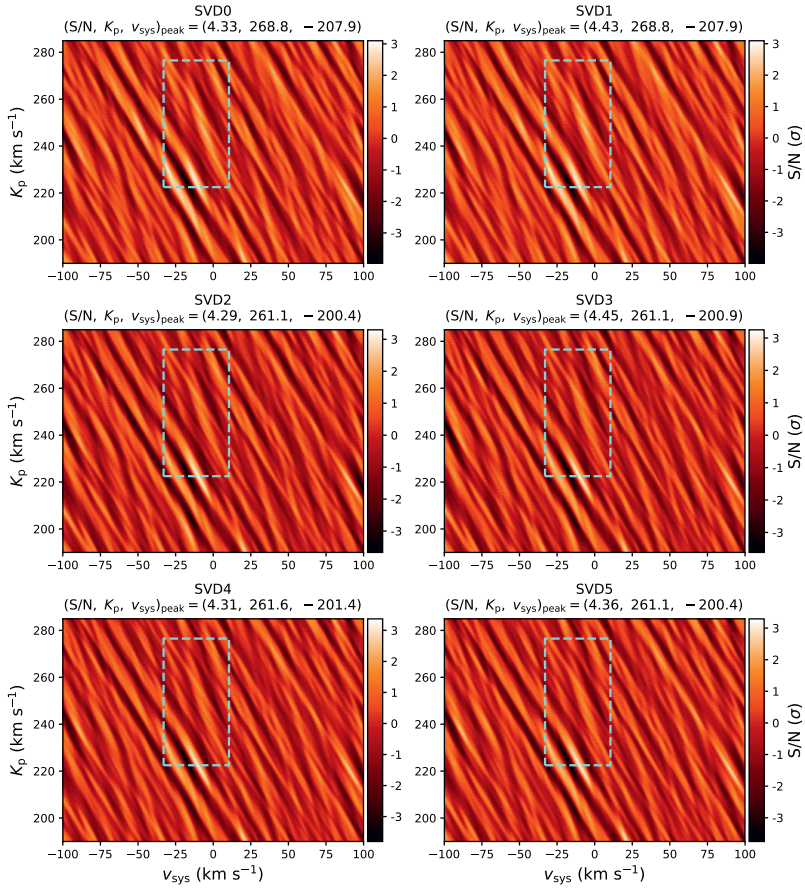

Figure 2.14. K_p–v_{sys} matrices of S/N values for the $\log_{10}(\mathrm{VMR_{TiO}}) = -8.0$ Plez98 model from Nugroho et al. (2017), with the v_{sys}-axis restricted to values within ± 100 km s^{-1} for clarity. Each panel corresponds to the matrix for a different SVD iteration (0–5), indicated above each panel. The strongest peak on the full v_{sys} range is noted above each panel with the corresponding values of K_p and v_{sys}. Where applicable, this peak is also marked on each matrix with a cyan ring. The dashed cyan box indicates the region where peaks must be found to be considered significant, as described in Section 2.4. The colorbar binning is based on the local S/N minimum and maximum on this restricted v_{sys} range.

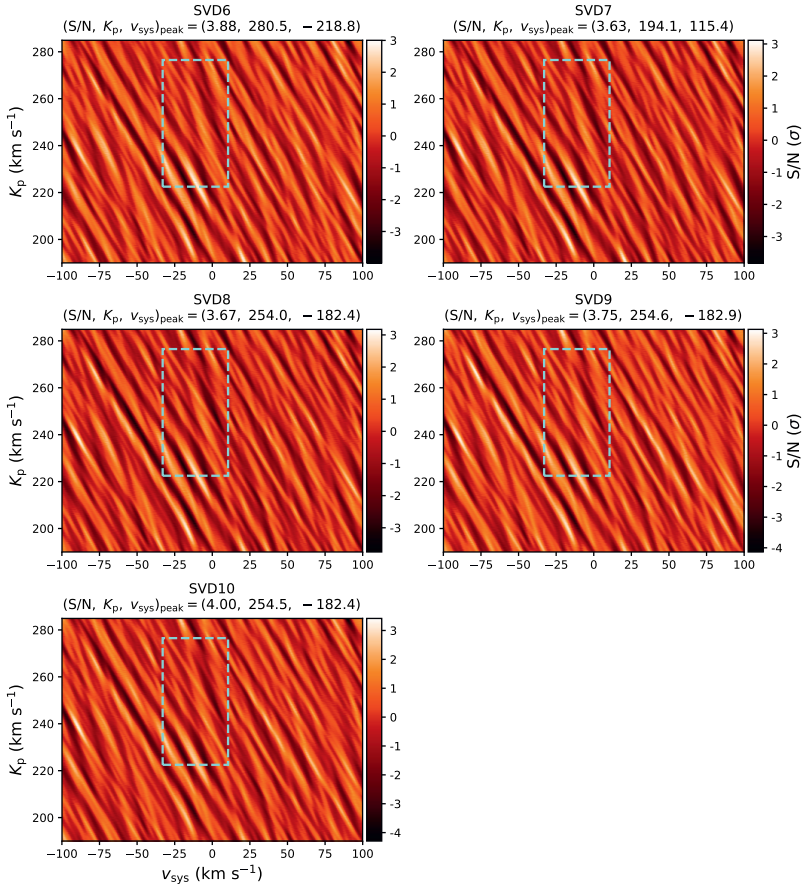

Figure 2.15. Same as Figure 2.14, but for SVD iterations 6–10.

Chapter 3

Measuring titanium isotope ratios in exoplanet atmospheres

Dilovan B. Serindag, Ignas A. G. Snellen, and Paul Mollière
Published in Astronomy & Astrophysics, 655, A69 (2021)

Abstract

Context. Measurements of relative isotope abundances can provide unique insights into the formation and evolution histories of celestial bodies, tracing various radiative, chemical, nuclear, and physical processes. In this regard, the five stable isotopes of titanium are particularly interesting. They are used to study the early history of the Solar System, and their different nucleosynthetic origins help constrain Galactic chemical models. Additionally, titanium's minor isotopes are relatively abundant compared to those of other elements, making them more accessible for challenging observations, such as those of exoplanet atmospheres.

Aims. We aim to assess the feasibility of performing titanium isotope measurements in exoplanet atmospheres. Specifically, we are interested in understanding whether processing techniques used for high-resolution spectroscopy, which remove continuum information about the planet spectrum, affect the derived isotope ratios. We also want to estimate the signal-to-noise requirements for future observations.

Methods. We used an archival high-dispersion CARMENES spectrum of the M-dwarf GJ 1002 as a proxy for an exoplanet observed at very high signal-to-noise. Both a narrow (7045–7090 Å) and wide (7045–7500 Å) wavelength region were defined for which spectral retrievals were performed using *petitRADTRANS* models, resulting in isotope ratios and uncertainties. These retrievals were repeated on the spectrum with its continuum removed to mimic typical high-dispersion exoplanet observations. The CARMENES spectrum was subsequently degraded by adding varying levels of Gaussian noise to estimate the signal-to-noise requirements for future exoplanet atmospheric observations.

Results. The relative abundances of all minor Ti isotopes are found to be slightly enhanced compared to terrestrial values. A loss of continuum information from broadband filtering of the stellar spectrum has little effect on the isotope ratios. For the wide wavelength range, a spectrum with a signal-to-noise of 5 is required to determine the isotope ratios with relative errors $\lesssim$10%. Super Jupiters at large angular separations from their host star are the most accessible exoplanets, requiring about an hour of observing time on 8-meter-class telescopes, and less than a minute of observing time with the future Extremely Large Telescope.

3.1 Introduction

The relative abundances of isotopes in a given environment are determined by various radiative, chemical, nuclear, and physical processes that occurred throughout its history. Understanding the effects of these processes on the isotope ratios can therefore trace the formation and evolution of astronomical objects. For instance, preferential Jeans escape of protium (^{1}H) and bombardment by deuterium-rich comets are invoked to explain the enhanced deuterium-to-hydrogen (D/H) ratio[1] of Earth's ocean water compared to the protosolar nebula (e.g., Genda & Ikoma 2008; Hartogh et al. 2011). Recently, work has begun to plan and perform isotope measurements in exoplanet atmospheres. For instance, Lincowski et al. (2019) and Morley et al. (2019) discuss the feasibility of determining hydrogen and oxygen isotope ratios in exoplanet atmospheres using the upcoming James Webb Space Telescope. Mollière & Snellen (2019) studied the efficacy of determining isotope ratios using ground-based high-resolution ($\mathcal{R} \sim 100,000$) spectroscopy, and conclude that while D/H measurements will only be possible with the future Extremely Large Telescope, current 8-m-class telescopes should be capable of determining carbon isotope ratios in exoplanets. Indeed, Zhang et al. (2021a) measured an isotope ratio in an exoplanet for the first time, finding a super-terrestrial ^{13}C/^{12}C value for the young super-Jupiter TYC 8998-760-1 b using medium-resolution ($\mathcal{R} \sim 4500$) integral field spectroscopy. Since this planet orbits well beyond the CO snowline, they suggest its enhancement in ^{13}C could be due to accretion of ices enriched in ^{13}C by isotope fractionation processes. This may mark the beginning of using isotope ratios to probe formation histories of planets beyond our Solar System.

Titanium has five stable isotopes — ^{46}Ti, ^{47}Ti, ^{48}Ti, ^{49}Ti, and ^{50}Ti — with telluric relative abundances of 8.25%, 7.44%, 73.72%, 5.41%, and 5.18% (Meija et al. 2016). With about 25% of its atoms approximately equally partitioned among the minor (less abundant) isotopes, Ti compares favorably to hydrogen (Wood et al. 2004; Linsky et al. 2006; Altwegg et al. 2015, and the references therein), carbon (Milam et al. 2005; Asplund et al. 2009; Meija et al. 2016), and oxygen (Ayres et al. 2013, and the references therein; Romano et al. 2017, and the references therein), whose minor isotopes have relative abundances $\lesssim$2% in the Solar System and local interstellar medium. The isotopes of titanium have different nucleosynthetic origins, with oxygen and silicon burning in massive stars thought to be the main source of ^{46}Ti and ^{47}Ti, while ^{48}Ti, ^{49}Ti, and ^{50}Ti are thought to be mostly produced in type Ia and/or type II supernovae (Hughes

[1]Throughout this chapter, we exclusively refer to number abundance ratios. For two species, A and B, we abbreviate this by writing A/B.

et al. 2008, and the references therein). It is therefore expected that stars that formed in different environments may exhibit variations in Ti isotope ratios of a factor ∼2 or more (Hughes et al. 2008). Indeed, observational studies targeting TiO isotopologue[2] features in K- and M-dwarfs have determined relative deviations of tens of percent in Ti isotope ratios compared to terrestrial values (Wyckoff & Wehinger 1972; Lambert & Luck 1977; Clegg et al. 1979; Chavez & Lambert 2009; Pavlenko et al. 2020). Such measurements have, in turn, been used to constrain Galactic chemical models (e.g., Hughes et al. 2008).

Interestingly, relative abundances of Ti isotopes are also used to study the early evolution of the Solar System. For instance, variations in isotope ratios across different populations of meteorites and other Solar System bodies are used to study (in)homogeneity and thermal processing in the solar protoplanetary disk (e.g., Leya et al. 2008; Trinquier et al. 2009). Conversely, the similarity in telluric and lunar Ti isotope ratios places constraints on Moon formation theories (Zhang et al. 2012). We note, however, that the relative variations reported in the Solar System are $\lesssim$0.1%, which is orders of magnitude smaller than those found in stellar populations.

Both close-orbiting and young gas giants can have sufficiently high temperatures ($T \gtrsim$ 1500–2000 K) to allow gaseous TiO to persist in their atmospheres (e.g., Hubeny et al. 2003; Fortney et al. 2008; Spiegel et al. 2009; Gandhi & Madhusudhan 2019), possibly enabling similar Ti isotope analyses of these objects. Indeed, there is increasing evidence for TiO in hot Jupiters from transmission and dayside emission spectra (e.g., Nugroho et al. 2017; Serindag et al. 2021; Cont et al. 2021; Chen et al. 2021). The youngest super Jupiters, which are still hot from their formation, are also expected to show TiO features, similar to brown dwarfs and M-dwarf stars. In fact, TiO band heads are clearly visible in the medium-resolution MUSE optical spectrum of the young, widely-orbiting super-Jupiter GQ Lupi b (Stolker et al., in prep).

In this chapter, we use an archival high-dispersion CARMENES spectrum of the M-dwarf GJ 1002 as a proxy for a gas-giant exoplanet observed at extremely high signal-to-noise, and assess the feasibility of performing titanium isotope measurements in exoplanet atmospheres. We investigate how the derived isotope ratios are impacted by different wavelength coverage and a loss of continuum information, which is a common effect of the processing techniques for high-resolution spectroscopy of exoplanet atmospheres. We also estimate what spectral signal-to-noise ratios (S/Ns) are needed to perform such analyses for exoplanets, along with the corresponding exposure times for current 8-m-

[2]Molecules comprised of different atomic isotopes, for instance, ^{47}Ti^{16}O versus ^{48}Ti^{16}O.

class telescopes and the future Extremely Large Telescope. In Section 3.2 we describe the high-resolution stellar spectrum we use in this work. We present the high-resolution TiO model spectra in Section 3.3 and outline our fitting methodology in Section 3.4. We present and discuss the results of our analyses in Sections 3.5 and 3.6, before summarizing our work in Section 3.7.

3.2 High-resolution TiO spectral data

3.2.1 CARMENES spectrum of GJ 1002

We use a single high-resolution archival[3] spectrum of the M5.5V (Walker 1983) star GJ 1002 taken on 18 November 2016 using the CARMENES spectrograph on the 3.5-m Calar Alto Telescope. CARMENES (Quirrenbach et al. 2014) consists of two echelle spectrographs in the visible and near-infrared wavelength regime. The archival observation is a 1238-s exposure in the visual channel, covering 5200–10,500 Å at a resolving power of $\mathcal{R} = 94,600$ ($\approx$3 km s^{-1}). The automated CARACAL pipeline (Caballero et al. 2016; Zechmeister et al. 2018) performs the initial data processing including bias correction, order extraction, and wavelength calibration. The archival pipeline product contains the topocentric wavelengths, fluxes, and errors for the 61 orders of the visual channel.

We isolated wavelengths 7000–7600 Å from nine orders and removed all pixels (0.02%) with nonfinite flux values. To mitigate the influence of telluric contamination, we also removed all wavelength bins (9%) with a telluric transmission value $\leq$0.98, based on the ESO SkyCalc model (Noll et al. 2012; Jones et al. 2013) with a precipitable water vapor of 2.5 mm. We subsequently shifted the spectrum to the stellar rest frame and divided the flux and error values by the mean flux level in the spectral range 7045–7050 Å preceding the red-degraded γ-system (0,0) band head of TiO at 7054 Å. This wavelength range is similar to those used as continuum levels in previous studies fitting high-resolution stellar TiO features (Clegg et al. 1979; Valenti et al. 1998; Chavez & Lambert 2009). The top left panel of Figure 3.1 shows the normalized spectrum (hereafter, unfiltered spectrum) over the wavelength range 7045–7500 Å.

To mimic the standard treatment of high-resolution spectra in exoplanet atmosphere analyses, we performed a high-pass filter which results in the loss of continuum information. For each wavelength bin, we subtracted the mean flux value in a boxcar with a full width of 0.60 Å ($\approx$25 km s^{-1}). Since the pixel spacing is nonuniform in both wavelength and velocity space, we only filtered

[3]Based on data from the CARMENES data archive at CAB (INTA-CSIC).

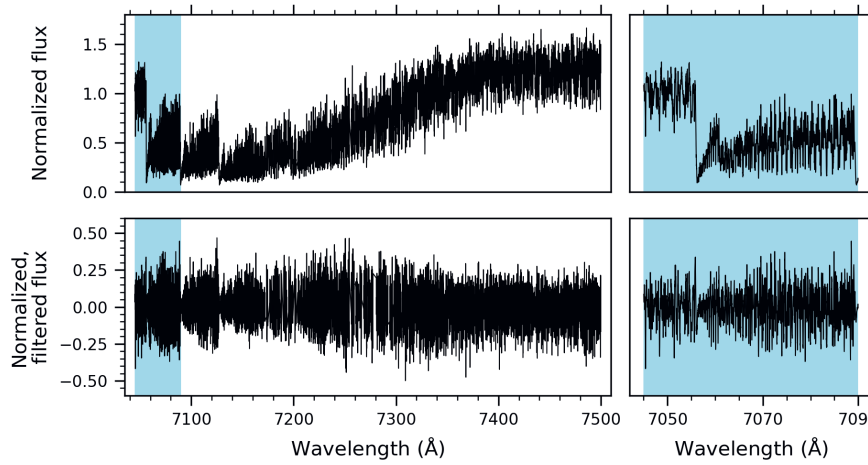

Figure 3.1. *Top left panel*: unfiltered CARMENES spectrum of GJ 1002 over the wide wavelength range 7045–7500 Å. The narrow wavelength range 7045–7090 Å is indicated by the blue shading. *Top right panel*: same as top left panel, but plotting only the narrow wavelength range for clarity. *Bottom left panel*: broadband-filtered CARMENES spectrum of GJ 1002 over the wide wavelength range. *Bottom right panel*: same as bottom left panel, but for the narrow wavelength range.

a given pixel if its boxcar contains more than half of the expected number of pixels based on the average wavelength sampling. This results in 2% of the pixels being excluded. This broadband-filtered spectrum on 7045–7500 Å is shown in the bottom left panel of Figure 3.1.

3.2.2 Choice of wavelength range for TiO fitting

Most of the previous studies that used TiO to determine stellar Ti isotope ratios used the wavelength range ∼7050–7100 Å, which contains strong features of the TiO γ-system (0,0) bands. Lambert & Mallia (1972), Wyckoff & Wehinger (1972), Lambert & Luck (1977), and Chavez & Lambert (2009) all chose a range with a relatively low line density between the γ(0,0) band heads at 7054 Å and 7089 Å. Clegg et al. (1979) used a similar spectral range, but only for

stars with a spectral type earlier than M4. For M4 stars and later, they instead analyzed the regions around the γ-system (0,1) band at 7589 Å and δ-system (0,0) band around 8900 Å, which are less saturated.

More recently, Pavlenko et al. (2020) compared the suitability of various spectral ranges in the optical and near-infrared for TiO isotopologue analysis, and they argue that the spectral region 7580–7594 Å, including the γ(0,1) band head at 7589 Å, is preferable to the commonly used spectral window encompassing the γ(0,0) band. Specifically, they note that while the γ(0,0) band head at 7054 Å is a blend of features from all five TiO isotopologues, the γ(0,1) band heads of ^{49}TiO and ^{50}TiO are blue-shifted out of the stronger, red-degraded ^{48}TiO band head at 7589 Å. Further, they note that the stellar flux for late-type stars is higher at these redder wavelengths than at 7054 Å. This is also expected to be the case for exoplanets. However, a major drawback of using the region surrounding the γ(0,1) band at 7589 Å is the presence of the strong telluric O_2 *A* band at 7590 Å. As Pavlenko et al. (2020) point out, the separation between the telluric and TiO band heads — and thus the level of telluric contamination of the TiO band — depends on the relative velocity between the target and telescope.

Since the primary objective of this work is to determine the feasibility of deriving accurate Ti isotope ratios from TiO features in the spectra of gas-giant exoplanets, we opt to entirely avoid analyzing spectral regions near the strong O_2 *A* band. Instead, similar to the majority of previous studies, we performed spectral fitting using the range 7045–7090 Å (hereafter, narrow range), shown for the unfiltered and broadband-filtered cases in the top right and bottom right panels of Figure 3.1. To investigate whether including more, albeit weaker, TiO features affects the spectral fitting results for GJ 1002 or enables more accurate results for noise-degraded cases, we also analyze the spectral range 7045–7500 Å (hereafter, wide range). The top left and bottom left panels of Figure 3.1 show the unfiltered and broadband-filtered spectrum, respectively, over this wide wavelength range. For comparison, the narrow range is highlighted in blue.

3.3 High-resolution TiO spectral models

We used the radiative transfer code *petitRADTRANS* (Mollière et al. 2019) to model the TiO spectrum of GJ 1002. While originally developed to study exoplanets, the high-resolution emission spectrum functionality of *petitRADTRANS* is also appropriate for modeling stellar spectra. We modeled the at-

mosphere of GJ 1002 in 70 layers from 10^5 to 10^{-6} bar assuming a constant, solar mean molecular weight of 2.33. We linearly interpolated the temperature–pressure (T–P) profiles of the MARCS plane-parallel standard-composition stellar model atmospheres grid (Gustafsson et al. 2008) to the parameters of GJ 1002. Specifically, we adopted a microturbulent velocity $v_{\rm turb} = 2$ km s^{-1} and fixed the remaining stellar parameters based on their literature values from Rajpurohit et al. (2018): $T_{\rm eff} = 3100$ K, $\log g = +5.5$, and [M/H] = +0.20. Since the MARCS models do not span a pressure range comparable to our atmospheric model, we subsequently extrapolated the T–P profile based on linear fits in $\log T$–$\log P$ space. To reflect the maximum temperature for which we calculated TiO opacities, we imposed a temperature upper limit of 4000 K.

We only included spectroscopic contributions from the five main isotopologues[4] of TiO, as these dominate the M-dwarf optical spectrum. We utilized the recently released ExoMol Toto line list to calculate TiO opacities. Compared to other commonly used TiO line lists, ExoMol Toto reproduces the TiO features in high-resolution M-dwarf spectra better for both the main (^{48}TiO) and minor isotopologues due to the inclusion of more accurate experimental energy levels in the line list calculations (McKemmish et al. 2019; Pavlenko et al. 2020). We used the method outlined in Appendix A of Mollière et al. (2015) to calculate TiO opacities up to 4000 K on a high-resolution wavelength grid ($\lambda/d\lambda = 10^6$). For all TiO isotopologues, we assumed a constant volume mixing ratio (VMR) at each pressure layer in our model atmosphere.

To facilitate a better fit, we performed similar processing steps on the *petitRADTRANS* models as we used on the CARMENES data. We broadened the models to the CARMENES resolving power and subsequently interpolated them onto the wavelength sampling of the data. We then normalized the model spectra to their mean flux value in the range 7045–7050 Å. If we were fitting the broadband-filtered CARMENES spectrum, we also performed a boxcar filtering identical to that described in Section 3.2.1. As an example, Figure 3.6 plots an unfiltered model (dashed black line) over a limited wavelength range, calculated using TiO isotopologue abundances retrieved for GJ 1002 (see Sections 4 and 5). Also shown are the flux contributions of the individual TiO isotopologues (solid lines), demonstrating their influence on the composite model spectrum.

[4]We only differentiate TiO isotopologues based on the stable Ti isotopes. The oxygen isotope fractionation is comparatively negligible.

3.4 Fitting TiO isotopologue abundances

We used the EMCEE implementation (Foreman-Mackey et al. 2013) of the Goodman & Weare (2010) affine-invariant Markov chain Monte Carlo (MCMC) ensemble sampler to directly fit the processed CARMENES spectrum (Section 3.2.1) using the similarly processed *petitRADTRANS* models (Section 3.3). Following the methods presented by Brogi & Line (2019) and Gibson et al. (2020), we adopted a log-likelihood function of the form

$$\ln \mathcal{L} = -N \ln \beta - \frac{1}{2} \sum_{i=1}^{N} \left(\frac{d_i - m_i}{\beta \, \sigma_i} \right)^2, \tag{3.1}$$

where N is the number of pixels, d_i and m_i are the data and model flux values for the ith pixel, σ_i is the CARMENES error of the ith pixel, and β is a wavelength-invariant scaling factor for the uncertainties. The purpose of the latter term is to allow for the possibility that the CARMENES errors are underestimated and to attempt to account for systematic uncertainties in our models.

Our model consists of six fitted parameters: β and the $\log_{10}$ (VMR) for each TiO isotopologue[5]. We adopted uniform priors: [1, 100] for β, [−10, −6] for $\log_{10}(\mathrm{VMR}_{48})$, and [−13, −6] for each minor isotopologue's $\log_{10}$ (VMR). The choice of bounds for the TiO abundances allows for ratios relative to the main isotopologue ^{48}TiO of [10^{-3}, 1], which is essentially zero to unity. While we did not fit for T_{eff}, $\log g$, [M/H], v_{turb}, and the mean molecular weight (see Section 3.3), we did perform additional retrievals to estimate the impact that uncertainties in these parameters have on the TiO results (see Section 3.6.1).

For each fit, we performed two MCMC runs in sequence. For the first, we initialized 50 walkers uniformly within the bounds of the prior for each fitted parameter, and we ran the sampler for 500 steps, corresponding to 25,000 model evaluations. We then initialized 50 walkers in a Gaussian ball around the best-fitting set of parameters from the first run and evolved the sampler again for 1000 steps (50,000 model evaluations). We visually inspected and removed the section of the second run preceding convergence. The resulting clipped, converged chain is the set of posterior samples used in our analysis.

[5]For brevity, we denote the $\log_{10}$ (VMR) for a given isotopologue ^{i}TiO as $\log_{10}(\mathrm{VMR_i})$.

3.5 Results

3.5.1 Ti isotope ratios for the M-dwarf GJ 1002

Using the framework presented in Section 3.4, we performed multiple retrievals of the TiO isotopologue abundances in the M-dwarf GJ 1002 to assess the impact of different methodologies for wavelength range and filtering. As mentioned in Section 3.2.2, we fit both a narrow (7045–7090 Å) and wide (7045–7500 Å) spectral range to determine the influence of including more TiO lines on the retrieved TiO abundances and Ti isotope ratios. We also performed retrievals on both the unfiltered and broadband-filtered versions of the CARMENES data to assess whether the loss of continuum information inherent to high-resolution studies of exoplanet spectra affects the results. For each methodology — narrow and unfiltered spectrum, narrow and broadband-filtered spectrum, wide and unfiltered spectrum, wide and broadband-filtered spectrum — we performed three independent retrievals to demonstrate consistency, leading to a total of 12 MCMC retrievals. In all 12 cases, the second MCMC run provides a uni-modal solution with constrained posteriors for all six fitted parameters.

The first column of Figure 3.2 plots the fitted TiO abundances for the various MCMC retrievals. Each panel corresponds to the $\log_{10}$ (VMR) for a different TiO isotopologue, with the mean posterior value for a given fit shown by the red marker and the 1σ and 3σ errors indicated by the black and gray bars, respectively. For reference, the mean values and 1σ errors for all fitted parameters, including β, are given in Table 3.1. We also derived sets of posteriors for the isotope ratios relative to Ti, ^{48}Ti, and ^{46}Ti. The corresponding mean and 1σ errors are also provided in Table 3.1, and plotted in the second, third, and fourth columns of Figure 3.2. We only provide the results of the first retrieval for each methodology in Figure 3.2 and Table 3.1 because the second and third retrievals give very similar values.

3.5.2 Ti isotope ratios from noise-degraded spectra

To assess the effectiveness of this technique for deriving Ti isotope ratios in the gas-giant exoplanet case, we degraded the CARMENES spectrum of GJ 1002 with varying levels of noise and reran the MCMC fitting. To achieve a given planet S/N on the wavelength range used for normalization (7045–7050 Å), we added white noise to the pipeline-reduced CARMENES spectrum by sampling a zero-mean normal distribution with a standard deviation equal to the average flux value on 7045–7050 Å divided by the desired S/N. We subsequently

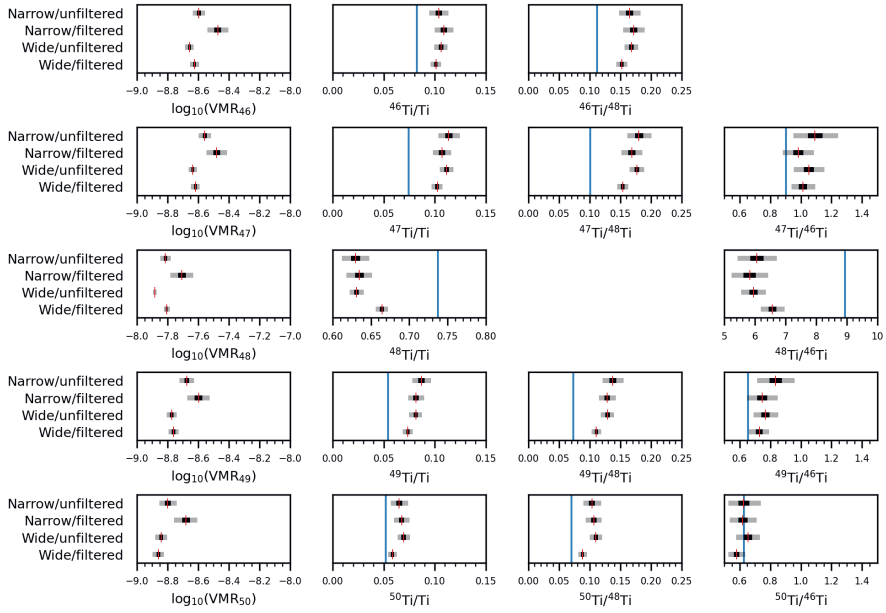

Figure 3.2. Results of the MCMC retrievals of TiO features in the CARMENES spectrum of GJ 1002 using the narrow and wide spectral ranges and the unfiltered and broadband-filtered versions of the data. Each panel plots the results for a different parameter, which are grouped in columns. The first column contains panels for the fitted $\log_{10}$ (VMR) of the five TiO isotopologues. The second, third, and fourth columns contain panels for the derived isotope ratios relative to Ti, ^{48}Ti, and ^{46}Ti, respectively. In each panel, the mean parameter value from each MCMC fitting is indicated by a red marker while the 1σ and 3σ errors are indicated by black and gray bars, respectively. For the panels comparing abundance ratios, we indicate the corresponding terrestrial value with a vertical blue line.

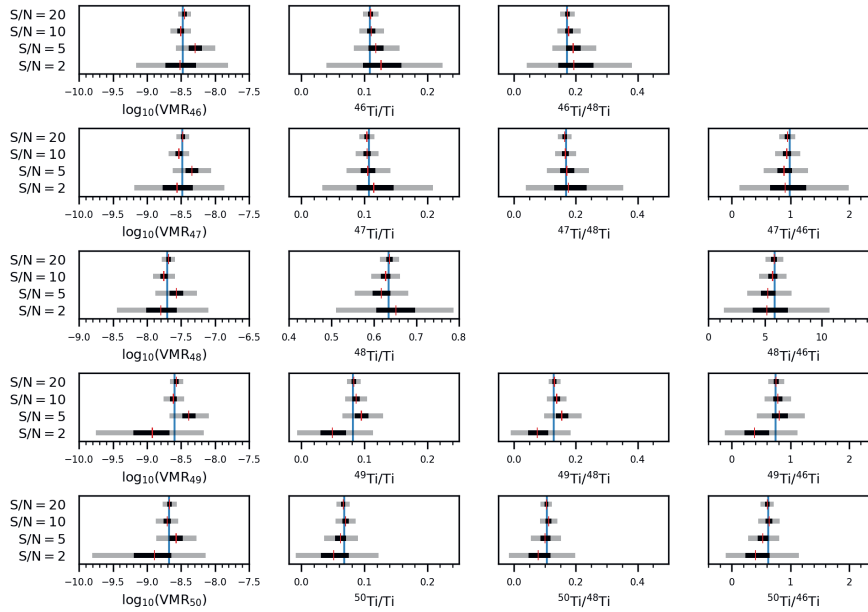

Figure 3.3. Same as Figure 3.2, but for the MCMC retrievals of TiO features in the narrow, broadband-filtered CARMENES spectrum of GJ 1002 with various levels of noise added. The results from the retrieval of the narrow, broadband-filtered spectrum without added noise are shown by the vertical blue lines.

performed the same telluric-contaminated pixel removal, reference frame shift, normalization, and high-pass filtering described in Section 3.2.1. We then used the same MCMC retrieval procedure described in Section 3.4 to fit the TiO isotopologue features for both the narrow and wide wavelength ranges in each noise-degraded, broadband-filtered data set. As before, we ran each fitting three times to ensure consistency of the results.

Similar to Figure 3.2, we present the fitted TiO isotopologue abundance values for each noise case in the first columns of Figures 3.3 and 3.4 for the narrow and broadband-filtered spectrum, and the wide and broadband-filtered spectrum, respectively. The second, third, and fourth columns of these figures show the derived isotope ratios relative to Ti, ^{48}Ti, and ^{46}Ti, respectively. For the narrow and broadband-filtered case, we present the results for spectra degraded

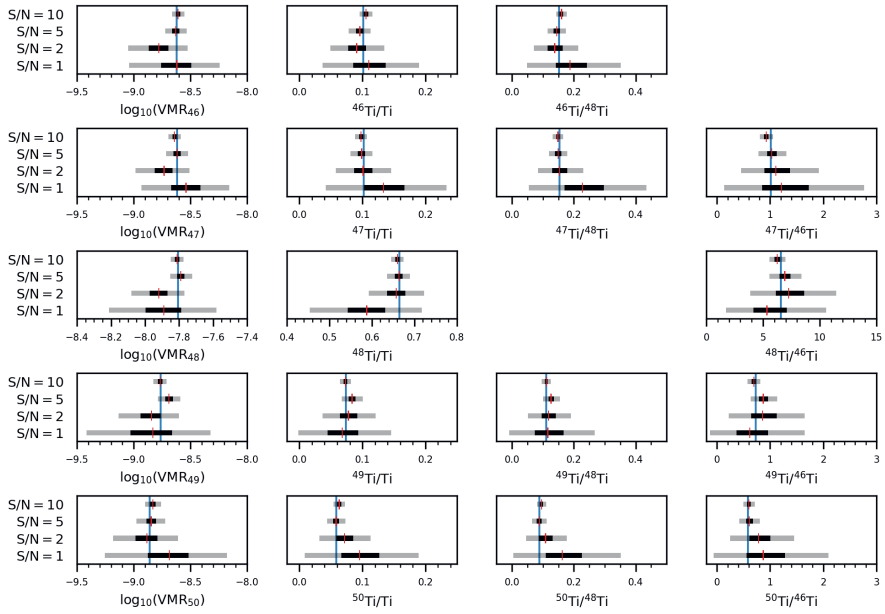

Figure 3.4. Same as Figure 3.3, but for the MCMC retrievals performed on the wide, broadband-filtered CARMENES spectrum of GJ 1002.

to a S/N of 20, 10, 5, and 2, while for the wide and broadband-filtered case we show the results for spectra degraded to a S/N of 10, 5, 2, and 1. Again, because the results of the three retrievals for each noise case are very similar, we only provide the values from the first retrieval in Figures 3.3 and 3.4.

3.6 Discussion

3.6.1 Effects of wavelength range and broadband filtering

Small systematic effects ($\lesssim$0.1 dex) seem to be present between isotopologue abundances retrieved using the narrow and wide wavelength ranges, with the latter resulting in lower $\log_{10}$ (VMR) values for a given filtering treatment (see Figure 3.2, first column). These effects likely arise from the additional sources

of TiO opacity contained on the wider spectral range. For instance, in addition to the red-degraded $\gamma(0,0)$ band starting at 7054 Å, the wide-spectrum retrievals also contain the two other strong red-degraded bands of the TiO $\gamma(0,0)$ triplet with band heads at 7089 Å and 7126 Å, as well as additional weak lines further redward. Simultaneously probing more features of varying strengths arising from different locations in the atmosphere could well lead to different retrieved abundances. Similarly small variations in abundance are also seen between retrievals using the unfiltered and broadband-filtered spectra. For a given wavelength range, fitting the broadband-filtered data generally leads to higher $\log_{10}$ (VMR) values. These differences can be attributed to the loss of continuum information, but are only $\sim$0.01 dex for the wide spectral range, except for the main isotopologue ($\sim$0.1 dex). Thus, the loss of continuum information hardly affects the retrieval of isotopologue abundances.

The remaining columns of Figure 3.2, comparing the derived Ti isotope ratios relative to Ti, ^{48}Ti, and ^{46}Ti, show there is generally good agreement between different retrievals, particularly for those ratios relative to ^{46}Ti. In Table 3.2, we provide the formal deviation between parameters retrieved using the different methodologies, calculated based on the errors derived from the MCMC posteriors. We note that despite our inclusion of the β parameter in the log-likelihood function (see Section 3.4), these formal deviation values are likely conservative error estimates and do not fully account for various sources of systematic uncertainty, for instance, in the choice of the T–P profile, line list inaccuracies, or the spectral modeling technique. Across all four retrieval methods, the isotope ratios relative to ^{46}Ti deviate by $<3\sigma$ for the minor isotopes and $<4\sigma$ for ^{48}Ti. This greater deviation for ^{48}Ti/^{46}Ti may be due to saturation of the strongest ^{48}TiO lines, as noted in previous studies (Clegg et al. 1979; Chavez & Lambert 2009; Pavlenko et al. 2020). The absolute spread in isotope ratios relative to Ti and ^{48}Ti across the various retrieval setups is only $\sim$1%. This small variation is immediately evident in Figure 3.5, where we plotted the absolute and relative abundances derived using the different methodologies (denoted by different markers), and found rather close clustering of values for each Ti isotope (denoted by different colors). This demonstrates that, similar to the retrieved isotopologue abundances, the isotope ratios relative to Ti and ^{48}Ti do not deviate much in absolute terms due to loss of continuum information or choice of wavelength range. This is particularly important considering that the S/N of exoplanet spectra will always be significantly lower than the stellar spectrum used here, resulting in much larger random errors (see Section 3.6.3).

We also verified that our assumptions for the mean molecular weight μ and stellar parameters of the T–P profile do not substantially impact the Ti iso-

tope analysis. For both the narrow and broadband-filtered spectrum and the wide and broadband-filtered spectrum, we performed MCMC fittings with the following mono-substituted parameters: $\mu = \{1.9, 2.1\}$, $T_{\rm eff} = \{3000, 3200\}$ K, $\log g = +5.0$, $[{\rm M/H}] = \{+0.00, +0.50\}$, and $v_{\rm turb} = 1$ km s^{-1}. Varying μ has a negligible impact on the retrieved isotope ratios. Changing the stellar T–P parameters results in $<3\sigma$ deviations for all isotope ratios relative to ^{46}Ti and most isotope ratios relative to Ti and ^{48}Ti.

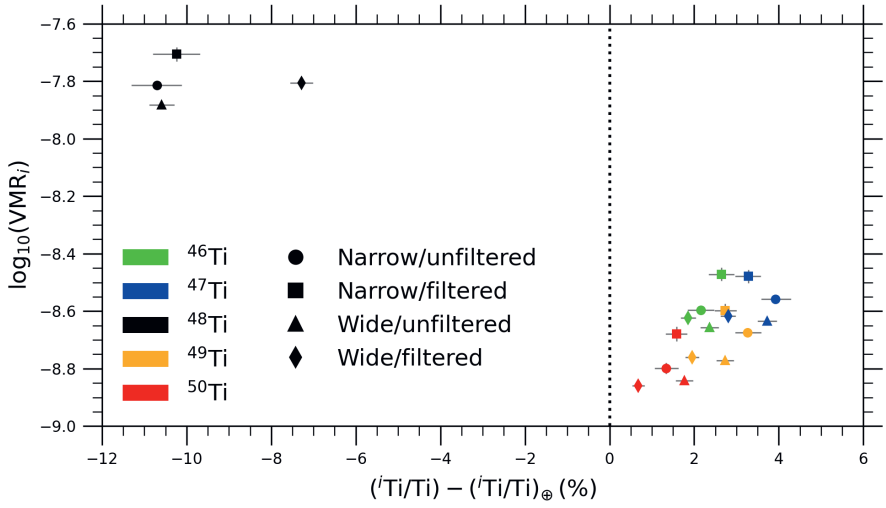

Figure 3.5. Comparison of absolute and relative abundances derived from each retrieval methodology, demonstrating the small impact the wavelength range and broadband filtering have on the results. For each stable titanium isotope ^{i}Ti, the retrieved $\log_{10}$ (VMR) of the corresponding isotopologue ^{i}TiO is shown on the y-axis, while the x-axis shows the absolute deviation in the relative abundance ^{i}Ti/Ti compared to the terrestrial value (vertical dotted line). The markers colored green, blue, black, orange, and red are used for ^{46}Ti, ^{47}Ti, ^{48}Ti, ^{49}Ti, and ^{50}Ti, respectively. The results for the narrow and unfiltered, narrow and filtered, wide and unfiltered, and wide and filtered spectra are denoted by the circular, square, triangular, and diamond markers, respectively. The 1σ errors, derived from the MCMC posteriors, are shown in gray.

3.6.2 GJ 1002 Ti isotope ratios in context

The relative abundances of Ti isotopes in GJ 1002 derived using the four different retrieval setups are all significantly different from the terrestrial values. While ^{48}Ti accounts for about 74% of all titanium atoms on Earth, we found this value to be only 63–66% in GJ 1002. The minor isotopes were all measured to be about 1–4% more abundant. We compared these values to those measured by Chavez & Lambert (2009) for a sample of 11 K- and M-dwarfs. They found a spread of about 11% in the relative abundance of ^{48}Ti, which is similar to the difference we found between GJ 1002 and Earth. With a literature metallicity of [M/H] = +0.20, the lower ^{48}Ti/Ti value we measured for GJ 1002 is consistent with expectations from various Galactic chemical models (e.g., Hughes et al. 2008; Chavez & Lambert 2009), which predict a negative correlation between the relative abundance of ^{48}Ti and metallicity. However, we note that in their stellar sample spanning metallicities $-1 <$ [Fe/H] < 0, Chavez & Lambert (2009) found essentially no correlation between metallicity and isotope ratios relative to ^{48}Ti, which are all similar to terrestrial.

As mentioned in Section 3.6.1, though, it is likely the strong ^{48}TiO lines we fit are saturated, so we are cautious to draw firm conclusions from the isotope ratios relative to Ti and ^{48}Ti. On the other hand, the abundances ratios of ^{47}Ti, ^{49}Ti, and ^{50}Ti relative to ^{46}Ti are not expected to be affected by saturation. The fourth column of Figure 3.2 indicates ^{50}Ti/^{46}Ti in GJ 1002 to be consistent with the terrestrial value, and the values for ^{47}Ti/^{46}Ti and ^{49}Ti/^{46}Ti to be consistent or marginally higher than Earth. These results are generally consistent with those from Chavez & Lambert (2009), who found approximately terrestrial values across their M-dwarf sample.

3.6.3 Determining Ti isotope ratios for gas-giant exoplanets

In Section 3.6.1, we show that the loss of continuum information common to exoplanet studies at high resolution should not be prohibitive in deriving Ti isotope ratios for gas-giant exoplanets. The other major difference between TiO analyses of M-dwarfs and future studies of exoplanets is the much fainter signals in the latter case. Figures 3.3 and 3.4 demonstrate that even for relatively low S/N levels, it is possible to constrain the relative abundances of Ti isotopes from the narrow and broadband-filtered spectrum and the wide and broadband-filtered spectrum, respectively. For each of the S/N levels shown, the $\log_{10}$(VMR) value of each isotopologue is consistent to within 3σ of the

non-degraded results, as are the Ti abundance ratios.

As expected, the fitting errors from the MCMC posteriors increase as the S/N decreases, and they are smaller for the wide, broadband-filtered spectrum compared to those for the narrow, broadband-filtered spectrum at a given S/N. To achieve $\lesssim$10% relative error for all Ti isotope ratios, the spectra in the range 7045–7050 Å must have S/N $\geq$ 10 for the narrow, broadband-filtered case and S/N $\geq$ 5 for the wide, broadband-filtered case.

To estimate the integration time required to achieve these S/N for various planetary systems using future high-contrast and high-dispersion instruments such as RISTRETTO (Chazelas et al. 2020) on the Very Large Telescope (VLT) and HIRES (Marconi et al. 2020) on the Extremely Large Telescope (ELT), we used a method similar to that described in Mollière & Snellen (2019). Assuming Poisson noise and negligible sky contribution, the planet emission S/N in a pixel centered at wavelength λ_0 is

$$(\mathrm{S/N})_{\mathrm{pix,planet}} = \frac{c_{\lambda_0}}{\sqrt{c_{\lambda_0} + 1/f}} \, (\mathrm{S/N})_{\mathrm{pix,star}} \,, \tag{3.2}$$

where $(\mathrm{S/N})_{\mathrm{pix,star}}$ is the stellar S/N in the pixel, c_{λ_0} is the planet-to-star luminosity contrast at wavelength λ_0, and f is the stellar-flux-reduction factor used to estimate the effect of suppressed stellar contribution in spatially resolved observations. Following Mollière & Snellen (2019), we adopted f values of 100 and 1000 for spatially resolved observations on the VLT and ELT, respectively, and $f = 1$ for spatially unresolved observations. We approximated c_{λ_0} as the ratio of blackbody luminosities at λ_0.

The stellar S/N is related to the integration time t by

$$(\mathrm{S/N})_{\mathrm{pix,star}} = \sqrt{N_{\mathrm{pix,star}}} = \sqrt{\frac{F^{\oplus}_{\lambda_0,\mathrm{star}} \; A \; t \; \Delta\lambda_{\mathrm{pix}} \; \tau}{E_{\lambda_0}}}, \tag{3.3}$$

where $N_{\mathrm{pix,star}}$ is the number of stellar photons collected by the pixel centered at λ_0, $F^{\oplus}_{\lambda_0,\mathrm{star}}$ is the stellar flux at wavelength λ_0 received at Earth, A is the telescope collecting area, $\Delta\lambda_{\mathrm{pix}}$ is the pixel width, τ is the telescope and instrument throughput, and E_{λ_0} is the photon energy at wavelength λ_0. Similar to Mollière & Snellen (2019), we took A to be 52 m^2 and 976 m^2 for the VLT and ELT, respectively, and adopted a throughput of 0.15. We approximated $F^{\oplus}_{\lambda_0,\mathrm{star}}$ using the blackbody luminosity at wavelength λ_0. For a given resolving power and number of pixels per resolution element n_{pix}, we can write $\Delta\lambda_{\mathrm{pix}} = \lambda_0/(\mathcal{R}\, n_{\mathrm{pix}})$. Following Mollière & Snellen (2019), we adopted $\mathcal{R} = 100,000$ and $n_{\mathrm{pix}} = 3$. By

replacing for $\Delta\lambda_{\rm pix}$, equating Equations (3.2) and (3.3), and rearranging, the required integration time for a given planet's S/N is

$$t = \left[(\mathrm{S/N})_{\rm pix,planet}\right]^2 \left(\frac{E_{\lambda_0}\ \mathcal{R}\ n_{\rm pix}}{F^{\oplus}_{\lambda_0,\rm star}\ A\ \tau\ \lambda_0}\right)\left(\frac{c_{\lambda_0}+1/f}{{c_{\lambda_0}}^2}\right). \tag{3.4}$$

Based on Equation (3.4), deriving Ti isotope ratios in unresolved ($f = 1$) observations of hot Jupiters is possible, but challenging. This is demonstrated by the case of the WASP-33 system, consisting of the transiting 1.7-$R_{\rm J}$ ultra-hot-Jupiter WASP-33b ($T_{\rm day} = 3100$ K) orbiting its 1.5-$R_\odot$ A5 host star ($T_{\rm eff} = 7430$ K) in a 1.2-d period (Collier Cameron et al. 2010; Kovács et al. 2013; Nugroho et al. 2021). WASP-33b is, thus far, the only hot Jupiter with evidence for TiO emission based on high-resolution spectral analyses (Nugroho et al. 2017; Serindag et al. 2021; Cont et al. 2021). At a distance of 117 pc (Kovács et al. 2013), to achieve S/N = 5 at 7045 Å on the ELT requires about seven hours of integration time assuming the planet dayside is fully visible, but nearly 29 hours of integration time assuming only half the planet dayside is visible.

Spatially resolved observations decrease the required integration time by reducing stellar contamination, though the planets suitable to such observations necessarily orbit much farther from their host stars than hot Jupiters. However, young wide-orbit planets are known to have $T_{\rm eff}$ similar to ultra-hot Jupiters. For example, the directly imaged 3.4-$R_{\rm J}$ planet GQ Lupi b has an effective temperature of 2400 K, despite orbiting its 1.7-$R_\odot$ T Tauri K7 host star ($T_{\rm eff} = 4300$ K) at ∼100 AU (Herbig 1977; Lavigne et al. 2009; Donati et al. 2012; Wu et al. 2017). At 150 pc (Crawford 2000), it would take less than one minute of integration time on the ELT to achieve a planet S/N of 5 at 7045 Å. Excitingly, the same S/N would also be attainable on the VLT in about an hour. Thus, there are excellent prospects to determine Ti isotope ratios in young gas-giant exoplanets on wide orbits.

3.7 Conclusions

We used *petitRADTRANS* models to fit TiO features in a CARMENES high-resolution spectrum of the M-dwarf GJ 1002, retrieving the relative abundances of Ti isotopes for a narrow and wide wavelength range, and for the unfiltered and broadband-filtered spectrum. The latter mimics typical high-resolution spectra of exoplanets for which continuum information is lost. Differences in the retrieved isotope ratios using the different setups are small. Most affected is the

main isotope ^{48}Ti due to possible saturation of the strongest ^{48}TiO lines. By degrading the S/N of the GJ 1002 spectrum and rerunning the retrievals, we determine a planetary S/N ≥ 5 is necessary to retrieve abundance ratios with relative errors $\lesssim$10% when fitting the wide wavelength range 7045–7500 Å. Future spatially resolved high-dispersion observations of widely-orbiting young gas giants can easily achieve such S/N, requiring only an hour and less than a minute of integration time on VLT/RISTRETTO and ELT/HIRES, respectively.

Acknowledgments

D.B.S., I.A.G.S., and P.M. acknowledge support from the European Research Council under the European Union's Horizon 2020 research and innovation program under grant agreement No. 694513. P.M. acknowledges support from the European Research Council under the European Union's Horizon 2020 research and innovation program under grant agreement No. 832428.

3.A Supplementary materials

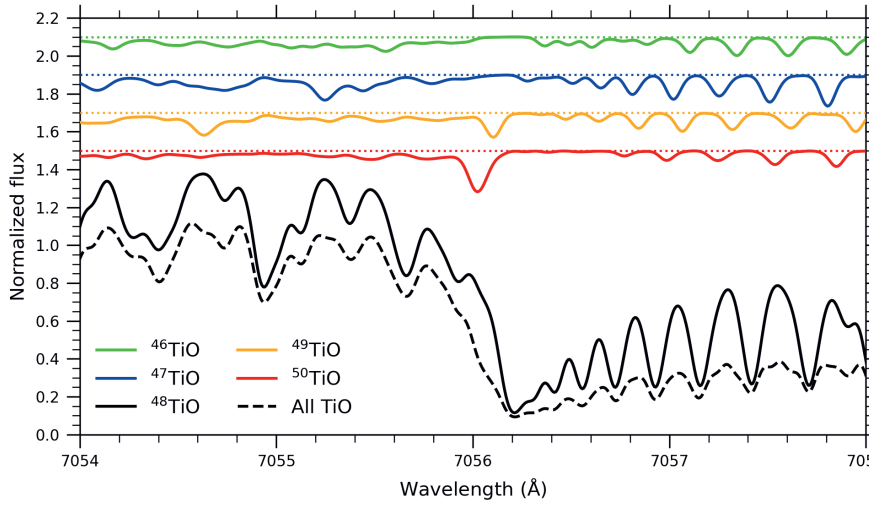

Figure 3.6. Flux contribution of each TiO isotopologue (solid lines) to the full TiO spectral model containing all isotopologues (dashed black line) around the strong band head at 7056 Å (7054 Å in air). Abundances were set at the retrieved values presented in Table 3.1 for the narrow and unfiltered GJ 1002 spectrum. The flux contribution of a given minor isotopologue ^{i}TiO was calculated as the difference between the model of all TiO isotopologues and the model of all isotopologues except ^{i}TiO. Since ^{48}TiO comprises 63% of TiO molecules in this setup, its flux contribution (solid black line) was calculated individually, without the presence of the minor isotopologues. Each contribution was normalized based on the full model's flux to ensure consistent scaling. The minor isotopologue contributions were vertically shifted to aid readability, with the offsets indicated by the dotted lines.

Table 3.1. Mean parameter values and 1σ errors from MCMC retrievals using different wavelength ranges and broadband filtering

Parameter	Value	Parameter	Value	Parameter	Value	Parameter	Value
Narrow/unfiltered spectrum							
$\log_{10}(\mathrm{VMR}_{46})$	-8.60 ± 0.01	$^{46}\mathrm{Ti}/\mathrm{Ti}$	0.104 ± 0.003	$^{46}\mathrm{Ti}/^{48}\mathrm{Ti}$	0.165 ± 0.006	–	
$\log_{10}(\mathrm{VMR}_{47})$	-8.56 ± 0.01	$^{47}\mathrm{Ti}/\mathrm{Ti}$	$0.114^{+0.004}_{-0.003}$	$^{47}\mathrm{Ti}/^{48}\mathrm{Ti}$	$0.180^{+0.007}_{-0.006}$	$^{47}\mathrm{Ti}/^{46}\mathrm{Ti}$	1.09 ± 0.05
$\log_{10}(\mathrm{VMR}_{48})$	-7.81 ± 0.01	$^{48}\mathrm{Ti}/\mathrm{Ti}$	0.630 ± 0.006	–		$^{48}\mathrm{Ti}/^{46}\mathrm{Ti}$	6.1 ± 0.2
$\log_{10}(\mathrm{VMR}_{49})$	-8.67 ± 0.02	$^{49}\mathrm{Ti}/\mathrm{Ti}$	0.087 ± 0.003	$^{49}\mathrm{Ti}/^{48}\mathrm{Ti}$	0.138 ± 0.006	$^{49}\mathrm{Ti}/^{46}\mathrm{Ti}$	0.83 ± 0.04
$\log_{10}(\mathrm{VMR}_{50})$	-8.80 ± 0.02	$^{50}\mathrm{Ti}/\mathrm{Ti}$	0.065 ± 0.003	$^{50}\mathrm{Ti}/^{48}\mathrm{Ti}$	0.103 ± 0.005	$^{50}\mathrm{Ti}/^{46}\mathrm{Ti}$	$0.63^{+0.04}_{-0.03}$
β	$4.94^{+0.07}_{-0.06}$	–		–		–	
Narrow/filtered spectrum							
$\log_{10}(\mathrm{VMR}_{46})$	-8.47 ± 0.02	$^{46}\mathrm{Ti}/\mathrm{Ti}$	0.109 ± 0.003	$^{46}\mathrm{Ti}/^{48}\mathrm{Ti}$	0.172 ± 0.006	–	
$\log_{10}(\mathrm{VMR}_{47})$	-8.48 ± 0.02	$^{47}\mathrm{Ti}/\mathrm{Ti}$	0.107 ± 0.003	$^{47}\mathrm{Ti}/^{48}\mathrm{Ti}$	0.169 ± 0.006	$^{47}\mathrm{Ti}/^{46}\mathrm{Ti}$	0.98 ± 0.03
$\log_{10}(\mathrm{VMR}_{48})$	$-7.71^{+0.02}_{-0.03}$	$^{48}\mathrm{Ti}/\mathrm{Ti}$	0.635 ± 0.006	–		$^{48}\mathrm{Ti}/^{46}\mathrm{Ti}$	5.8 ± 0.2
$\log_{10}(\mathrm{VMR}_{49})$	-8.60 ± 0.02	$^{49}\mathrm{Ti}/\mathrm{Ti}$	0.081 ± 0.003	$^{49}\mathrm{Ti}/^{48}\mathrm{Ti}$	$0.128^{+0.005}_{-0.004}$	$^{49}\mathrm{Ti}/^{46}\mathrm{Ti}$	0.75 ± 0.03
$\log_{10}(\mathrm{VMR}_{50})$	$-8.68^{+0.02}_{-0.03}$	$^{50}\mathrm{Ti}/\mathrm{Ti}$	$0.068^{+0.002}_{-0.003}$	$^{50}\mathrm{Ti}/^{48}\mathrm{Ti}$	$0.107^{+0.004}_{-0.005}$	$^{50}\mathrm{Ti}/^{46}\mathrm{Ti}$	0.62 ± 0.03
β	3.87 ± 0.05	–		–		–	
Wide/unfiltered spectrum							
$\log_{10}(\mathrm{VMR}_{46})$	-8.657 ± 0.009	$^{46}\mathrm{Ti}/\mathrm{Ti}$	0.106 ± 0.002	$^{46}\mathrm{Ti}/^{48}\mathrm{Ti}$	0.168 ± 0.004	–	
$\log_{10}(\mathrm{VMR}_{47})$	-8.635 ± 0.009	$^{47}\mathrm{Ti}/\mathrm{Ti}$	0.112 ± 0.002	$^{47}\mathrm{Ti}/^{48}\mathrm{Ti}$	0.177 ± 0.004	$^{47}\mathrm{Ti}/^{46}\mathrm{Ti}$	1.05 ± 0.03
$\log_{10}(\mathrm{VMR}_{48})$	-7.883 ± 0.004	$^{48}\mathrm{Ti}/\mathrm{Ti}$	0.631 ± 0.003	–		$^{48}\mathrm{Ti}/^{46}\mathrm{Ti}$	5.9 ± 0.1
$\log_{10}(\mathrm{VMR}_{49})$	-8.77 ± 0.01	$^{49}\mathrm{Ti}/\mathrm{Ti}$	0.081 ± 0.002	$^{49}\mathrm{Ti}/^{48}\mathrm{Ti}$	0.129 ± 0.004	$^{49}\mathrm{Ti}/^{46}\mathrm{Ti}$	0.77 ± 0.03
$\log_{10}(\mathrm{VMR}_{50})$	-8.84 ± 0.01	$^{50}\mathrm{Ti}/\mathrm{Ti}$	0.069 ± 0.002	$^{50}\mathrm{Ti}/^{48}\mathrm{Ti}$	$0.110^{+0.004}_{-0.003}$	$^{50}\mathrm{Ti}/^{46}\mathrm{Ti}$	0.66 ± 0.03
β	7.18 ± 0.03	–		–		–	

Parameter	Value	Parameter	Value	Parameter	Value	Parameter	Value
Wide/filtered spectrum							
$\log_{10}(\mathrm{VMR}_{46})$	$-8.623^{+0.01}_{-0.010}$	$^{46}\mathrm{Ti/Ti}$	0.101 ± 0.002	$^{46}\mathrm{Ti}/^{48}\mathrm{Ti}$	0.152 ± 0.003	–	
$\log_{10}(\mathrm{VMR}_{47})$	$-8.617^{+0.009}_{-0.010}$	$^{47}\mathrm{Ti/Ti}$	0.102 ± 0.002	$^{47}\mathrm{Ti}/^{48}\mathrm{Ti}$	0.154 ± 0.003	$^{47}\mathrm{Ti}/^{46}\mathrm{Ti}$	1.01 ± 0.03
$\log_{10}(\mathrm{VMR}_{48})$	$-7.805^{+0.007}_{-0.006}$	$^{48}\mathrm{Ti/Ti}$	0.664 ± 0.003	–		$^{48}\mathrm{Ti}/^{46}\mathrm{Ti}$	6.6 ± 0.1
$\log_{10}(\mathrm{VMR}_{49})$	-8.76 ± 0.01	$^{49}\mathrm{Ti/Ti}$	0.074 ± 0.002	$^{49}\mathrm{Ti}/^{48}\mathrm{Ti}$	0.111 ± 0.003	$^{49}\mathrm{Ti}/^{46}\mathrm{Ti}$	0.73 ± 0.02
$\log_{10}(\mathrm{VMR}_{50})$	-8.86 ± 0.01	$^{50}\mathrm{Ti/Ti}$	0.059 ± 0.001	$^{50}\mathrm{Ti}/^{48}\mathrm{Ti}$	0.088 ± 0.002	$^{50}\mathrm{Ti}/^{46}\mathrm{Ti}$	0.58 ± 0.02
β	$4.81^{+0.02}_{-0.03}$	–		–		–	

Table 3.2. Formal deviation between parameters retrieved using different wavelength ranges and broadband filtering

Parameter	Deviation (σ)	Param.	Dev. (σ)	Param.	Dev. (σ)	Param.	Dev. (σ)
Narrow/unfiltered vs. narrow/filtered							
$\log_{10}(\mathrm{VMR}_{46})$	4.75	^{46}Ti/Ti	1.11	^{46}Ti/^{48}Ti	0.79	–	
$\log_{10}(\mathrm{VMR}_{47})$	2.95	^{47}Ti/Ti	1.44	^{47}Ti/^{48}Ti	1.34	^{47}Ti/^{46}Ti	1.88
$\log_{10}(\mathrm{VMR}_{48})$	3.86	^{48}Ti/Ti	0.58	–		^{48}Ti/^{46}Ti	0.79
$\log_{10}(\mathrm{VMR}_{49})$	2.64	^{49}Ti/Ti	1.31	^{49}Ti/^{48}Ti	1.28	^{49}Ti/^{46}Ti	1.66
$\log_{10}(\mathrm{VMR}_{50})$	3.71	^{50}Ti/Ti	0.64	^{50}Ti/^{48}Ti	0.46	^{50}Ti/^{46}Ti	0.14
Wide/unfiltered vs. wide/filtered							
$\log_{10}(\mathrm{VMR}_{46})$	2.59	^{46}Ti/Ti	1.81	^{46}Ti/^{48}Ti	3.32	–	
$\log_{10}(\mathrm{VMR}_{47})$	1.39	^{47}Ti/Ti	3.25	^{47}Ti/^{48}Ti	4.63	^{47}Ti/^{46}Ti	0.93
$\log_{10}(\mathrm{VMR}_{48})$	10.31	^{48}Ti/Ti	8.11	–		^{48}Ti/^{46}Ti	3.35
$\log_{10}(\mathrm{VMR}_{49})$	0.75	^{49}Ti/Ti	2.96	^{49}Ti/^{48}Ti	4.01	^{49}Ti/^{46}Ti	1.14
$\log_{10}(\mathrm{VMR}_{50})$	1.05	^{50}Ti/Ti	4.38	^{50}Ti/^{48}Ti	5.32	^{50}Ti/^{46}Ti	2.38
Narrow/unfiltered vs. wide/unfiltered							
$\log_{10}(\mathrm{VMR}_{46})$	3.83	^{46}Ti/Ti	0.54	^{46}Ti/^{48}Ti	0.43	–	
$\log_{10}(\mathrm{VMR}_{47})$	4.87	^{47}Ti/Ti	0.49	^{47}Ti/^{48}Ti	0.46	^{47}Ti/^{46}Ti	0.70
$\log_{10}(\mathrm{VMR}_{48})$	5.89	^{48}Ti/Ti	0.18	–		^{48}Ti/^{46}Ti	0.43
$\log_{10}(\mathrm{VMR}_{49})$	5.10	^{49}Ti/Ti	1.46	^{49}Ti/^{48}Ti	1.32	^{49}Ti/^{46}Ti	1.38
$\log_{10}(\mathrm{VMR}_{50})$	1.89	^{50}Ti/Ti	1.21	^{50}Ti/^{48}Ti	1.09	^{50}Ti/^{46}Ti	0.64
Narrow/filtered vs. wide/filtered							
$\log_{10}(\mathrm{VMR}_{46})$	6.20	^{46}Ti/Ti	2.24	^{46}Ti/^{48}Ti	3.03	–	
$\log_{10}(\mathrm{VMR}_{47})$	5.70	^{47}Ti/Ti	1.34	^{47}Ti/^{48}Ti	2.28	^{47}Ti/^{46}Ti	0.68
$\log_{10}(\mathrm{VMR}_{48})$	3.79	^{48}Ti/Ti	4.79	–		^{48}Ti/^{46}Ti	3.15
$\log_{10}(\mathrm{VMR}_{49})$	6.07	^{49}Ti/Ti	2.62	^{49}Ti/^{48}Ti	3.40	^{49}Ti/^{46}Ti	0.49
$\log_{10}(\mathrm{VMR}_{50})$	6.34	^{50}Ti/Ti	3.06	^{50}Ti/^{48}Ti	3.61	^{50}Ti/^{46}Ti	1.21

Parameter	Deviation (σ)	Param.	Dev. (σ)	Param.	Dev. (σ)	Param.	Dev. (σ)
Narrow/unfiltered vs. wide/filtered							
$\log_{10}(\mathrm{VMR}_{46})$	1.63	^{46}Ti/Ti	0.82	^{46}Ti/^{48}Ti	1.98	–	
$\log_{10}(\mathrm{VMR}_{47})$	3.72	^{47}Ti/Ti	3.00	^{47}Ti/^{48}Ti	3.74	^{47}Ti/^{46}Ti	1.47
$\log_{10}(\mathrm{VMR}_{48})$	0.62	^{48}Ti/Ti	5.29	–		^{48}Ti/^{46}Ti	2.02
$\log_{10}(\mathrm{VMR}_{49})$	4.51	^{49}Ti/Ti	3.90	^{49}Ti/^{48}Ti	4.40	^{49}Ti/^{46}Ti	2.33
$\log_{10}(\mathrm{VMR}_{50})$	2.75	^{50}Ti/Ti	2.15	^{50}Ti/^{48}Ti	2.91	^{50}Ti/^{46}Ti	1.23
Narrow/filtered vs. wide/unfiltered							
$\log_{10}(\mathrm{VMR}_{46})$	7.74	^{46}Ti/Ti	0.76	^{46}Ti/^{48}Ti	0.51	–	
$\log_{10}(\mathrm{VMR}_{47})$	6.45	^{47}Ti/Ti	1.19	^{47}Ti/^{48}Ti	1.15	^{47}Ti/^{46}Ti	1.45
$\log_{10}(\mathrm{VMR}_{48})$	6.89	^{48}Ti/Ti	0.55	–		^{48}Ti/^{46}Ti	0.50
$\log_{10}(\mathrm{VMR}_{49})$	6.49	^{49}Ti/Ti	0.00	^{49}Ti/^{48}Ti	0.13	^{49}Ti/^{46}Ti	0.45
$\log_{10}(\mathrm{VMR}_{50})$	5.66	^{50}Ti/Ti	0.56	^{50}Ti/^{48}Ti	0.62	^{50}Ti/^{46}Ti	0.88

Chapter 4

A search for protoplanets around the young star HD 169142 using molecule mapping

Dilovan B. Serindag, Callum S. Griffiths, Ignas A. G. Snellen, and Rico Landman
To be submitted

Abstract

Context. Protoplanetary disks exhibit a range of substructures such as rings, gaps, and spirals. An important goal is to link these structures to the possible protoplanets that shape them. One such system is HD 169142, which shows two rings among which near-infrared high-contrast images have revealed several candidate protoplanets.

Aims. We searched for spectral signatures of these protoplanets in the HD 169142 system and, in particular, for the candidate object at an in-disk orbital distance of 38 AU. We aimed to confirm the presence of this planet, and to constrain the chemical composition of its atmosphere.

Methods. We used the molecule mapping technique on K-band integral field spectroscopic data ($\mathcal{R} \sim 5000$) taken with the SINFONI instrument on the Very Large Telescope, utilizing a grid of BT-Settl spectral models. The spectral contribution of the host star was removed from each spatial position, after which the residual spectra were cross-correlated with the models. Sensitivity limits were determined by injecting artificial planets using the same model grid.

Results. No spectral signatures were detected around HD 169142 at the locations of the candidate protoplanets. The injection and recovery analysis indicated that these observations are sensitive to a planet with mass $\gtrsim$7.3 $M_{\rm J}$ for a system age of 5–11 Myr at the location of the best candidate previously identified.

Conclusions. The observations presented here appear to be insufficiently sensitive to confirm or reject the main protoplanet candidate at 38 AU, which was suggested to have a mass $\lesssim$6 $M_{\rm J}$. Additional integral field spectroscopic observations will enhance the recoverability of any planet signal. However, since previous analysis suggested the planet is likely accreting, extinction by surrounding dust may complicate spectral analysis at medium resolution, and necessitate high-resolution studies. A similar scenario was suggested to explain the non-detection with molecule mapping of the protoplanets in the PDS 70 system. We estimate about 52 min of observing time is needed on ERIS, the upcoming high-dispersion successor to SINFONI, to reach the reported mass upper limit of the putative planet in HD 169142. The same result would require about 1 min of observing time on HARMONI, the planned optical/near-infrared integral field spectrograph for the Extremely Large Telescope.

4.1 Introduction

Many protoplanetary disks show substructures such as rings, gaps, and spirals that could indicate the presence of protoplanets (e.g., ALMA Partnership et al. 2015; Andrews et al. 2016; Andrews 2020, and the references therein). Finding and characterizing the responsible planets, as has been done for the PDS 70 system (e.g., Keppler et al. 2018; Haffert et al. 2019), constitutes an important step in better understanding planet formation. For instance, the chemical composition of their atmospheres is expected to trace the formation and early evolution of planets. Various factors, including formation location, migration, and gas versus solid accretion history are expected to affect bulk quantities such as relative elemental abundances and metallicity (e.g., Madhusudhan 2019, and the references therein). Planet formation theories incorporating these different factors provide predictions that can be tested by spectroscopic atmospheric observations (e.g., Line et al. 2021). Accessing and analyzing the atmospheric compositions of as complete a population as possible, across various orbital distances and planet ages, is thus critical to refining our understanding of the processes by which planets and their atmospheres form and evolve.

High contrast imaging enables the study of an exoplanet population largely inaccessible using other detection and characterization techniques. Whereas the transit and radial velocity methods for exoplanet analysis are inherently biased to close-in planets, spatially resolving exoplanets and their host stars is most feasible for relatively wide orbits ($\gtrsim$10 AU). At the moment, the number of imaged planets stands in the dozens, mainly because only very young planets that are still warm from their formation are bright enough to be detected. This is many fewer than the thousands provided by transit and radial velocity studies. Nonetheless, the ability to probe planets on wide orbits as well as young planets, possibly still undergoing formation, is invaluable.

Based on the cross-correlation technique pioneered by Snellen et al. (2010) to identify molecular signatures in high-resolution exoplanet spectra, Hoeijmakers et al. (2018b) developed "molecule mapping" for use with medium-resolution ($\mathcal{R} \sim 10^3$) integral field spectroscopy (IFS). First, the stellar spectral contribution is removed from each spatial location in the data set. By subsequently cross-correlating spectral templates of various molecules with the spectra at each spatial location, they measured the signatures of CO and H_2O in the atmosphere of the young (24 Myr; Bell et al. 2015) widely-orbiting (10 AU; Lacour et al. 2021) gas-giant planet β Pictoris b, and broadly constrained the planetary effective temperature and surface gravity by comparing the cross-correlation strengths retrieved for a grid of BT-Settl spectral models. Similar studies were

subsequently performed for other young directly-imaged planets, detecting CO and H_2O in both HR 8799 b (Petit dit de la Roche et al. 2018) and in HIP 65426 b (Petrus et al. 2021).

The HD 169142 system is estimated to be 5–11 Myr old, and consists of a gas-rich disk surrounding a 1.65–2 $M_\odot$ Herbig Ae/Be star (Gratton et al. 2019, and the references therein). VLA (Osorio et al. 2014), ALMA (Fedele et al. 2017), and near-infrared polarimetric observations (Quanz et al. 2013; Monnier et al. 2017; Pohl et al. 2017; Bertrang et al. 2018) all revealed two rings spanning approximately 0.″17–0.″28 (ring 1) and 0.″48–0.″64 (ring 2)[1]. Some studies proposed that disk structures such as the annular gap between rings 1 and 2 and a radial gap in ring 1 may imply the presence of planets in HD 169142 (Fedele et al. 2017; Bertrang et al. 2018). Other near-infrared observations (Biller et al. 2014; Reggiani et al. 2014) reported possible point-sources within 0.″2, but subsequent observations spanning multiple years by Ligi et al. (2018) and Gratton et al. (2019) could not confirm the existence of these features.

Gratton et al. (2019) expanded the near-infrared data set first presented by Ligi et al. (2018), and searched for persistent flux excesses in low-resolution ($\mathcal{R} \sim$ 30–50) IFS data in the Y-J (0.95–1.35 μm) and Y-H (0.95–1.65 μm) bands taken with the SPHERE instrument on the Very Large Telescope (VLT). In these data with epochs spanning three years, Gratton et al. (2019) found four persistent, extended flux sources that orbit the star with roughly Keplerian velocities: blob A at 13.5 AU, located in between the star and ring 1; blobs B and C within ring 1, at 21.4 AU and 23.1 AU, respectively; and blob D at 36.4 AU, within the annular gap between rings 1 and 2. Combining simultaneous observations with IRDIS on VLT/SPHERE in the $K1$ (2.09 μm) and $K2$ (2.25 μm) bands, Gratton et al. (2019) suggested that the relatively flat, reddish blob-to-star spectral contrasts are indicative of extincted, dust-scattered stellar light. They also found evidence for spiral arm structures within ring 1. Taken together, Gratton et al. (2019) proposed that the Y-J-H-band detection of blob D is starlight reflecting off an accretion flow associated with a nearby planet. They noted that the $K2$-band detection of blob D is spatially offset compared to its location in the Y-J-H band, which may indicate that the longer wavelength observations probed the planet's photosphere. In such a scenario, the putative planet would be responsible for carving the gap between rings 1 and 2, as well as exciting the spiral arms within ring 1. Using various metrics (photometry, inferred Hill radius, spiral arm separation, spiral arm pitch angle, disk gap size), they constrained the mass of this putative planet at 38 AU to $\lesssim$6 M_J, with a

[1]We adopt the ring nomenclature and spatial extents from Gratton et al. (2019).

best estimate of 2.2 $M_{\rm J}$.

In this chapter, we searched for spectral signatures at and around the location of blob D in medium-resolution IFS data taken using SINFONI on the VLT utilizing the molecule mapping technique. We cross-correlated exoplanet spectral templates with the spectra at each spatial location in our IFS observations. We also performed a sensitivity analysis of our data by injecting and recovering synthetic planet signals at the same on-sky orbital separation expected for blob D. In Section 4.2 we present our SINFONI data of HD 169142, and outline the processing techniques we applied to mitigate stellar and telluric contamination. We outline our methodology for searching for planet signals and performing the sensitivity analysis in Sections 4.3 and 4.4, respectively, and present the associated results in Section 4.5. We discuss these results and conclude in Section 4.6.

4.2 Integral field spectroscopic data of HD 169142

4.2.1 Data acquisition and characteristics

We observed[2] HD 169142 with the SINFONI integral field spectrograph (Eisenhauer et al. 2003; Bonnet et al. 2004) mounted on the Cassegrain focus of the Very Large Telescope UT4. Thirty-two observations were taken on 17 August 2018 and 16 observations on 18 August 2018, each consisting of 15 exposures of 4 s. The K-band grating was selected to provide a wavelength coverage of 1.93–2.47 μm at a resolving power of $\mathcal{R} \sim 5000$ (60 km s^{-1}) with a pixel sampling of 2.45×10^{-4} μm.

The spectrograph pre-optics were set for a field of view (FOV) of $0\farcs8 \times 0\farcs8$, with an orientation fixed at a position angle of 0° such that North and East point up ($+y$ direction) and left ($-x$ direction), respectively. In this setup, the SINFONI image slicer cuts along the East-West axis, producing 32 slices with a height of 25 mas. Each slice is then spatially sampled along the East-West axis by 64 pixels of size 12.5 mas. The spatial resolution is therefore 25 mas × 12.5 mas in declination and right ascension, respectively.

[2]ESO program ID: 0101.C-0582(A); PI: Snellen

4.2.2 Data reduction

We used the EsoRex pipeline (Freudling et al. 2013) to perform the initial data reduction on the bias-corrected SINFONI observations of HD 169142, including bad pixel masking, dark frame corrections, flat fielding, distortion corrections, and wavelength calibration. From each observation's raw data, the pipeline constructed a data cube of 2216 × 64 × 64 voxels[3] in λ, y, and x, respectively. Note the y-axis (declination) has been over-sampled by a factor of two.

The edges of the spectral axis contain bad frames as well as frames that are heavily contaminated by telluric features, so we retained only those frames with wavelengths 2.08–2.45 μm. To regain the native spatial resolution of 25 mas along the y-axis, we averaged adjacent pairs of rows in each wavelength frame. The spatial edges of each frame also contain rows and columns of bad spaxels[4]. We therefore removed the two top- and bottom-most rows and the four left- and right-most columns from each wavelength frame.

In each observation, the stellar photocenter is spatially offset from the center of the FOV by varying amounts. To spatially recenter each cube, we first generated a white-light image based on the median along the spectral axis. We then determined the spatial location of the stellar photocenter by fitting a two-dimension Gaussian to the 231 pixels surrounding the flux peak in the white-light image. Based on this spatial location, we linearly interpolated each frame in the given cube such that the spatial center corresponds to the fitted stellar photocenter. In the re-gridding, we preserved the 25 mas × 12.5 mas spatial resolution.

To verify the quality of the wavelength calibration for each cube, we cross-correlated the central 231 spaxels with a vacuum-wavelength ESO SkyCalc model (Noll et al. 2012; Jones et al. 2013) of the Earth's transmission spectrum, and determined the velocity offsets corresponding to the maximum cross-correlation values. The wavelength drift of each cube was calculated as the median velocity offset over these central spaxels. Over all observations, there is a $\approx$31 km s^{-1} redshift compared to the vacuum rest frame. To correct these offsets, we used a cubic spline to Doppler shift the spaxels in a given cube to the vacuum rest frame. The top left panel of Figure 4.1 shows the white light image of HD 169142 after this rest frame correction, calculated by median-combining the cubes of the individual observations and then taking the median flux along the wavelength axis.

[3]Data cube elements
[4]Spectrum for a given spatial position

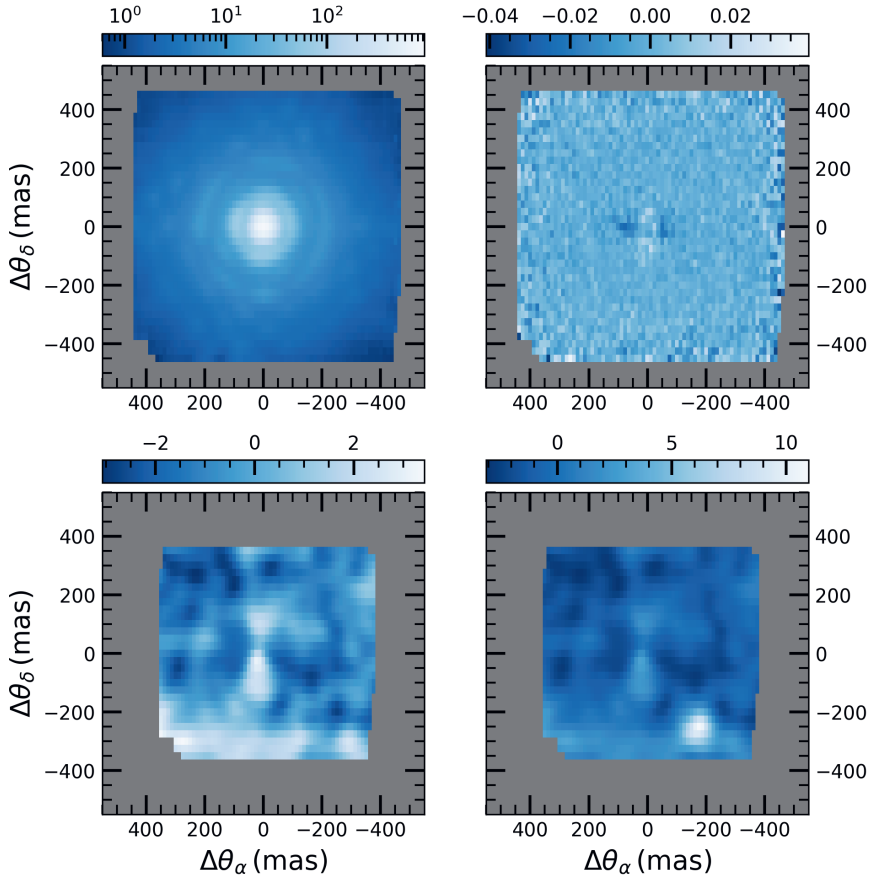

Figure 4.1. *Top left panel*: white light image of HD 169142 generated from the master cube of rest-frame-corrected observations. The colorbar flux units are arbitrary. *Top right panel*: white light image generated from the master cube of all observations after the removal of ten PCA components. The colorbar flux units are arbitrary. *Bottom left panel*: S/N image at $v = 0$ km s^{-1} for the cross-correlation of the $T_{\rm eff} = 1800$ K, $\log g = 4.0$ BT-Settl model with the PCA10 master cube. *Bottom right panel*: S/N image at $v = 0$ km s^{-1} for the cross-correlation of the $T_{\rm eff} = 1800$ K, $\log g = 4.0$ BT-Settl model with the PCA10 master cube, injected with a 1.6-$R_{\rm J}$ planet at $(\Delta\theta_\alpha, \Delta\theta_\delta) = (-179, -260)$ mas.

4.2.3 Removal of stellar and telluric contamination

To facilitate the retrieval of planetary spectral signals, further processing steps are necessary to remove the contributions of the host star and the Earth's atmosphere. Here, we loosely followed the recipe for molecule mapping presented in Hoeijmakers et al. (2018b). We first constructed a reference stellar spectrum for each cube by individually normalizing the central 45 spaxels by their total flux counts before taking the median in each wavelength bin. In calculating the median, we excluded values more than six standard deviations from the bin median. This reference spectrum serves as a template for the contributions from the stellar point-spread-function (PSF) and telluric absorption.

We divided the spaxels in each cube by that cube's reference stellar spectrum to determine the relative spectral contribution as a function of wavelength at each spatial position. To isolate low-frequency deviations (e.g., from quasi-static speckles) while preserving any potential high-frequency planetary signal, we performed a low-pass Gaussian filter with a FWHM of 20 pixels ($\approx 5\times10^{-3}$ μm) on the relative spectral contribution at each spaxel. We then subtracted from each spaxel the reference stellar spectrum scaled by that spaxel's low-frequency relative spectral contribution. The resulting flux residuals for each spaxel should subsequently be largely devoid of low-frequency spectrally- and spatially-dependent contributions of the stellar PSF and telluric absorption.

To attempt to clean any remaining stellar and telluric noise, we performed a 6σ clipping of each spaxel, masked any outliers, and, for regions that are well sampled, subsequently replaced their value by the mean value of the adjacent ten voxels in the spectrum. We then projected each cube onto a two-dimensional matrix where each column is a different spaxel. On these matrices we performed a principle component analysis (PCA) using the singular value decomposition technique (e.g., de Kok et al. 2013). Removing increasing numbers of principle components from the matrix decreases the correlated noise. For each cube, we performed the PCA iteratively to generate ten new cubes, each with an additional principle component removed.

4.2.4 Combining observations

To maximize any potential planet signal in our set of SINFONI observations, we stacked the residual flux cubes for all 48 observations. The stacking was performed by taking the median for each voxel across the set of observations. The residual flux cubes were stacked for each PCA iteration separately, resulting in 11 master cubes for PCA iterations 0–10. As an example, the top right panel

of Figure 4.1 shows the white light image generated from the master cube for the PCA10 case.

4.3 Search for planet signals

We searched for planetary spectral signatures in the SINFONI data by cross-correlating BT-Settl (CIFIST) models[5] (Allard et al. 2011, 2012, 2013) with each spaxel in the 11 residual flux cubes (Section 4.2.4) on velocities (v) spanning -2000 to $+2000$ km s^{-1} in steps of 10 km s^{-1}. The result is a set of 11 cross-correlation cubes in v, y, and x for each model. We restricted ourselves to solar metallicity models with $T_{\rm eff} = 1200$–4000 K and $\log g = 2.5$–5.5. To maximize the retrieval of any potential planet signal, prior to cross-correlation we broadened the BT-Settl models to $\mathcal{R} = 5000$ to match the SINFONI resolving power and performed a high-pass filtering to mimic our treatment of the data.

To further enhance the signal recoverability of possible planetary signals, we convolved each velocity frame in the cross-correlation cubes with a two-dimensional Gaussian. This accounts for the fact that any planet signal, like that of the star, should be spatially extended by the PSF of the imaging system. The widths of the convolution kernel along the x- and y-axes were determined by fitting a two-dimensional Gaussian to the stellar PSF in the rest-frame-corrected white light image of the star, shown in the top left panel of Figure 4.1 and described in Section 4.2.2. The Gaussian convolution kernel was truncated at three times the width along each axis.

To quantify the strength of correlation peaks relative to the surrounding noise, we divided the cross-correlation values in each spaxel by the standard deviation of the cross-correlation values in that spaxel with velocities $|v| > 500$ km s^{-1}, so as to avoid the contribution of any potential planet signal. We thereby converted the cross-correlation cubes to signal-to-noise ratio (S/N) cubes. The bottom left panel of Figure 4.1 shows an example image at $v = 0$ km s^{-1} from the S/N cube generated from the cross-correlation of the $T_{\rm eff} = 1800$ K, $\log g = 4.0$ BT-Settl model with the PCA10 master cube. While there is clearly no statistically-significant peak in this case, for comparison, the bottom right panel of Figure 4.1 shows how the S/N image would look with a 1.6-$R_{\rm J}$ planet added at $(\Delta\theta_\alpha, \Delta\theta_\delta) = (-179, -260)$ mas. The artificial signal in the bottom right corner of this panel is clearly visible.

[5]Retrieved from
http://svo2.cab.inta-csic.es/theory/newov2/index.php?models=bt-settl-cifist

4.4 Injection–recovery tests of synthetic planet signals

We also evaluated the recoverability of planetary signals in the SINFONI data by performing injection–recovery tests with synthetic planet signals. To simulate the planetary spectrum, we used the same BT-Settl models described in Section 4.3, broadened to $\mathcal{R} = 5000$ to match the resolving power of SINFONI. To ensure accurate flux levels for the synthetic planet signals, we generated a planet PSF by scaling the stellar PSF profile by the wavelength-dependent luminosity contrast between the simulated planet and the host star HD 169142. We determined the stellar PSF profile for each wavelength frame of each observation by fitting a two-dimensional Gaussian to the 861 voxels about the stellar photocenter. The luminosity contrast for a synthetic planet of radius R_p and effective temperature $T_\mathrm{eff,p}$ was calculated as the flux ratio of the BT-Settl model spectrum for $T_\mathrm{eff,p}$ to the blackbody spectrum for $T_\mathrm{eff,\star} = 7500$ K, scaled by $(R_\mathrm{p}/R_\star)^2$ with $R_\star = 1.59\ R_\odot$ (Blondel & Djie 2006). We adopted $\log g = 4.0$ for all synthetic planets.

To inject a synthetic planet signal into a given observation, we truncated the planet PSF beyond 3σ from the peak and added it to the corresponding rest-frame-corrected data cube. After performing this injection for each observation in our data set, we ran the injected data cubes through the same reduction procedure outlined in Sections 4.2.3 and 4.2.4 to remove stellar and telluric contamination. We recovered the injected signal by cross-correlating the master cubes with the broadened, filtered version of the BT-Settl model used to generate the synthetic planet signal, and then performing a two-dimensional Gaussian convolution as described in Section 4.3. Since we wanted to quantify the recoverability even in the weak signal cases, we calculated the S/N value for each voxel as the difference between the injected and uninjected cross-correlation values for that voxel, normalized by the standard deviation of the cross-correlation values for $|v| > 500$ km s^{-1} in the corresponding uninjected spaxel. We adopted the maximum value on the S/N cube within one voxel ($\Delta v = 10$ km s^{-1}, $\Delta y = 25$ mas, $\Delta x = 12.5$ mas) of the injection location as the recovered S/N.

4.5 Results

4.5.1 Non-detection of planet signal

We examined the S/N cubes described in Section 4.3 for statistically significant peaks near the expected radial velocity and spatial location of blob D. We set the velocity range rather wide at $|v| \leq 100$ km s^{-1}, which easily accommodates the contributions of the heliocentric motion of the VLT in the direction of HD 169142 (+22 km s^{-1}), the heliocentric radial velocity of the system (-3 ± 2 km s^{-1}; Dunkin et al. 1997a,b), and the expected orbital velocity of the planet along our line of sight (± 1 km s^{-1}). This latter value was calculated as the line-of-sight Keplerian velocity assuming a circular orbit, a system inclination of 13°, a stellar mass of 1.65 $M_\odot$ (Blondel & Djie 2006), and an in-disk orbital distance for blob D of 36.4 AU (Gratton et al. 2019). To determine the spatial position of blob D in our data, we deprojected the most recent on-sky position of blob D reported in Table 3 of Gratton et al. (2019) into the disk plane, advanced the orbital position to the epoch of our SINFONI observations using the in-disk orbital speed presented in Table 7 of the same work, and re-projected the updated position to the sky plane. We estimated the error in this updated position by performing the same procedure on a sample of 10^5 positions and orbital velocities drawn from normal distributions with spreads corresponding to the reported errors in Gratton et al. (2019), and taking the standard deviation of the resulting distribution. We defined the spatial bounds for our search as the spaxels containing x and y values within ± 6 standard deviations of the expected on-sky position of blob D. These velocity and spatial bounds also easily incorporate the slightly offset location of the putative planet. No peaks with S/N > 4 were found within these bounds in the S/N cubes for any of the BT-Settl models. Similar searches at the locations of blobs B and C did not reveal any peaks with S/N > 4 either, while the corresponding search at the location of blob A was inconclusive due to the presence of strong residual stellar contamination.

4.5.2 Injection–recovery tests

Using the injection–recovery procedure described in Section 4.4, we determined the sensitivity of our data and reduction method to recovering planet signals at the on-sky orbital distance of blob D (316 mas). We injected synthetic planet signals assuming various planet effective temperatures and radii to probe different planet–star luminosity contrasts. For each $T_{\rm eff,p}$–$R_{\rm p}$ combination, we

performed the injection–recovery procedure at $v = 0$ km s^{-1} and three spatial locations with a constant on-sky offset of 315.6 mas and position angles offset by 90°, 180°, and 270° from the expected 34.6°. We averaged the maximum recovered S/N for these three cases to determine a single recoverable S/N for each contrast. The spread in S/N values relative to the average value was always $\lesssim$30%. These average values are presented in Figure 4.2. Each panel shows the sensitivity of our SINFONI data and reduction procedure for different values of planet radius (y-axis) and effective temperature (x-axis). The color gradient indicates the average recovered S/N, with blue shades corresponding to S/N < 5 and red shades corresponding to S/N > 5. For typical planet radii of 1.6–1.8 $R_{\rm J}$, we are only sensitive to effective temperatures $\gtrsim$1600 K.

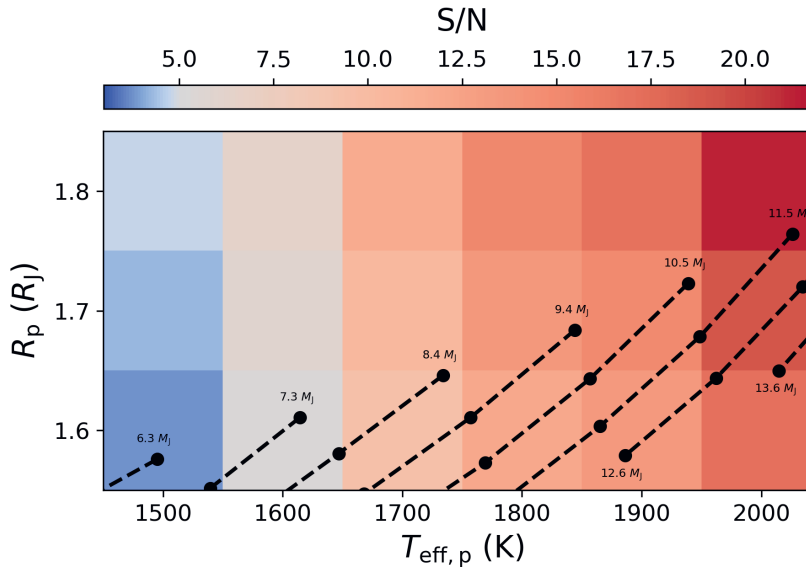

Figure 4.2. Recoverability of injected planet signals in our SINFONI data set at the on-sky distance of blob D. Each panel corresponds to a different effective temperature and radius, and the color coding indicates the recovered S/N value, averaged across the three injection locations. The color gradient breaks at S/N = 5, which we adopted as the threshold for a robust detection. The evolutionary tracks from Phillips et al. (2020) are plotted in black for various planet masses for the 5–11 Myr age of HD 169142.

4.6 Discussion and conclusions

Using the molecule mapping technique with BT-Settl spectral models, we were unable to confirm the presence of the putative planet in the SINFONI data at or near the persistent flux feature labeled blob D by Gratton et al. (2019), or indeed at any of the other blob locations reported therein. Despite allowing rather generous velocity and spatial bounds, no cross-correlation peaks with S/N > 4 were found near the expected location of the putative planet. In light of our sensitivity analysis in Section 4.5.2, this result is not necessarily unexpected.

To link the sensitivity of our data and methodology at the various $T_{\mathrm{eff,p}}$ and R_{p} plotted in Figure 4.2 to physically-realistic planet cases, we overplotted the model evolutionary tracks from Phillips et al. (2020) for low-mass objects in black. We only show those time steps (black circles) within the 5–11 Myr age range of HD 169142. Each curve corresponds to a different object mass, and demonstrates the cooling and contraction of planets in the immediate aftermath of formation. Based on the transition of the recovered S/N values from less than to greater than 5 around 1500–1600 K, we conclude that our analysis is sensitive to masses $\gtrsim$7.3 M_{J} near the location of blob D in the HD 169142 system. We are thus insensitive to the putative planet mass proposed in Gratton et al. (2019). They constrained the planet mass to $\lesssim$6 M_{J}, with a best estimate of 2.2 M_{J}.

Potentially further complicating the retrieval of planetary spectral signals is the scenario proposed by Gratton et al. (2019) that the persistent blob D found in their IFS observations is stellar light reflected off an accretion flow feeding the nearby putative planet. While we were unable to find evidence in our master cubes of Brackett γ emission indicative of accretion, such a scenario may suggest surrounding material that could obscure the spectral lines of the planet's photosphere, as seems to be the case for PDS 70 b. The PDS 70 system is young (5.4 Myr; Müller et al. 2018) and contains two widely-orbiting protoplanets PDS 70 b and PDS 70 c at 21 AU and 35 AU, respectively (Keppler et al. 2018; Müller et al. 2018; Haffert et al. 2019). Both planets have been shown to be actively accreting based on spatially-resolved detections of Hα emission (Wagner et al. 2018; Haffert et al. 2019). Subsequent analysis of PDS 70 b by Cugno et al. (2021) was unable to detect spectral signatures of H_2O, CO, or CH_4 in SINFONI data using similar reduction and cross-correlation techniques to our study. They suggested that dust extinction is the likely cause of the non-detection of molecular features at medium spectral resolution, one source of which may be a dusty shell enveloping the planet. As a remedy, they noted observations at higher spectral resolution should enable a greater line-to-

continuum contrast, and thereby enhance the detectability of extincted spectral signatures.

Probing the spectroscopic signature of the putative protoplanet near blob D in HD 169142 therefore requires additional observations, ideally at higher spectral resolution. Although the SINFONI instrument has been decommissioned, the upcoming VLT instrument ERIS will incorporate the refurbished SINFONI IFS, upgraded to enable high-dispersion ($\mathcal{R} = 8000$) observations. We can estimate how much more observing time on ERIS is required from the S/N value in Figure 4.2 for 1.6 $R_{\rm J}$ and 1500 K, which are very similar to the radius and $T_{\rm eff}$ values predicted by the Phillips et al. (2020) models for a 6.3 $M_{\rm J}$ planet. Based on the retrieved S/N value of 3.8 from the injection–recovery tests, achieving a S/N of 5 at this flux contrast with the higher ERIS resolving power would require 1.1× as much observing time, or about 52 min. In contrast, only about 1 min of observing time would be required to reach a S/N of 5 using the highest-dispersion setting ($\mathcal{R} = 18,000$) on HARMONI, the planned optical/near-infrared IFS for the Extremely Large Telescope. These estimates should be taken as lower limits on the observing time, as ∼6 $M_{\rm J}$ is the upper limit for the putative planet.

Acknowledgments

D.B.S., I.A.G.S., and R.L. acknowledge support from the European Research Council under the European Union's Horizon 2020 research and innovation program under grant agreement No. 694513. This research has made use of the Spanish Virtual Observatory (http://svo.cab.inta-csic.es) supported from Ministerio de Ciencia e Innovación through grant PID2020-112949GB-I00.

Chapter 5

Testing the detectability of extraterrestrial O_2 with the extremely large telescopes using real data with real noise

Dilovan B. Serindag and Ignas A. G. Snellen
Published in The Astrophysical Journal Letters, 871, L7 (2019)

Abstract

The future extremely large telescopes (ELTs) are expected to be powerful tools to probe the atmospheres of extrasolar planets using high-dispersion spectroscopy, with the potential to detect molecular oxygen in Earth-like planets transiting nearby late-type stars. So far, simulations have concentrated on the optical 7600 Å *A* band of oxygen using synthetic noise distributions. In this chapter, we build upon previous work to predict the detectability of molecular oxygen in nearby temperate planets by using archival time-series data of Proxima Centauri from the high-dispersion Ultraviolet and Visual Echelle Spectrograph (UVES) on ESO's Very Large Telescope (VLT). The brightest transiting M-dwarfs are expected to be about 25 times fainter than Proxima, a factor that is similar to the difference in light-gathering power between the VLT and the future ELTs. By injecting synthetic oxygen transmission signals into the UVES data, the O_2 detectability can be studied in the presence of real data with real noise properties. Correcting for the relatively low throughput ($\sim$4%) of the Proxima spectra to an assumed 20% throughput for a high-dispersion spectrograph on the European ELT, we find that the molecular oxygen signature of an Earth-twin transiting a nearby ($d \approx 7$ pc) M5V star can be detected in 20–50 transits (a total of 70–175 hr of observing time). This estimate, using more realistic simulations, is close to previous predictions. Novel concepts that increase the instrumental throughput can further reduce the time span over which such observations need to be taken.

5.1 Introduction

The search for biosignature gases in the atmospheres of terrestrial exoplanets will be an important component in the search for extraterrestrial life. Finding such compounds in thermodynamic disequilibrium and abundances inconsistent with abiotic processes will be suggestive of life (e.g., Lovelock 1965; Lippincott et al. 1967; Meadows 2017; Meadows et al. 2018). In particular, the simultaneous atmospheric detection of O_2 and a reducing gas, such as CH_4 or N_2O, has been suggested as a probe for biological activity (e.g., Lovelock 1975; Sagan et al. 1993; Segura et al. 2005) as such a combination is highly mutually reactive and would not persist without continuous resupply. One promising method to search for molecular oxygen is to probe the spectra of temperate terrestrial exoplanets transiting late-type M-dwarfs using the future extremely large telescopes (ELTs[1]) at high dispersion (Snellen et al. 2013; Rodler & López-Morales 2014; Ben-Ami et al. 2018).

Over the last decade, ground-based high-dispersion ($\mathcal{R} = \lambda/\Delta\lambda \sim 10^5$) spectroscopy has provided robust detections of several molecular (e.g., Snellen et al. 2010; Birkby et al. 2013; Nugroho et al. 2017) and atomic (e.g., Hoeijmakers et al. 2018a) species in giant exoplanet atmospheres. It uses cross-correlation of model templates with spectroscopic observations to probe the exoplanet's atmospheric composition. At these high spectral resolutions, molecular bands resolve into individual lines, whose signal contributions are co-added during cross-correlation. This technique is expected to be important in the ground-based detection of exoplanet biosignatures like oxygen because the resolved telluric and exoplanet lines can be separated using the radial velocity of the system, the barycentric motion of the Earth, and the radial velocity component of the orbital motion of the exoplanet. Particularly amenable to this technique is the A-band transition of O_2 at 7600 Å due to its spectral isolation and resolvability at high $\mathcal{R}$.

Snellen et al. (2013) and Rodler & López-Morales (2014) previously studied the feasibility of using ELT transmission spectroscopy to detect the O_2 A band in terrestrial exoplanet atmospheres. Snellen et al. (2013) compared the detection requirements for an Earth-twin transiting in the habitable zones of G-dwarfs (G0–G5), early-type M-dwarfs (M0–M2), and late-type M-dwarfs (M4–M6), and found that the relatively short, 12-day periods make temperate exoplanets transiting late-type M-dwarfs preferential targets. Simulating

[1]We adopt ELT as a generic abbreviation for the future giant segmented mirror telescopes, and use "European ELT" if we specifically mean the 39-m telescope being built by ESO.

European ELT (E-ELT) observations of an $I = 11.1$ mag[2] Earth–M5V system assuming only uncorrelated noise, they determined that a 3.8σ detection of the O_2 A band requires 30 transits. Rodler & López-Morales (2014) performed similar simulations for various spectrograph setups, with and without correlated noise. Adopting similar system parameters as Snellen et al. (2013), they determined for late-type M-dwarfs that 42–60 transits are needed for a 3σ detection of O_2 when only uncorrelated noise is considered, and 60–84 transits when both uncorrelated and correlated noise are simulated.

The studies described above are based on idealized simulations with synthetic data. In particular, real data from real telescopes of real stars, which may show significant astrophysical noise, could potentially degrade the expected performances and affect the feasibility of such observations. In this chapter, we test these feasibility predictions using real data. While high-dispersion E-ELT spectra of an $I = 11$ mag M5V star will of course not be available for several years, they should be very similar to data of an $I = 7.5$ mag dwarf from an 8-m-class telescope. The fact that the light-gathering power of such a telescope is a factor $\sim$25 smaller is compensated by the star being $\sim$25 times brighter. We use three nights of high-dispersion archival spectra from ESO's Very Large Telescope (VLT) of Proxima Centauri (M5.0V, $I = 7.41$ mag; Jao et al. 2014) and inject synthetic oxygen transmission spectra to assess the detectability of this biosignature gas in temperate terrestrial exoplanets. This multi-night spectral time series allows us to include the influence of the rich stellar spectra, the barycentric motion of the observatory, and all components of the Earth's atmosphere in our assessment of the recoverability of the exoplanet signal.

The archival data and initial reduction are presented in Section 5.2, and the simulation methodology in Section 5.3. The results are presented in Section 5.4 and discussed in Section 5.5.

[2] I-band magnitude expected for the brightest late-type M-dwarfs with a transiting, habitable-zone Earth-twin, assuming that all late-type M-dwarfs host such a planet (Snellen et al. 2013).

5.2 Archival data of Proxima Centauri

The data set consists of three nights[3] of archival observations of Proxima by the Ultraviolet and Visual Echelle Spectrograph (UVES; Dekker et al. 2000) mounted on UT2 of the VLT, taken 2009 March 10, 12, and 14. Each night of observation spans nearly eight hours, and consists of 215, 168, and 178 spectra, respectively, with typical exposure times of 100 s for March 10 and 14, and between 90 and 200 s for March 12. The UVES slit width was $1''$ with a reported resolving power $\mathcal{R} = 42,310$, corresponding to a spectral resolution of $\Delta\lambda = 0.18$ Å ($\Delta v = 7.1$ km s^{-1}) at 7600 Å, and a pixel sampling of 0.039 Å ($\Delta v = 1.5$ km s^{-1}). We inspected and removed spectral observations with poor signal-to-noise ratio (S/N), leaving 214, 162, and 175 observations for each night.

5.2.1 Initial data reduction

Initial reduction of the UVES data was performed by the UVES-Echelle pipeline,[4] which includes de-biasing, background subtraction, order extraction, flat-fielding, wavelength calibration, and order merging. Upon inspection, variations in the wavelength solution over the course of each night are clearly visible in the pipeline-reduced spectra. These wavelength shifts have magnitudes of up to several tenths of a pixel (see Figure 5.1), determined by cross-correlating the telluric-free region at 7500–7570 Å of each spectrum with that of the lowest-resolution observation of each night. Additionally, we found a temporal variation in spectral resolution.

We used the singular value decomposition (SVD) method presented in Rucinski (1999) to simultaneously correct the wavelength shifts and variations in spectral resolution. In brief, SVD inverts the expression $F(\lambda) = B(\lambda) * f(\lambda)$ to calculate the kernel B that broadens a narrow spectrum f to F. For each night of UVES observations, we selected the spectrum with the lowest resolution to serve as reference and used the SVD method to derive 11-pixel-wide kernels for the remaining spectra based on the telluric-free 7500–7570 Å wavelength range. Convolving the spectra with their corresponding kernels corrects the variation in resolution. As Figure 5.1 demonstrates, the non-symmetric nature of the kernels also corrects the wavelength shifts, which have magnitudes on the

[3]Based on observations collected at the European Southern Observatory under ESO program 082.D-0953(A). PI: Liefke.

[4]https://www.eso.org/observing/dfo/quality/UVES/pipeline/pipe_reduc.html
https://www.eso.org/observing/dfo/quality/UVES/pipeline/recipe_science.html

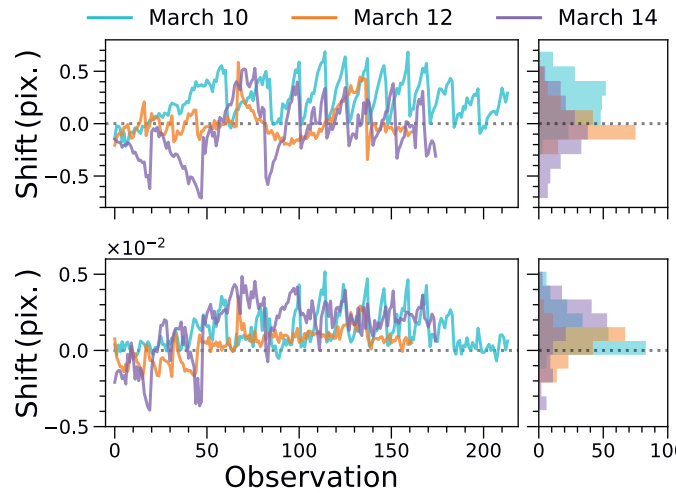

Figure 5.1. *Left panels*: shifts in the wavelength solution in pixels (0.039 Å, $\Delta v = 1.5$ km s^{-1}) for the March 10 (blue), 12 (orange), and 14 (purple) spectral time series relative to the lowest-resolution reference spectrum for each night. The top and bottom panels correspond to the measured shifts before and after the singular value decomposition (SVD) correction. Note the different vertical scales, showing that the shifts have decreased by two orders of magnitude. *Right panels*: corresponding histograms of wavelength shifts for each night.

order of thousandths of a pixel after convolution — a two order-of-magnitude improvement.

5.2.2 Assessment of data quality

Following the SVD correction, we calculated the S/N of the individual UVES spectra in the same telluric-free range by dividing $\sqrt{2}$ by the measured standard deviation of the ratio of two successive spectra. The average is taken of the S/N derived from both the preceding and subsequent spectra, resulting in

$$(\mathrm{S/N})_i = \frac{1}{\sqrt{2}} \left(\frac{1}{\mathrm{std}(f_i/f_{i-1})} + \frac{1}{\mathrm{std}(f_i/f_{i+1})} \right). \tag{5.1}$$

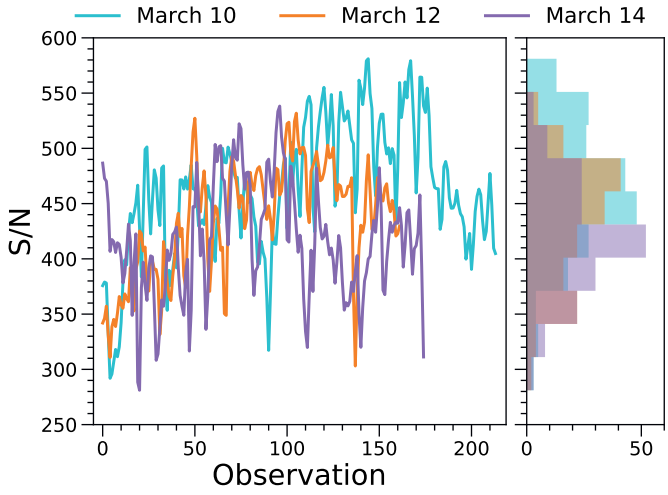

Figure 5.2. *Left panel*: S/N of each UVES spectrum. The observations are temporally sequenced and color-coded by date as in Figure 5.1. *Right panel*: histogram of S/N values for each observation date. The joint S/N distribution including all dates has a median value 443 ± 57.

Figure 5.2 shows the temporal evolution of the S/N over the course of each night, and the associated distributions. Overall, the spectra have a median S/N of 443 ± 57 in the telluric-free region. We also calculated the S/N for each UVES wavelength bin by dividing the bin's median flux value by its corresponding standard deviation. These S/N profiles are shown in Figure 5.3 for each observation night.

An important property of the archival observations is the total throughput of the telescope and instrument. Based on the I-band magnitude of Proxima, the collecting area of the VLT, and the integration times, we determined the incident photon count in the telluric-free range and compared this to the observed UVES photon count to find a throughput of 3.8%, a factor $\sim$2.5 lower than the new Echelle SPectrograph for Rocky Exoplanets and Stable Spectroscopic Observations (ESPRESSO; C. Lovis 2018, private communication), and $\sim$5 times lower than the throughput assumed by Snellen et al. (2013).

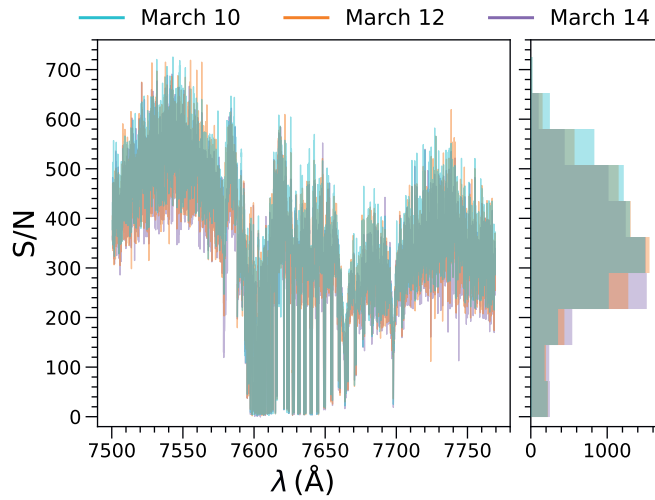

Figure 5.3. *Left panel*: S/N of each UVES wavelength bin, color-coded by observation date as in Figure 5.1. *Right panel*: histogram of S/N values for each observation date.

5.3 Synthetic oxygen transmission spectra

5.3.1 Transmission model calculation and injection

We determined the atmospheric transmission in the oxygen A band at a spectral resolving power of $\mathcal{R} = 100,000$, and the resulting change in effective radius as a function of wavelength, for an Earth-twin — a planet with Earth's surface gravity, and atmospheric composition and temperature structure (including a constant oxygen volume-mixing ratio of 20.95%). This was converted to a transmission spectrum of an Earth-twin transiting a late-type M-dwarf assuming an M5V star radius of 0.19 $R_\odot$. As the high-dispersion transit technique is only sensitive to the high-frequency part of the transmission spectrum, the broadband transmission signal is removed using a high-pass filter. Figure 5.4 shows the resulting, relative transit depth due to O_2, with individual line strengths of up to 4.5×10^{-5}. Refraction effects were not modeled as they negligibly impact the transmission spectrum of an Earth–M5V system (Bétrémieux & Kaltenegger 2014).

We simulate the observations of a full transit by injecting the model template (Figure 5.4) into a series of UVES observations, Doppler-shifted to mimic the orbital motion of the exoplanet about its system's barycenter. Assuming a circular orbit and an edge-on inclination, the transit duration for an Earth-twin orbiting an M5V star in the habitable zone is 1.4 hr for an orbital period $P = 11.8$ days, stellar mass $M_\star = 0.19\ M_\odot$, and stellar radius $R_\star = 0.19\ R_\odot$ (Snellen et al. 2013). Adopting a uniform cadence of 130 s (median observation cadence of the UVES data), each simulated transit consists of 39 successive UVES observations injected with an Earth-twin O_2 signal. For a given radial velocity offset (see Section 5.4.1), we are able to simulate 13 transits using the UVES time-series in its original order, without the need to re-use or re-order spectra.

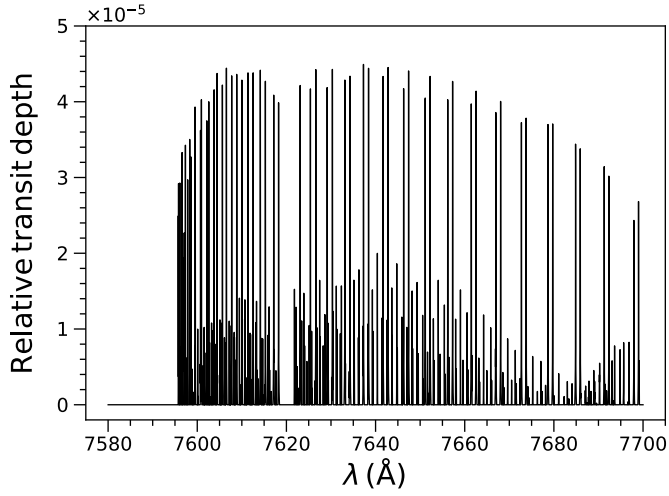

Figure 5.4. High-resolution ($\mathcal{R} = 100,000$) model transmission spectrum of the O_2 A band for an Earth-twin transiting an M5V star. A high-pass filter was used to remove the broadband component in the transmission spectrum for which the high-dispersion transit technique is insensitive.

5.3.2 Signal recovery

Subsequently, to retrieve the O_2 transmission signal, we normalize each spectrum to its median flux value on the range 7500–7570 Å, and flag regions where overlapping spectral orders are poorly stitched. We also flag the stellar potassium doublet at 7665/7699 Å, as well as the most-saturated telluric O_2 lines. Several steps are required to remove the telluric O_2 and (weak) water transmission spectrum. The measured fluxes at each wavelength step are first divided by their median value, essentially normalizing each wavelength column to its typical depth for that night. We subsequently fit each column with a quadratic function in airmass, and divide out the main temporal variations. Finally, we use SVD to identify and remove the strongest residual noise components present in the data set, as used by de Kok et al. (2013). The number of SVD components is chosen such that the S/N from combining the 13 unique transits at a given offset velocity is maximized (see Section 5.4.1). A high-pass filter is subsequently applied to remove low-frequency trends in the spectra.

The exoplanet O_2 signal is extracted by cross-correlating each filtered transit spectrum with the O_2 template spectrum over velocities ranging from -100 to $+100$ km s^{-1} in steps of 1 km s^{-1} in the exoplanet rest frame. This results in 39 cross-correlation functions (CCFs) per transit, of which the sum corresponds to its overall transmission signal. We perform the same analysis on the spectra without injected transmission signals to assess the retrieved S/N of O_2, by comparing the cross-correlation function of the spectra with and without injected signals, using

$$\mathrm{S/N} = \frac{\max(\mathrm{CCF_{inj}} - \mathrm{CCF_0})}{\mathrm{std}(\mathrm{CCF_0})}, \tag{5.2}$$

where $\mathrm{CCF_{inj}}$ and $\mathrm{CCF_0}$ are the summed cross-correlation functions for the injected and non-injected spectra, respectively, and $\mathrm{std}(\mathrm{CCF_0})$ is the standard deviation of the summed CCF of the non-injected spectra.

5.3.3 Perfect Gaussian-noise comparisons

We also repeat each transit simulation using synthetic data consisting of pure Gaussian noise to quantify the influence of systematic effects on the signal retrieval. For each UVES observation we create a corresponding synthetic "spectrum" by sampling a Gaussian normal distribution on a pixel-by-pixel basis, with a standard deviation such that it matches the S/N of the spectrum in the telluric-free region scaled by the square root of the relative flux.

A nearly similar procedure is followed for the synthetic data set as for the real spectra to retrieve the oxygen transmission signals. Continuum normalization, wavelength-column normalization, and airmass and SVD corrections are not necessary as there are, by definition, no systematic effects in the synthetic data. We do perform the same flagging procedures and filtering to preserve their effect on the CCF.

5.4 Results

5.4.1 Transits at constant v_{offset}

We inject 13 transits for velocity offsets v_{offset} ranging from -200 to $+200$ km s^{-1} in steps of 2 km s^{-1} in the UVES data of Proxima, using the methods outlined in Section 5.3. The v_{offset} factor combines both the systematic velocity of the target and the radial component of the Earth's barycentric orbital velocity, which we take as constant because the induced shift has a magnitude $\sim$0.01 pixels across each 8 hr set of observations. We also neglect the Earth's rotation, as this effect only induces a $\sim$0.1 pixel shift over 8 hr. We use real data, so the stellar lines do shift by these amounts during the observations, however our analysis removes their effect. By simulating transits at different v_{offset} we can mimic observations at different times of year.

The average per-transit S/N for each offset velocity at an instrument and telescope throughput of 20%, calculated from the 13 unique transits at that v_{offset}, is shown in solid purple in Figure 5.5. The S/N depends on the overlap with telluric lines, which depends on v_{offset}, and ranges from S/N = 0.4 to 1.0 for $|v_{\mathrm{offset}}| > 16$ km s^{-1}. At $|v_{\mathrm{offset}}| < 16$ km s^{-1}, the injected exoplanet O_2 lines fall within the flagging bounds for the heavily saturated telluric O_2 lines, leading to essentially no retrieved exoplanet signal. Because the strongest O_2 A-band lines lie in pairs, maximum S/N occurs around $v_{\mathrm{offset}} = \pm 22$ km s^{-1} when both exoplanet lines are free of tellurics. As discussed in Section 5.3.3, we also perform transit simulations using synthetic data consisting of purely Gaussian noise. For each v_{offset} we repeat the 13 transit simulations for 100 initializations of Gaussian-noise data. The median per-transit S/N for each v_{offset} at a throughput of 20% is shown in Figure 5.5 in solid blue, and mimics the trend seen for the UVES simulations, albeit up to 45% higher. The per-transit S/N values for both the UVES and Gaussian simulations are generally consistent with the per-transit S/N predicted by Snellen et al. (2013).

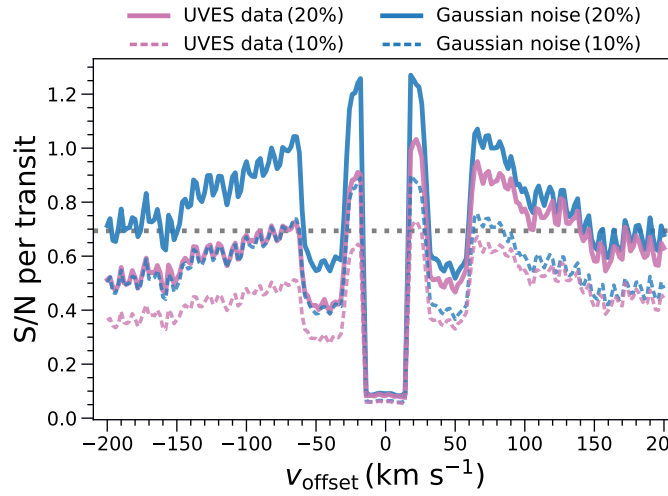

Figure 5.5. Average signal-to-noise per transit for molecular oxygen as a function of velocity offset, which incorporates both the systematic velocity of the target and the radial component of the Earth's barycentric velocity. The purple lines denote the UVES data results, while the blue lines indicate the median Gaussian-noise results for instrument and telescope throughputs of 20% (solid) and 10% (dashed). The dotted gray line shows the prediction of Snellen et al. (2013), who assumed a 20% throughput.

5.4.2 Combining transits at multiple $v_{\rm offset}$

To estimate the number of transits required to detect O_2, we vary $v_{\rm offset}$ to mimic the change in the radial component of Earth's orbital motion toward the star during an observing season. For each systematic velocity $v_{\rm sys}$, the N per-transit S/N values from Figure 5.5 that fall within $v_{\rm sys} \pm 20$ km s^{-1} are added in quadrature, and then normalized by $\sqrt{N}$. This results in the nominal S/N per transit expected during an observing season centered at $v_{\rm sys}$. This is subsequently scaled to estimate how many transits observations are required to reach a 3σ O_2 signal.

For $v_{\rm sys}$ ranging from -100 to $+100$ km s^{-1} in steps of 2 km s^{-1}, Figure 5.6 plots the number of transits required to reach this level, as well as the corre-

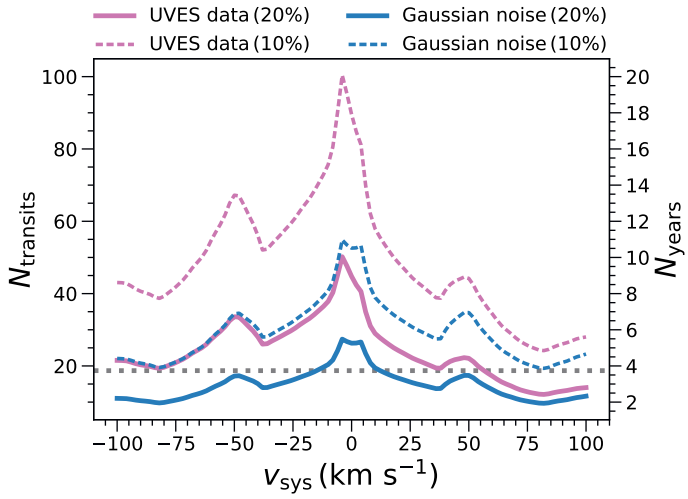

Figure 5.6. *Left axis*: estimate of the number of transits required to achieve a 3σ molecular oxygen detection as a function of the systematic velocity of the target, accounting for the change in barycentric velocity due to Earth's motion around the Sun. *Right axis*: corresponding number of years needed to collect the transit observations, assuming a typical observability. The estimates based on UVES data and Gaussian noise are shown in purple and blue, respectively, for 20% (solid) and 10% (dashed) instrument and telescope throughputs. The Snellen et al. (2013) prediction assumed a 20% throughput, and is denoted in dotted gray.

sponding number of years to collect such observations, assuming five[5] transits are observable each year. The UVES data indicate that the required number of transits to achieve an O_2 detection of S/N = 3 for an instrument and telescope throughput of 20% ranges from 20 to 50 for $v_{\rm sys}$ of 0 to ± 50 km s^{-1}, corresponding to 4–10 yr of observations. Note that the total amount of observing time needed will range between 70 and 175 hr over this period of time.

[5]Targets are typically above the horizon 50% of the time, and it is sufficiently dark at the observatory for only one-third of the time. Assuming an orbital period of 11.8 days, this results in five transits per year.

5.5 Discussion and conclusions

The number of transits required for an O_2 detection, as predicted by using real spectroscopic data of Proxima, is very similar to that predicted by Snellen et al. (2013) and Rodler & López-Morales (2014). This implies that real astronomical and instrumental effects that were not considered in the previous simulations do not strongly affect the power of the cross-correlation technique in retrieving molecular oxygen. In particular, the archival UVES spectra show considerable wavelength instabilities that have been effectively removed by the methods presented in Section 5.2.1. In addition, the strong S/N variations as a function of wavelength due to the dense forest of stellar molecular lines and saturated telluric oxygen lines were not prohibitive in recovering the exoplanet signal over a wide range of radial velocities. As expected, any microtellurics are effectively taken out by the SVD (Section 5.3.2). During the three nights of observation, the occurrence of variable line emission in the cores of the 7665/7699 Å stellar potassium doublet shows that Proxima experienced several flares. Our masking of the potassium doublet line cores (Section 5.3.2) was sufficient to mitigate their potential effect on the oxygen retrieval.

Although we injected the exoplanet O_2 signal at $\mathcal{R} = 10^5$, the UVES data have $\mathcal{R} \sim 40,000$. We do not expect that performing this study using $\mathcal{R} \sim 10^5$ tellurics will substantially improve our results in terms of the range of $v_{\rm offset}$ that can be probed. The strongest telluric O_2 lines that we flag are saturated, so increasing the resolving power will not dramatically narrow their line widths.

We conclude, using archival UVES data of Proxima, that a few dozen transits observed with the future ELTs are required to detect molecular oxygen from an Earth-twin transiting an $I = 11$ mag M5V star, assuming an instrument and telescope throughput of 20% and a resolving power of $\mathcal{R} = 100,000$. For a single ELT, the required number of transits can be collected on a timescale of 4–10 yr, which is very similar to that predicted by Snellen et al. (2013) and Rodler & López-Morales (2014).

For this method to live up to its potential, a high instrumental throughput is key because the required number of transits is linearly dependent on it. While the newest generation of high-dispersion spectrographs can achieve throughputs in the range 10–20%, we emphasize the importance of further development of instrument design to increase the throughput, e.g., through novel designs of high-dispersion spectrographs that specifically target the molecular oxygen band(s) (Ben-Ami et al. 2018).

Additionally, we note that strong instrumental effects present in the UVES data, particularly those affecting the wavelength solution, require us to imple-

ment SVD techniques to mitigate their influence on the transmission signal. These techniques are known to remove part of the exoplanet signal. Indeed, we determine signal losses ∼10–20% for $|v_{\rm offset}| > 16$ km s^{-1}. A stabilized spectrograph would not suffer from such instrumental effects, which may improve the S/N per transit.

Acknowledgments

The authors acknowledge support from the European Research Council under the European Union's Horizon 2020 research and innovation program under grant agreement No. 694513. The authors thank the anonymous referee for their insightful comments. The authors also thank R.J. de Kok for use of his O_2 transmission models, and F.J. Alonso-Floriano, O. Contigiani, H.J. Hoeijmakers, D.J.M. Petit dit de la Roche, and A.R. Ridden-Harper for helpful discussions.

Bibliography

Allard, F., Homeier, D., & Freytag, B. 2011, in Astronomical Society of the Pacific Conference Series, Vol. 448, 16th Cambridge Workshop on Cool Stars, Stellar Systems, and the Sun, ed. C. Johns-Krull, M. K. Browning, & A. A. West, 91

Allard, F., Homeier, D., & Freytag, B. 2012, Philosophical Transactions of the Royal Society of London Series A, 370, 2765

Allard, F., Homeier, D., Freytag, B., Schaffenberger, W., & Rajpurohit, A. S. 2013, Memorie della Societa Astronomica Italiana Supplementi, 24, 128

ALMA Partnership, Brogan, C. L., Pérez, L. M., et al. 2015, ApJ, 808, L3

Alonso-Floriano, F. J., Sánchez-López, A., Snellen, I. A. G., et al. 2019, A&A, 621, A74

Altwegg, K., Balsiger, H., Bar-Nun, A., et al. 2015, Science, 347, 1261952

Andrews, S. M. 2020, ARA&A, 58, 483

Andrews, S. M., Wilner, D. J., Zhu, Z., et al. 2016, ApJ, 820, L40

Arcangeli, J., Désert, J.-M., Line, M. R., et al. 2018, ApJ, 855, L30

Armitage, P. J., Livio, M., Lubow, S. H., & Pringle, J. E. 2002, MNRAS, 334, 248

Asplund, M., Grevesse, N., Sauval, A. J., & Scott, P. 2009, ARA&A, 47, 481

Ayres, T. R., Lyons, J. R., Ludwig, H. G., Caffau, E., & Wedemeyer-Böhm, S. 2013, ApJ, 765, 46

Bae, J., Zhu, Z., Baruteau, C., et al. 2019, ApJ, 884, L41

Barman, T. S., Konopacky, Q. M., Macintosh, B., & Marois, C. 2015, ApJ, 804, 61

Baxter, C., Désert, J.-M., Parmentier, V., et al. 2020, A&A, 639, A36

Bell, C. P. M., Mamajek, E. E., & Naylor, T. 2015, MNRAS, 454, 593

Ben-Ami, S., López-Morales, M., Garcia-Mejia, J., Gonzalez Abad, G., & Szentgyorgyi, A. 2018, ApJ, 861, 79

Bertrang, G. H. M., Avenhaus, H., Casassus, S., et al. 2018, MNRAS, 474, 5105

Bétrémieux, Y. & Kaltenegger, L. 2014, ApJ, 791, 7

Biller, B. A., Males, J., Rodigas, T., et al. 2014, ApJ, 792, L22

Birkby, J. L., de Kok, R. J., Brogi, M., et al. 2013, MNRAS, 436, L35

Blondel, P. F. C. & Djie, H. R. E. T. A. 2006, A&A, 456, 1045

Bonnet, H., Abuter, R., Baker, A., et al. 2004, The Messenger, 117, 17

Bourrier, V., Kitzmann, D., Kuntzer, T., et al. 2020, A&A, 637, A36

Brogi, M., de Kok, R. J., Albrecht, S., et al. 2016, ApJ, 817, 106

Brogi, M., Giacobbe, P., Guilluy, G., et al. 2018, A&A, 615, A16

Brogi, M. & Line, M. R. 2019, AJ, 157, 114

Caballero, J. A., Guàrdia, J., del Fresno, M. L., et al. 2016, in Observatory Operations: Strategies, Processes, and Systems VI, ed. A. B. Peck, R. L. Seaman, & C. R. Benn, Vol. 9910, International Society for Optics and Photonics (SPIE), 110–127

Cabot, S. H. C., Madhusudhan, N., Hawker, G. A., & Gandhi, S. 2019, MNRAS, 482, 4422

Casasayas-Barris, N., Pallé, E., Yan, F., et al. 2019, A&A, 628, A9

Charbonneau, D., Brown, T. M., Latham, D. W., & Mayor, M. 2000, ApJ, 529, L45

Charbonneau, D., Brown, T. M., Noyes, R. W., & Gilliland, R. L. 2002, ApJ, 568, 377

Chauvin, G., Desidera, S., Lagrange, A. M., et al. 2017, A&A, 605, L9

Chavez, J. & Lambert, D. L. 2009, ApJ, 699, 1906

Chazelas, B., Lovis, C., Blind, N., et al. 2020, in Adaptive Optics Systems VII, ed. L. Schreiber, D. Schmidt, & E. Vernet, Vol. 11448, International Society for Optics and Photonics (SPIE), 1393–1401

Chen, G., Pallé, E., Parviainen, H., Murgas, F., & Yan, F. 2021, ApJ, 913, L16

Clegg, R. E. S., Lambert, D. L., & Bell, R. A. 1979, ApJ, 234, 188

Collier Cameron, A., Guenther, E., Smalley, B., et al. 2010, MNRAS, 407, 507

Cont, D., Yan, F., Reiners, A., et al. 2021, A&A, 651, A33

Crawford, I. A. 2000, MNRAS, 317, 996

Cugno, G., Patapis, P., Stolker, T., et al. 2021, A&A, 653, A12

Daylan, T., Günther, M. N., Mikal-Evans, T., et al. 2019, arXiv e-prints, arXiv:1909.03000

de Kok, R. J., Brogi, M., Snellen, I. A. G., et al. 2013, A&A, 554, A82

Dekker, H., D'Odorico, S., Kaufer, A., Delabre, B., & Kotzlowski, H. 2000, in Society of Photo-Optical Instrumentation Engineers (SPIE) Conference Series, Vol. 4008, Optical and IR Telescope Instrumentation and Detectors, ed. M. Iye & A. F. Moorwood, 534–545

Donati, J. F., Gregory, S. G., Alencar, S. H. P., et al. 2012, MNRAS, 425, 2948

Dunkin, S. K., Barlow, M. J., & Ryan, S. G. 1997a, MNRAS, 286, 604

Dunkin, S. K., Barlow, M. J., & Ryan, S. G. 1997b, MNRAS, 290, 165

Ehrenreich, D., Lovis, C., Allart, R., et al. 2020, Nature, 580, 597

Eisenhauer, F., Abuter, R., Bickert, K., et al. 2003, in Society of Photo-Optical Instrumentation Engineers (SPIE) Conference Series, Vol. 4841, Instrument Design and Performance for Optical/Infrared Ground-based Telescopes, ed. M. Iye & A. F. M. Moorwood, 1548–1561

Eistrup, C., Walsh, C., & van Dishoeck, E. F. 2018, A&A, 613, A14

Espinoza, N., Rackham, B. V., Jordán, A., et al. 2019, MNRAS, 482, 2065

Evans, T. M., Sing, D. K., Goyal, J. M., et al. 2018, AJ, 156, 283

Evans, T. M., Sing, D. K., Kataria, T., et al. 2017, Nature, 548, 58

Fedele, D., Carney, M., Hogerheijde, M. R., et al. 2017, A&A, 600, A72

Foreman-Mackey, D., Hogg, D. W., Lang, D., & Goodman, J. 2013, PASP, 125, 306

Fortney, J. J., Lodders, K., Marley, M. S., & Freedman, R. S. 2008, ApJ, 678, 1419

Fressin, F., Torres, G., Charbonneau, D., et al. 2013, ApJ, 766, 81

Freudling, W., Romaniello, M., Bramich, D. M., et al. 2013, A&A, 559, A96

Gandhi, S., Brogi, M., Yurchenko, S. N., et al. 2020, MNRAS, 495, 224

Gandhi, S. & Madhusudhan, N. 2019, MNRAS, 485, 5817

Genda, H. & Ikoma, M. 2008, Icarus, 194, 42

Gibson, N. P., Merritt, S., Nugroho, S. K., et al. 2020, MNRAS, 493, 2215

Gontcharov, G. A. 2006, Astronomical and Astrophysical Transactions, 25, 145

Goodman, J. & Weare, J. 2010, Communications in Applied Mathematics and Computational Science, 5, 65

Gratton, R., Ligi, R., Sissa, E., et al. 2019, A&A, 623, A140

Gustafsson, B., Edvardsson, B., Eriksson, K., et al. 2008, A&A, 486, 951

Haffert, S. Y., Bohn, A. J., de Boer, J., et al. 2019, Nature Astronomy, 3, 749

Hartogh, P., Lis, D. C., Bockelée-Morvan, D., et al. 2011, Nature, 478, 218

Haynes, K., Mandell, A. M., Madhusudhan, N., Deming, D., & Knutson, H. 2015, ApJ, 806, 146

Herbig, G. H. 1977, ApJ, 214, 747

Herman, M. K., de Mooij, E. J. W., Jayawardhana, R., & Brogi, M. 2020, AJ, 160, 93

Hoeijmakers, H. J., Ehrenreich, D., Heng, K., et al. 2018a, Nature, 560, 453

Hoeijmakers, H. J., Ehrenreich, D., Kitzmann, D., et al. 2019, A&A, 627, A165

Hoeijmakers, H. J., Schwarz, H., Snellen, I. A. G., et al. 2018b, A&A, 617, A144

Hubeny, I., Burrows, A., & Sudarsky, D. 2003, ApJ, 594, 1011

Hughes, G. L., Gibson, B. K., Carigi, L., et al. 2008, MNRAS, 390, 1710

Jao, W.-C., Henry, T. J., Subasavage, J. P., et al. 2014, AJ, 147, 21

Jones, A., Noll, S., Kausch, W., Szyszka, C., & Kimeswenger, S. 2013, A&A, 560, A91

Kaltenegger, L. 2017, ARA&A, 55, 433

Keppler, M., Benisty, M., Müller, A., et al. 2018, A&A, 617, A44

Kesseli, A. Y., Snellen, I. A. G., Casasayas-Barris, N., Molliere, P., & Sanchez-Lopez, A. 2021, arXiv e-prints, arXiv:2111.09916

Konopacky, Q. M., Barman, T. S., Macintosh, B. A., & Marois, C. 2013, Science, 339, 1398

Kovács, G., Kovács, T., Hartman, J. D., et al. 2013, A&A, 553, A44

Lacour, S., Wang, J. J., Rodet, L., et al. 2021, A&A, 654, L2

Laertius, D. & Hicks, R. D. 2015, Lives of Eminent Philosophers (Cambridge, MA: Harvard University Press)

Lagrange, A. M., Bonnefoy, M., Chauvin, G., et al. 2010, Science, 329, 57

Lambert, D. L. & Luck, R. E. 1977, ApJ, 211, 443

Lambert, D. L. & Mallia, E. A. 1972, MNRAS, 156, 337

Lavigne, J.-F., Doyon, R., Lafrenière, D., Marois, C., & Barman, T. 2009, ApJ, 704, 1098

Leya, I., Schönbächler, M., Wiechert, U., Krähenbühl, U., & Halliday, A. N. 2008, Earth and Planetary Science Letters, 266, 233

Ligi, R., Vigan, A., Gratton, R., et al. 2018, MNRAS, 473, 1774

Lin, D. N. C., Bodenheimer, P., & Richardson, D. C. 1996, Nature, 380, 606

Lincowski, A. P., Lustig-Yaeger, J., & Meadows, V. S. 2019, AJ, 158, 26

Line, M. R., Brogi, M., Bean, J. L., et al. 2021, Nature, 598, 580

Linsky, J. L., Draine, B. T., Moos, H. W., et al. 2006, ApJ, 647, 1106

Lippincott, E. R., Eck, R. V., Dayhoff, M. O., & Sagan, C. 1967, ApJ, 147, 753

Lodders, K. 2002, ApJ, 577, 974

Lothringer, J. D. & Barman, T. 2019, ApJ, 876, 69

Lothringer, J. D., Barman, T., & Koskinen, T. 2018, ApJ, 866, 27

Louden, T. & Wheatley, P. J. 2015, ApJ, 814, L24

Lovelock, J. E. 1965, Nature, 207, 568

Lovelock, J. E. 1975, Proceedings of the Royal Society of London Series B, 189, 167

Luger, R. & Barnes, R. 2015, Astrobiology, 15, 119

Madhusudhan, N. 2019, ARA&A, 57, 617

Marconi, A., Abreu, M., Adibekyan, V., et al. 2020, in Ground-based and Airborne Instrumentation for Astronomy VIII, ed. C. J. Evans, J. J. Bryant, & K. Motohara, Vol. 11447, International Society for Optics and Photonics (SPIE), 461–472

Marois, C., Macintosh, B., Barman, T., et al. 2008, Science, 322, 1348

Mayor, M. & Queloz, D. 1995, Nature, 378, 355

McKemmish, L. K., Masseron, T., Hoeijmakers, H. J., et al. 2019, MNRAS, 488, 2836

Meadows, V. S. 2017, Astrobiology, 17, 1022

Meadows, V. S., Reinhard, C. T., Arney, G. N., et al. 2018, Astrobiology, 18, 630

Meija, J., Coplen, T. B., Berglund, M., et al. 2016, Pure and Applied Chemistry, 88, 293

Merritt, S. R., Gibson, N. P., Nugroho, S. K., et al. 2020, A&A, 636, A117

Mikal-Evans, T., Sing, D. K., Goyal, J. M., et al. 2019, MNRAS, 488, 2222

Milam, S. N., Savage, C., Brewster, M. A., Ziurys, L. M., & Wyckoff, S. 2005, ApJ, 634, 1126

Mollière, P. & Snellen, I. A. G. 2019, A&A, 622, A139

Mollière, P., van Boekel, R., Bouwman, J., et al. 2017, A&A, 600, A10

Mollière, P., van Boekel, R., Dullemond, C., Henning, T., & Mordasini, C. 2015, ApJ, 813, 47

Mollière, P., Wardenier, J. P., van Boekel, R., et al. 2019, A&A, 627, A67

Monnier, J. D., Harries, T. J., Aarnio, A., et al. 2017, ApJ, 838, 20

Morley, C. V., Skemer, A. J., Miles, B. E., et al. 2019, ApJ, 882, L29

Müller, A., Keppler, M., Henning, T., et al. 2018, A&A, 617, L2

Noll, S., Kausch, W., Barden, M., et al. 2012, A&A, 543, A92

Nugroho, S. K., Gibson, N. P., de Mooij, E. J. W., et al. 2020a, ApJ, 898, L31

Nugroho, S. K., Gibson, N. P., de Mooij, E. J. W., et al. 2020b, MNRAS, 496, 504

Nugroho, S. K., Kawahara, H., Gibson, N. P., et al. 2021, ApJ, 910, L9

Nugroho, S. K., Kawahara, H., Masuda, K., et al. 2017, AJ, 154, 221

Osorio, M., Anglada, G., Carrasco-González, C., et al. 2014, ApJ, 791, L36

Parmentier, V., Line, M. R., Bean, J. L., et al. 2018, A&A, 617, A110

Parmentier, V., Showman, A. P., & Lian, Y. 2013, A&A, 558, A91

Pavlenko, Y. V., Yurchenko, S. N., McKemmish, L. K., & Tennyson, J. 2020, A&A, 642, A77

Petit dit de la Roche, D. J. M., Hoeijmakers, H. J., & Snellen, I. A. G. 2018, A&A, 616, A146

Petrus, S., Bonnefoy, M., Chauvin, G., et al. 2021, A&A, 648, A59

Phillips, M. W., Tremblin, P., Baraffe, I., et al. 2020, A&A, 637, A38

Pino, L., Désert, J.-M., Brogi, M., et al. 2020, ApJ, 894, L27

Plez, B. 1998, A&A, 337, 495

Plez, B. 2012, Turbospectrum: Code for spectral synthesis

Pohl, A., Benisty, M., Pinilla, P., et al. 2017, ApJ, 850, 52

Quanz, S. P., Avenhaus, H., Buenzli, E., et al. 2013, ApJ, 766, L2

Quirrenbach, A., Amado, P. J., Caballero, J. A., et al. 2014, in Society of Photo-Optical Instrumentation Engineers (SPIE) Conference Series, Vol. 9147, Ground-based and Airborne Instrumentation for Astronomy V, ed. S. K. Ramsay, I. S. McLean, & H. Takami, 91471F

Rajpurohit, A. S., Allard, F., Rajpurohit, S., et al. 2018, A&A, 620, A180

Reggiani, M., Quanz, S. P., Meyer, M. R., et al. 2014, ApJ, 792, L23

Rodler, F. & López-Morales, M. 2014, ApJ, 781, 54

Romano, D., Matteucci, F., Zhang, Z. Y., Papadopoulos, P. P., & Ivison, R. J. 2017, MNRAS, 470, 401

Rucinski, S. 1999, in Astronomical Society of the Pacific Conference Series, Vol. 185, IAU Colloq. 170: Precise Stellar Radial Velocities, ed. J. B. Hearnshaw & C. D. Scarfe, 82

Sagan, C., Thompson, W. R., Carlson, R., Gurnett, D., & Hord, C. 1993, Nature, 365, 715

Sedaghati, E., Boffin, H. M. J., MacDonald, R. J., et al. 2017, Nature, 549, 238

Segura, A., Kasting, J. F., Meadows, V., et al. 2005, Astrobiology, 5, 706

Serindag, D. B., Nugroho, S. K., Mollière, P., et al. 2021, A&A, 645, A90

Sheppard, K. B., Mandell, A. M., Tamburo, P., et al. 2017, ApJ, 850, L32

Showman, A. P., Fortney, J. J., Lewis, N. K., & Shabram, M. 2013, ApJ, 762, 24

Showman, A. P., Fortney, J. J., Lian, Y., et al. 2009, ApJ, 699, 564

Showman, A. P. & Guillot, T. 2002, A&A, 385, 166

Smith, A. M. S., Anderson, D. R., Skillen, I., Collier Cameron, A., & Smalley, B. 2011, MNRAS, 416, 2096

Snellen, I. A. G. & Brown, A. G. A. 2018, Nature Astronomy, 2, 883

Snellen, I. A. G., de Kok, R. J., de Mooij, E. J. W., & Albrecht, S. 2010, Nature, 465, 1049

Snellen, I. A. G., de Kok, R. J., le Poole, R., Brogi, M., & Birkby, J. 2013, ApJ, 764, 182

Spiegel, D. S., Silverio, K., & Burrows, A. 2009, ApJ, 699, 1487

Stevenson, K. B., Désert, J.-M., Line, M. R., et al. 2014, Science, 346, 838

Tamuz, O., Mazeh, T., & Zucker, S. 2005, MNRAS, 356, 1466

Tennyson, J. & Yurchenko, S. N. 2012, MNRAS, 425, 21

Toci, C., Lodato, G., Christiaens, V., et al. 2020, MNRAS, 499, 2015

Trinquier, A., Elliott, T., Ulfbeck, D., et al. 2009, Science, 324, 374

Valenti, J. A., Piskunov, N., & Johns-Krull, C. M. 1998, ApJ, 498, 851

Wagner, K., Follete, K. B., Close, L. M., et al. 2018, ApJ, 863, L8

Walker, A. R. 1983, South African Astronomical Observatory Circular, 7, 106

Wood, B. E., Linsky, J. L., Hébrard, G., et al. 2004, ApJ, 609, 838

Wu, Y.-L., Sheehan, P. D., Males, J. R., et al. 2017, ApJ, 836, 223

Wyckoff, S. & Wehinger, P. 1972, ApJ, 178, 481

Yan, F., Pallé, E., Reiners, A., et al. 2020, A&A, 640, L5

Zechmeister, M., Reiners, A., Amado, P. J., et al. 2018, A&A, 609, A12

Zhang, J., Dauphas, N., Davis, A. M., Leya, I., & Fedkin, A. 2012, Nature Geoscience, 5, 251

Zhang, Y., Snellen, I. A. G., Bohn, A. J., et al. 2021a, Nature, 595, 370

Zhang, Y., Snellen, I. A. G., & Mollière, P. 2021b, A&A, 656, A76

Summary

Throughout history, humanity has been fascinated with the Universe. We have continuously sought to expand our understanding of its many wonders and, by extension, our place in it. Perhaps unsurprisingly, the existence of worlds beyond Earth has proven a recurring topic in philosophy and science fiction for millennia. Only about thirty years ago, however, did alien worlds fully enter the domain of science with the discovery in 1995 of a planet orbiting a star other than the Sun. In the decades since, much progress has been made to better understand these so-called exoplanets. As of the publication of this dissertation, approximately 5000 planets outside the Solar System are known to exist, and it is believed that there are at least as many planets in our Galaxy as stars. Such plenty brings with it the exciting opportunity to explore these strange new worlds and begin to answer questions such as *What kinds of planets exist beyond the Solar System? Of what are these planets made? How did they form?* and *Is there life beyond Earth?*

The methods used to detect exoplanets often provide very basic information about their characteristics, such as physical size and mass — the amount of composing material. With this information, it is possible to determine how dense a given exoplanet is, and thus infer whether it is made of mostly rock, ice, or gas. In this way, it is possible to develop a basic understanding of what kinds of exoplanets exist in our Galaxy. However, to understand planets beyond the Solar System in more detail, it is necessary to comprehensively study their atmospheres. Only then is it truly feasible to answer the aforementioned fundamental questions of exoplanetary science.

To study the atmospheres of exoplanets, it is common to perform spectroscopic observations — that is, to observe these objects using different colors (wavelengths) of light. In the resulting spectrum of a planet's atmosphere is encoded a wealth of information about its chemical composition. Different chemicals have unique spectral fingerprints in that they absorb and emit light of

different colors in a unique way. These unique patterns allow different chemicals to be distinguished from one another. Their presence or absence in the spectrum of an exoplanetary atmosphere thereby probes the chemical composition of these objects, despite them being trillions of kilometers away from Earth. Using high-dispersion instruments that more finely distinguish different wavelengths of light enables more robust analyses of atmospheres. Chapters 2–5 of this dissertation present four research projects studying exoplanet atmospheres at high dispersion.

Chapter 2 details a study to understand the chemical composition of some of the most extreme exoplanets. Hot Jupiters are gas-giant planets that orbit their stars at very close distances. A "year" on such planets lasts only a few days. For comparison, Mercury — the closest-orbiting planet in the Solar System — passes around the Sun in about 90 days. When these extreme exoplanets were discovered in the 1990s, research began to better understand the nature of their atmospheres, and in particular, the effect of receiving such an intense amount of starlight. It was predicted that these exoplanets orbit so closely to their stars, and thus their atmospheres are so hot, that the molecule titanium oxide (TiO), composed of a single atom each of titanium and oxygen, should exist as a gas at high altitudes on these worlds. However, studies that set out to test this theory have largely failed to provide unambiguous evidence for TiO gas in these hot, closely-orbiting gas-giant planets. The work presented in this chapter tried to reproduce a seminal detection of TiO in a particular planet called WASP-33b. At the time, it was the only unambiguous discovery of the molecule in such a planet. However, despite using the same observations and a better "fingerprint" for this chemical, we could not confirm its presence in WASP-33b. As discussed in Chapter 2, this conclusion serves as a cautionary tale regarding the techniques we use to study exoplanet atmospheres at high dispersion, and weakens the once seminal detection of TiO in this particular planet. In turn, the ambiguity surrounding the presence of TiO in these hot exoplanet atmospheres remains.

Chapter 3 investigates the feasibility of studying the different isotopes of titanium in large gaseous exoplanets. Isotopes are different varieties of a given chemical element, and behave slightly differently from one another. Measuring the comparative amount of each isotope of a chemical can provide information about an object. For instance, studying titanium isotopes in stars has provided information about the evolution of our Galaxy, whereas similar studies in the Solar System have been used to study its formation. In future, such analyses may provide similar insight into the formation of exoplanets. We first checked whether the analysis techniques commonly used to study exoplanet atmospheres

provide accurate measurements of titanium isotopes. We did this by applying these exoplanet-specific techniques to observations of a star, known to have TiO in its atmosphere composed of the different isotopes of titanium. By comparing our results to those from previous studies of similar stars, we conclude the methods used to study exoplanets should not significantly affect what we measure for the quantities of titanium isotopes. With this assurance, we determined how much observing time on current and future telescopes is required to perform such a study on a fainter exoplanet. Excitingly, studying titanium isotopes in large, widely-orbiting gas-giant planets is very feasible with current and upcoming observatories.

Chapter 4 presents an attempt to detect young, still-forming planets in an effort to better understand how this process works. Young stars are surrounded by so-called protoplanetary disks composed of gas and dust, in which it is believed planets form. Indeed, structures like rings, gaps between rings, and spirals are often seen in these protoplanetary disks, and are thought to be caused by young, possibly still-forming, planets. Studying the atmospheres of nascent planets is the most straightforward way to understand the planet-formation process, rather than trying to infer the history of an exoplanet after the fact. However, finding such young objects is rare. Recently, a study was published on the young star system HD 169142 suggesting a young planet may be present and causing the rings and spiral structures observed in that system's protoplanetary disk. We searched for, but could not find, evidence of this young planet's atmosphere in different observations of this system. We determined the data we used for this analysis is, in fact, not sensitive enough to detect the proposed planet, and thus more observations are required to confirm or deny its presence.

Chapter 5 concludes this dissertation with a forward-looking project evaluating the ability of large future telescopes to detect molecular oxygen (O_2) in Earth-like exoplanets. Just like on Earth, it is expected that O_2 may trace the presence of life on rocky exoplanets. There are, naturally, intricacies to this relatively simple relation, and many other criteria must be fulfilled before we can declare any future detection of oxygen to be evidence of extraterrestrial life. Nonetheless, the search for such biosignatures — chemicals that are associated with life on Earth — in the atmospheres of other worlds is seen as the most reasonable way forward in the search for life beyond the Solar System. Our work builds on previous studies which looked into the feasibility of using the upcoming larger and more powerful "extremely large telescopes" to search for O_2 in rocky exoplanets similar to Earth. Specifically, we performed our study in a manner that more realistically represents future searches for O_2 in Earth-like planets. We find that these more accurate simulations give very similar predic-

tions for how difficult it will be to detect O_2, and that even using these newer and more powerful telescopes, it will take several years to collect the necessary observations for a single exoplanet.

Samenvatting

Door de geschiedenis heen is de mensheid gefascineerd geweest door het heelal. We hebben voortdurend geprobeerd ons begrip van de vele wonderen van het heelal en hoe wij daar binnen passen uit te breiden. Het is misschien niet verwonderlijk dat het bestaan van werelden buiten de aarde al millennia lang een terugkerend onderwerp is in de filosofie en science fiction. Pas zo'n dertig jaar geleden echter kwamen buitenaardse werelden volledig in het domein van de wetenschap met de ontdekking in 1995 van een planeet die rond een andere ster dan de zon draaide. In de decennia daarna is er veel vooruitgang geboekt om deze zogenaamde exoplaneten beter te begrijpen. Bij de publicatie van dit proefschrift zijn er ongeveer 5000 planeten buiten het zonnestelsel bekend, en men denkt dat er minstens evenveel planeten als sterren in ons melkwegstelsel zijn. Zo'n overvloed brengt de opwindende mogelijkheid met zich mee om deze vreemde nieuwe werelden te verkennen en vragen te beantwoorden zoals *Welke soorten planeten bestaan er buiten het zonnestelsel? Waarvan zijn deze planeten gemaakt? Hoe zijn ze ontstaan?* en *Is er leven buiten de Aarde?*

De methoden die worden gebruikt om exoplaneten op te sporen, leveren vaak zeer elementaire informatie op over hun kenmerken, zoals de fysieke grootte en massa — de hoeveelheid materiaal waaruit ze bestaan. Met deze informatie is het mogelijk te bepalen wat voor dichtheid een bepaalde exoplaneet heeft, en is dus af te leiden of hij voornamelijk uit rots, ijs, of gas bestaat. Op deze manier is het mogelijk te weten te komen wat voor exoplaneten in ons Melkwegstelsel voorkomen. Maar om planeten buiten ons zonnestelsel beter te begrijpen, moeten hun atmosferen uitgebreid worden bestudeerd. Pas dan is het echt mogelijk om de eerder genoemde fundamentele vragen van de exoplaneetwetenschap te beantwoorden.

Om de atmosferen van exoplaneten te bestuderen, is het gebruikelijk spectroscopische waarnemingen te doen — dat wil zeggen, deze objecten waar te nemen met verschillende kleuren (golflengten) licht. In het resulterende spectrum

van de atmosfeer van een planeet is een schat aan informatie over zijn chemische samenstelling gecodeerd. Verschillende chemische stoffen hebben unieke spectrale vingerafdrukken waardoor zij licht van verschillende kleuren op een unieke manier absorberen en uitstralen. Dankzij deze unieke patronen kunnen verschillende chemische stoffen van elkaar worden onderscheiden. Hun aan- of afwezigheid in het spectrum van een exoplanetaire atmosfeer vertelt iets over de chemische samenstelling van deze objecten, ondanks dat ze triljoenen kilometers van de aarde verwijderd zijn. Het gebruik van instrumenten met een hoge dispersie die de verschillende golflengten van het licht beter van elkaar onderscheiden, maakt een robuustere analyse van atmosferen mogelijk. De hoofdstukken 2–5 van dit proefschrift stellen vier onderzoeksprojecten voor die exoplaneetatmosferen bestuderen bij hoge dispersie.

Hoofdstuk 2 beschrijft een studie om de chemische samenstelling van enkele van de meest extreme exoplaneten te begrijpen. Hete Jupiters zijn gasreuzenplaneten die op zeer korte afstand om hun ster draaien. Een "jaar" op zulke planeten duurt maar een paar dagen. Ter vergelijking: Mercurius — de planeet in het zonnestelsel die het dichtst bij de zon staat — draait in ongeveer 90 dagen rond de zon. Toen deze extreme exoplaneten in de jaren negentig werden ontdekt, begon men meer inzicht te krijgen in de aard van hun atmosferen, en in het bijzonder in het effect van het ontvangen van zo'n intense hoeveelheid sterlicht. Er werd voorspeld dat deze exoplaneten zo dicht bij hun sterren draaien, en dat hun atmosferen dus zo heet zijn, dat het molecuul titaniumoxide (TiO), dat bestaat uit één atoom titaan en één atoom zuurstof, als gas hoog in de atmosfeer van deze werelden zou moeten bestaan. Onderzoeken om deze theorie te testen zijn er echter grotendeels niet in geslaagd ondubbelzinnig bewijs te leveren voor het bestaan van TiO-gas op deze hete, dicht bij elkaar staande gasreuzenplaneten. Het werk dat in dit hoofdstuk wordt gepresenteerd, probeerde een baanbrekende detectie van TiO in een bepaalde planeet, WASP-33b genaamd, te reproduceren. Destijds was dit de enige ondubbelzinnige ontdekking van het molecuul op zo'n planeet. Maar ondanks het gebruik van dezelfde waarnemingen en een betere "vingerafdruk" voor deze chemische stof, konden we de aanwezigheid ervan op WASP-33b niet bevestigen. Zoals besproken in hoofdstuk 2, dient deze conclusie als een waarschuwing voor de technieken die we gebruiken om exoplaneetatmosferen bij hoge dispersie te bestuderen, en verzwakt ze de ooit baanbrekende detectie van TiO in deze specifieke planeet. De dubbelzinnigheid rond de aanwezigheid van TiO in deze hete exoplaneetatmosferen blijft bestaan.

Hoofdstuk 3 onderzocht of het mogelijk is om de verschillende isotopen van titaan op grote gasvormige exoplaneten te bestuderen. Isotopen zijn verschil-

lende varianten van een bepaald chemisch element, en gedragen zich enigszins verschillend van elkaar. Het meten van de relatieve hoeveelheid van elke isotoop van een chemische stof kan informatie verschaffen over een object. Zo heeft de studie van titaanisotopen in sterren informatie opgeleverd over de evolutie van ons Melkwegstelsel, terwijl soortgelijke studies in het zonnestelsel zijn gebruikt om de vorming ervan te bestuderen. In de toekomst kunnen dergelijke analyses een soortgelijk inzicht verschaffen in de vorming van exoplaneten. Wij zijn eerst nagegaan of de analysetechnieken die gewoonlijk worden gebruikt om exoplaneetatmosferen te bestuderen nauwkeurige metingen van titaanisotopen opleveren. We hebben dit gedaan door deze exoplaneetspecifieke technieken toe te passen op waarnemingen van een ster, waarvan bekend is dat deze TiO in zijn atmosfeer heeft, samengesteld uit de verschillende isotopen van titaan. Door onze resultaten te vergelijken met die van eerdere studies van soortgelijke sterren, concluderen we dat de methoden die gebruikt worden om exoplaneten te bestuderen geen significante invloed zouden moeten hebben op wat we meten voor de hoeveelheden titaanisotopen. Met deze zekerheid hebben we bepaald hoeveel waarneemtijd op huidige en toekomstige telescopen nodig is om zo'n studie op een zwakkere exoplaneet uit te voeren. Het is opwindend dat het bestuderen van titaanisotopen bij grote, wijd omcirkelende gasreuzenplaneten zeer goed mogelijk is met de huidige en toekomstige observatoria.

In hoofdstuk 4 wordt een poging gedaan om jonge, zich nog vormende planeten op te sporen, in een poging om beter te begrijpen hoe dit proces in zijn werk gaat. Jonge sterren worden omringd door zogenaamde protoplanetaire schijven, bestaande uit gas en stof, waarin zich vermoedelijk planeten vormen. Structuren zoals ringen, gaten tussen ringen en spiralen zijn vaak te zien in deze protoplanetaire schijven, en worden vermoedelijk veroorzaakt door jonge, mogelijk nog vormende, planeten. Het bestuderen van de atmosferen van ontluikende planeten is de meest eenvoudige manier om het proces van planeetvorming te begrijpen, in plaats van achteraf te proberen de geschiedenis van een exoplaneet af te leiden. Zulke jonge objecten worden echter zelden gevonden. Onlangs werd een studie gepubliceerd over het jonge sterrensysteem HD 169142, waarin werd gesuggereerd dat een jonge planeet aanwezig zou kunnen zijn en de ringen en spiraalstructuren zou kunnen veroorzaken die in de protoplanetaire schijf van dat systeem zijn waargenomen. Wij hebben in verschillende waarnemingen van dit systeem gezocht naar bewijzen voor de atmosfeer van deze jonge planeet, maar konden die niet vinden. We hebben vastgesteld dat de gegevens die we voor deze analyse hebben gebruikt in feite niet gevoelig genoeg zijn om de voorgestelde planeet te detecteren, en dat er dus meer waarnemingen nodig zijn om zijn aanwezigheid te bevestigen of te ontkennen.

Hoofdstuk 5 sluit dit proefschrift af met een toekomstgericht project waarin het vermogen van grote toekomstige telescopen om moleculaire zuurstof (O_2) bij aardachtige exoplaneten te detecteren wordt geëvalueerd. Net als op Aarde wordt verwacht dat O_2 de aanwezigheid van leven op rotsachtige exoplaneten kan aantonen. Er zitten natuurlijk haken en ogen aan deze relatief eenvoudige relatie en er moet aan nog veel meer criteria worden voldaan voordat we kunnen zeggen dat de aanwezigheid van zuurstof in de toekomst wijst op de aanwezigheid van buitenaards leven. Desalniettemin wordt het zoeken naar dergelijke biosignaturen — chemische stoffen die geassocieerd worden met leven op aarde — in de atmosferen van andere werelden gezien als de meest redelijke weg voorwaarts in de zoektocht naar leven buiten het zonnestelsel. Ons werk bouwt voort op eerdere studies die de haalbaarheid onderzochten van het gebruik van de aankomende grotere en krachtigere "extreem grote telescopen" om te zoeken naar O_2 in rotsachtige exoplaneten die vergelijkbaar zijn met de Aarde. Wij hebben ons onderzoek zo uitgevoerd dat het een realistischer beeld geeft van toekomstige zoektochten naar O_2 op aardachtige planeten. We stellen vast dat deze meer accurate simulaties zeer gelijkaardige voorspellingen geven voor hoe moeilijk het zal zijn om O_2 te detecteren, en dat het zelfs met deze nieuwere en krachtigere telescopen meerdere jaren zal duren om de nodige waarnemingen voor één enkele exoplaneet te verzamelen.

List of publications

A search for protoplanets around the young star HD 169142 using molecule mapping
Serindag, Griffiths, Snellen, and Landman
To be submitted (Chapter 4)

Measuring titanium isotope ratios in exoplanet atmospheres
Serindag, Snellen, and Mollière
2021, *Astronomy & Astrophysics*, 655, A69 (Chapter 3)

Is TiO emission present in the ultra-hot Jupiter WASP-33b? A reassessment using the improved ExoMol TOTO *line list*
Serindag, Nugroho, Mollière, de Mooij, Gibson, and Snellen
2021, *Astronomy & Astrophysics*, 645, A90 (Chapter 2)

A Search for FeH in Hot-Jupiter Atmospheres with High-Dispersion Spectroscopy
Kesseli, Snellen, Alonso-Floriano, Mollière, **Serindag**
2020, *The Astronomical Journal*, 160, 228

Testing the Detectability of Extraterrestrial O_2 with the Extremely Large Telescopes Using Real Data with Real Noise
Serindag and Snellen
2019, *The Astrophysical Journal Letters*, 871, L7 (Chapter 5)

Curriculum vitae

I was born on January 30, 1993, in Alexandria, Virginia, to Yuksel Serindag and Martha Banks-Serindag. Soon thereafter, we left the suburbs of Washington, D.C., for New England and moved to Middletown, Connecticut, to live with my grandfather, David Banks. For the next two decades, this university city was to be my home, and in hindsight, a consequential influence on my path through higher education. My curiosity was present from a very young age and was well encouraged by my parents and grandfather, who made the effort to expose me to a wide variety of topics — from the arts to the sciences, music to politics. Indeed, throughout my youth and well into my high-school years, my career goals fluctuated wildly and included jobs as diverse as veterinarian, jurist, writer, musician, and diplomat. Amidst these varied interests, one passion that sprouted and grew without interruption was a fascination with space and the Universe, so much so that one of the primary requirements in my university search was that the school have an astronomy department. In the end, I did not move very far for my undergraduate studies. After graduating from Middletown High School in 2011, I matriculated to Wesleyan University, whose Van Vleck Observatory is a mere ten-minute walk from my family's home. Having declared my undergraduate majors in both astronomy and physics, in the third year of my bachelor's, I began conducting astronomy research under the supervision of Seth Redfield and for the next two years, I worked on characterizing exoplanets based on their phase curves. During this period, a fortuitous internet search for research experiences abroad led to a three-month stint at Leiden University during the summer of 2014, working in the group of Ignas Snellen. It is not an exaggeration to say that the summer I spent at the Sterrewacht set up the next stages of my academic career. After obtaining my Bachelor of Arts from Wesleyan in 2015, I hopped continents and returned to Leiden University in the Netherlands to pursue a master's degree in astronomy. After a year working on protoplanetary disks with Michiel Hogerheijde, I rejoined Ignas Snellen's re-

search group for my second master's research project, evaluating the feasibility of detecting oxygen in terrestrial exoplanets. Ultimately, the transition to the PhD entailed a much shorter move. After obtaining my Master of Science in 2017, I remained at the Sterrewacht in Leiden to pursue a PhD researching exoplanet atmospheres under the supervision of Ignas Snellen. Over four-and-a-half years, I explored a diverse set of research topics in the field. First finishing my master's research on detecting extraterrestrial oxygen, I subsequently turned my attention to exploring the chemical and isotopic compositions of gas-giant exoplanets, and attempting to detect the atmospheres of candidate protoplanets still undergoing formation. The results of these endeavors constitute this dissertation, which likely marks the conclusion of my career as an astronomer and scientist. After spending more than ten years in the university environment — over eight of which involved research in astronomy — I have decided to leave academia. Where I will find myself in the coming years and decades remains undetermined, but the one certainty I do have for the future is that my general curiosity and specific fascination with the Universe, and all the strange and wonderful marvels it contains, will endure.

Acknowledgments

A PhD cannot be completed in isolation. It requires support from people outside the formal supervision structure. I hereby endeavor to express my gratitude as comprehensively as possible, while readily acknowledging that such an attempt will inevitably contain inadvertent oversights, for which I sincerely apologize.

Having a knowledgeable and friendly research group is not guaranteed, but in this regard I have been most fortunate. Thank you Alex Cridland, Alex Sánchez-López, Andrew Ridden-Harper, Aurélien, Aurora, Javi, Jens, Patrick, Paul, Rico, Sebastiaan, Tomas, and Yapeng for your research advice over the years. Many problems were quickly solved through your helpful interventions.

The support staff at the Sterrewacht and University also very much deserve my gratitude. In particular, thank you to the Sterrewacht IT department for being unfailingly patient with my technological struggles, and to the Sterrewacht Secretariat for your assistance in sorting out many logistical challenges.

Starting a new job is always a daunting prospect. Alberto, Andrej, Christos, Eleonora, Jit, Lorenzo, Maria Cristina, Tommaso, Valeria, and Vincenzo — you warmly welcomed me into your family from the beginning, making my transition to the PhD much smoother. From the bottom of my heart, grazie mille!

As any Sterrewachter knows, the borrel is the highlight of the work week, but is only as good as the company present. Alex Bohn, Alex Mechev, Alfred, Amy, Andrés, Andrew Allan, Arthur, Benoît, Christiaan, Christian, Ciaran, Dora, Drish, Elia, Elina, Erik, Evgenii, Folkert, Frits, Ivana, Jeroen, Joey, Josh Albert, Josh Butterworth, Lammim, Łukasz, Margot, Marina, Martijn, Matus, Merel, Michał, Michelle, Niccolò, Orestis, Osmar, Pranjal, Rob, Roi, Roland, Sierk, Steven, Thijs, Vanesa, and Zuzanna — you unfailingly livened Friday evenings, providing desperately needed and highly enjoyable recharges.

No life is complete without companions in adventure. Whether it was grabbing a coffee, attending a concert, enjoying nightlife, exploring a museum, participating in post-conference shenanigans, or simply hanging out, I could not

have asked for a better group than Andrea, Anna, Anniek, Bas, Dario, David, Dieuwertje, Dirk, Dominique, Lýdia, Mantas, Niloo, Patrick, Pooneh, Rafaël, Stella, Stijn, and Turgay.

Equally important are friends outside of work who keep you grounded and remind you that there is, in fact, a wonderful world beyond the Sterrewacht. Aaron, Bouke, Christine, Dara, Eimear, Gonzalo, Greg, Hannah, Isabel, Iva, Nicole, Radek, and Rob — in addition to all the fun we had, you helped me keep perspective and, more often than not, kept me afloat. For this, I cannot thank you enough. Additionally, thank you Eimear and Iva for your invaluable support in exiting academia.

Emanuele, you took me under your wing very early in my Leiden experience during LEAPS. Thank you for continuously challenging my preconceptions, and for always being generous in your advise for navigating the academic and non-academic landscape.

Marta, I am so glad that after two years of hoping, we *finally* managed to get to Amsterdam for Koningsnacht! Thank you for always being willing and eager to simply have fun. It may sound silly, but you reminded me how important it is to strive for a rich social life, and not allow a routine of complacent boredom develop and persist.

Kirsty, our mutual interests spanned quite a range in refinement, from performances at the opera and Concertgebouw to pumpkin bowling. Thank you for ensuring there was never a scarcity of gezelligheid, and for providing me much-needed reality checks.

Fraser, I can always count on you for a good gin and tonic, and getting my North American references. Thank you for being a calming influence and for always knowing what to say when my day required levity.

Jorge, I think we prove borrel friendships last forever! Thank you for always being down for bacchanal revelry, but more importantly, for teaching me how important it is to be myself.

Mikołaj, thank you for being a sounding board and fount of wisdom whenever I needed one. You are probably the most selfless person I know, and carried me through many difficult moments.

Gabriella, where to begin? You are my fellow wine aficionado, fashion police constable, and dispenser of justice. I can always depend on you for encouragement, advice, and general cheering up. Thank you for always having my back!

Omar — no words can quite do justice to the friendship we developed! From our long "philosophical discussions" (rants), to overindulging on food and drink on Gran Canaria, to simply being bad influences, we certainly created many

memories. Thank you for always pushing me to be better and to want more out of my life and career.

Lastly, but most importantly, I want to express how grateful I am to my family. Poppy, thank you for always reminding me how amazing the Universe is and the importance of unapplied research, especially when I was struggling with my own projects. Mom and Dad, you always supported me in my decision to leave the United States to continue in astronomy, even though that meant you would see me less often. And when I told you I would not continue in the field in which I spent a decade of my life studying and working, you never batted an eye. I honestly do not think I could ask for more loving, supportive parents. Kendar, thanks for always reminding me that life is too short and too precious not to take chances. Without all of you, I would never have made it to this point.